



University of
Stavanger

Faculty of Science and Technology

MASTER'S THESIS

Study program/Specialization:

Petroleum Geosciences Engineering

Spring, 2018

Open

Writer:

Khushal Adlakha

(Writer's signature)

Faculty supervisor: Nestor Fernando Cardozo Diaz

External supervisor(s): Lothar Schulte

Title of thesis:

Fracture analysis and modelling of the South Arne field

Credits (ECTS): 30

Keywords:

Fracture Intensity
Fracture Modelling
Seismic Attributes
South Arne Field
Permeability
Young Modulus

Pages: 116

Stavanger, 14th June, 2018

Copyright
by
Khushal Adlakha
2018

Fracture analysis and modelling of the South Arne field

by

Khushal Adlakha

Thesis

Presented to the Faculty of Science and Technology

The University of Stavanger

The University of Stavanger

June 2018

ACKNOWLEDGEMENTS

Firstly, I would like to thank my supervisors, Lothar Schulte and Nestor Cardozo, for their outstanding support, and encouragement throughout this project. I truly appreciate the time, knowledge, and guidance provided by them. I would also like to thank Surender Manral and Paul Henry Nadeau for his feedback during this project.

Further thanks to my colleagues, Mathias Tomasgaard, Lars Ulsund Frette, Luis Centeno, Thodoris Rozos and Signe Kristoffersen for their encouragement and suggestions throughout the project. I also thank Andreas Habel for his invaluable technical support.

I would also like to thank my mother, family and friends for their love, patience and motivation throughout this process.

ABSTRACT

Fracture analysis and modelling of the South Arne field

Khushal Adlakha

The University of Stavanger, 2018

Supervisor: Nestor Cardozo

External Supervisor: Lothar Schulte

Fractures are paramount elements in reservoirs, and they are omnipresent in almost all outcrops. The importance of fractures lies in their ability to provide permeable pathways and consequently increase the reservoir permeability. Therefore, fracture characterization and reliable fracture modelling are crucial in hydrocarbon exploration and production. The main objective of this study is to provide a detailed analysis of fractures measured at wells and their relationship to rock properties such as the Young Modulus. This study also focuses on using the seismic Young Modulus, resulting from seismic amplitude-variation-with-offset (AVO) inversion and structural seismic attributes like ant tracking and variance for guiding the modelling of fracture intensity. This approach represents an alternative workflow for improving fracture modelling by reducing the uncertainty in fracture intensity. The fracture models resulting from the different fracture intensity models are upscaled in a 3D grid in order to estimate their corresponding permeability distribution. These alternative permeability models are compared and discussed. The area of study is the South Arne field which is located in the Central Graben in the western part of the Danish North Sea. It consists of an elongated anticline in a fractured chalk reservoir. The results of the rock physics study indicate that the fractures of the South Arne field are associated with clay-poor chalk characterized by high Young Modulus values. The analysis of the well fracture data shows that the WNW-ESE fracture trend dominates the reservoir. General strike directions of the measured fractures are difficult to derive by conventional methods, such as stereo-net analysis because of the large data scattering. Therefore, a new methodology is discussed that allows a more reliable estimation of the fractures strike directions. The permeability models obtained from the fracture intensity guided by the seismically derived Young Modulus and seismic attributes, show zones of high and low permeability that are not observed in the permeability models obtained from interpolation techniques.

TABLE OF CONTENTS

Abstract.....	v
Table of Contents	vi
List of Tables	viii
List of Figures.....	ix
1. Introduction.....	1
1.1. Objectives of the Study	1
1.2. Impact of the Study	2
2. Geological Setting.....	3
2.1. Regional Geology	3
2.2. Tectonic Evolution.....	3
2.3. Arne-Elin Ridge	4
2.4. South Arne Field	5
3. Dataset.....	11
3.1. Seismic Data	11
3.2. Well Data	11
4. Theory and Background	15
4.1. Fractures.....	15
4.2. Fracture Properties	19
4.3. Rock Physics Properties, Elasticity and Fracture Relationship	23
4.4. Seismic Inversion.....	26
4.5. Discrete Fracture Network Modelling	31
4.6. Previous Work	36
5. Methodology	38
5.1. Introduction.....	38
5.2. Well Data Study	38
5.3. Seismic Study.....	43
5.4. Seismic AVO Inversion	48

5.5. Fracture Modelling.....	52
6. Results	58
6.1. Rock Physics Study.....	58
6.2. Faults and Fractures Study	63
6.3. Seismic Inversion and Seismic Attributes	75
6.4. Fracture Modelling Study	80
7. Discussion.....	86
8. Conclusion	90
9. References.....	91
10. Appendix.....	96
10.1. Fracture Data.....	96
10.2. Impact of fracture concentration and fracture aperture on fracture permeability	98
10.3. Fracture Modelling.....	101

LIST OF TABLES

Table 1. Available wells of the study area along with well type, and different well data present in the well (Green colour represents data is present, red colour represents data is absent). All the data is present for well SA-1A.....	14
Table 2 Aperture classification by size (Singhal and Gupta, 2010).	19
Table 3 Statistical laws used in fracture modelling	35
Table 4 Different values of concentration (marked in bold) used in the sensitivity analysis study.	55
Table 5 Different values of fracture aperture (marked in bold) used in the sensitivity analysis study.....	55
Table 6 Different values of fracture length (marked in bold) used in the sensitivity analysis study.	55
Table 7 Variogram ranges in major, minor and vertical direction for the fracture drivers.	56
Table 8 Relation between different reservoir properties from Figures 53 and 54.	61
Table 9 Relation between high fracture intensity and reservoir properties observed from Figures 55 and 56.	63
Table 10 Different lineament trends interpreted from the Ant-tracking algorithm. The labels in column 1 corresponds to the labels in Figure 58.....	66
Table 11 Different lineament trends interpreted from the variance attribute. The labels in Column 1 corresponds to the labels in Figure 61.	68
Table 12 Different lineament trends interpreted from the t^* attenuation attribute. The colours in Column 1 corresponds to the colours in Figure 63... ..	72
Table 13 Different fracture trends interpreted from the well azimuth histogram data. The fracture trends are illustrated in Figure 66.	75
Table 14 Change in mean permeability with change in fracture concentration. ...	81
Table 15 Change in mean permeability with change in fracture aperture.	81
Table 16 Relation of fracture intensity with the reservoir properties.	86
Table 17 Observed lineament trends interpreted from the well fracture data and the seismic data.	87

LIST OF FIGURES

Figure 1 A. Map of the Danish North Sea showing the location of the South Arne Field (marked in as red square). The line 1 in the figure corresponds to the geological cross-sections in Figure 2. Modified from (Møller and Rasmussen, 2003) B. Inset box shows the location of the Danish North Sea (coloured in red) and international borders.	2
Figure 2 The cross-section across the mid southern part of the Danish Central Graben (Møller and Rasmussen, 2003). See Figure 1 for location of the cross-section.	4
Figure 3 Lithostratigraphic summary for the Central Graben. Modified from Halland et al. (2011).	7
Figure 4 A. Bulk density (RHOB), compressional wave velocity (Vp), shear wave velocity (Vs), and porosity log of the Rigs-2 well. Note the high porosity in both the Ekofisk (upper reservoir) and Tor (lower reservoir) formations. Porosity is more homogenous in the Tor Formation than in the Ekofisk Formation. The Ekofisk Tight Zone (ETZ) is characterised in the logs by low porosity and high P- and S- wave velocity. B. Location of Rigs-2 well displayed on top Ekofisk surface. Modified from Vejrbæk et al. (2014).	8
Figure 5 A. A schematic cross-section through the field of study showing the Ekofisk and Tor reservoirs. Note the thickness variation over the crest and the flanks of the structure. B. Top Ekofisk surface with navigation of cross section C-C' shown in A. Modified from Garcia and MacBeth (2013).....	8
Figure 6 Outline of the main structural elements in the Chalk of the South Arne Field. Modified from Astratti et al. (2015).....	9
Figure 7. A. Seismic section showing the salt dome, gas chimney (marked in blue) and gas cloud (marked in red) in the overburden along with the interpreted top reservoir (Top Ekofisk). B. Top Ekofisk surface with navigation of cross section C-C' shown in A.	12
Figure 8 Trajectories of the horizontal wells and vertical wells along with the reservoir boundary. Most of the wells are horizontal. Well names are displayed for few wells only (Table 1).....	13
Figure 9 Stereo-net plot with well data from well SA-1A displaying the dip azimuth (points) and strike attribute (shaded area) of the fracture data. For the location of the well SA-1A, refer to Figure 8.	14
Figure 10 The orientation of various fracture types with respect to the principal stresses. Tension fractures (green) form parallel to σ_1 and σ_2 . The acute angle between two shear fractures (red) is called the conjugate angle. The angle between the shear fracture and σ_1 is called the dihedral angle. Modified from Bratton et al. (2006).....	16
Figure 11 Illustration of different types of fractures with respect to the relation between rock matrix porosity and permeability with the fracture porosity and fracture permeability. Modified from Nelson (2001).....	17
Figure 12 Rose diagram of shear fractures associated with a normal fault. Modified from Nelson (2001)	18
Figure 13 Conceptual model of basement reservoir within the structural closure. The reservoir is divided into three zones: (1) an Inner Fault Zone; (2) an Outer Fault Zone (both of which combine to make up a Fault Zone); and (3) a pseudo matrix (Trice, 2014).	18
Figure 14 Graph illustrating the relationship between fracture spacing and bed thickness for varying lithologies. Modified from Twiss and Moores (1992).....	20
Figure 15 I. An outcrop of rock where fracture porosity and matrix porosity are calculated. II. A small element of an outcrop of area 1 cm ² located between fractures. III. A small element of an outcrop of area 1 cm ² located over a fracture. The blue line represents a fracture. Note the change in fracture porosity between the two equal areas. Modified from Nelson (2001).....	21
Figure 16 A. Fracture model illustrating infilling materials, alteration and fracture porosity. B. Figure illustrating how flow rate Q is dependent on fracture aperture e. Modified from Paillet and Kapucu (1989).	22

Figure 17 Well-log data over a depth interval corresponding to a limestone reservoir. The first, second, third and fourth columns correspond to Gamma-Ray, P-wave velocity, S-wave velocity and the number of fractures per foot interpreted from FMI data respectively. Modified from Mavko (2000).	23
Figure 18 Change in length of the material as a result of applied stress.....	24
Figure 19 Average fracture number for several common rock types naturally deformed in the same physical environment. Modified from Stearns and Friedman (1972).	25
Figure 20 A. Compressive strength as a function of porosity. Modified from Dunn et al. (1973). B. Outcrop measurements of fracture intensity and corresponding porosity in a dolomite. Note the decreasing fracture intensity with increasing porosity. Modified from Nelson (2001). C. Relationship between compressive strength and Young Modulus. Modified from (Xu et al., 2016).	25
Figure 21 Model data illustrating inversion process.....	26
Figure 22 Frequency versus Amplitude plot illustrating the band-limited nature of seismic. Note how the low frequencies fill the band below the seismic and provides a geologic setting. It is possible to gain a few Hz on the high side as illustrated. Modified from Pendrel and Van Riel (2000).	27
Figure 23 A. The low-frequency model of acoustic impedance used to create the deterministic inversion. The three black lines represent three wells used for building the low-frequency model. Note the variation at the bottom of the well I. B. The results of the deterministic inversion (acoustic impedance) obtained using the low-frequency model. Modified from Francis (2014).	27
Figure 24 Generalized flow chart for model-based inversion. Light blue text boxes represent the input drivers. Modified from Simm and Bacon (2014).	28
Figure 25 A. Original seismic used for inversion. B. Synthetic seismic obtained from inversion. C. Difference between original and synthetic seismic.	28
Figure 26 A. Graphical representation of an acoustic wave striking a boundary between two media with different acoustic impedances. B. P-wave reflectivity as defined by different approximations to a hydrocarbon benchmark of shale overlying gas sand. Modified from Booth et al. (2015).	29
Figure 27 Schematic workflow of model-based pre-stack simultaneous inversion. Light blue text boxes represent the input data for the inversion. Modified from Simm and Bacon (2014).	31
Figure 28 A. Sketch illustrating the fracture intensity represented in 1D (P_{10}). B. Sketch illustrating the fracture intensity represented in 3D (P_{32}). Circles represent fracture surfaces. Modified from Dershowitz and Herda (1992).	34
Figure 30 A and B. Distribution of fracture orientation on stereo-net based on Fisher Model with different concentration parameters. C and D. Distribution of fracture orientation on stereo-net based on Kent Model with different concentration and anisotropy parameters. E and F. Distribution of fracture orientation on stereo-net based on Bingham Model with different azimuthal and radial concentration parameters. Note that mean dip and mean dip azimuth are the same, 90° and 70° respectively, in all the cases.....	37
Figure 31 Generalized workflow used in this thesis involving the well data, seismic data and fracture modelling. Numbers in the textboxes represent the sub-chapter where the particular study is discussed.	38
Figure 32 Workflow for well data study Numbers in the textboxes represent the sub-chapter where the particular study is discussed.	38
Figure 33 Histogram of dip azimuth (dip direction) of well SA-1A. The x-axis represents the dip azimuth (dip direction), and the y-axis represents the number of times a particular value is encountered in the dataset of well SA-1A, i.e., count or frequency. The coloured rectangle represents the fracture trends identified in the data. Red dashed line represents the borehole direction of the well.	40
Figure 34 Stereo-net plot of well SA-1A displaying the fracture azimuths. Coloured area represents the interpreted fracture trends derived from the histogram methodology, whereas, coloured arrows represent the corresponding mean strike direction.....	40

Figure 35 A. Cumulative fracture log of a well, used for calculating the fracture intensity log over a gliding window of user-defined length. B. Fracture intensity calculated using a window length of 10m. C. Fracture intensity calculated using a window length of 30m.	41
Figure 36 A. Sketch illustrating fractures perpendicular to the borehole. B. Sketch illustrating fractures parallel to the borehole. Note the difference in the number of fractures encountered in the borehole in both the cases. Case A results in higher fracture intensity.	42
Figure 37 Workflow for rock physics study illustrating the input, and the calculated logs. The grey dashed line around the boxes illustrates the cross-plots between the input and the calculated logs.	43
Figure 38 Workflow of seismic data illustrating the process and the results obtained.	43
Figure 39 Workflow for generating fault cube using Ant-tracking process. Ant-tracking faults obtained from (i) and (ii) are illustrated in Figure 41 and from (iii) and (iv) in Figure 42.	45
Figure 40 Stereo-net tab used in the Ant-tracking workflow. The white coloured area represents the open area for agents and grey coloured area represents the restricted area for agents. Note that the azimuth is measured with reference to the inline direction and not the true North. Modified from Schlumberger (2010).	46
Figure 41 A. and B. Ant-tracking faults obtained from the different aperture directions displayed on the top reservoir surface. C. Stereo-net tab illustrating the accepted search direction for agents to obtain the fault cube (A). D. Stereo-net tab illustrating the accepted search direction for agents to obtain the fault cube (B).	47
Figure 42 A. and B. Ant-tracking faults obtained from the different aperture directions displayed on the top reservoir surface. C. Stereo-net tab illustrating the accepted search direction for agents to obtain the fault cube (A). D. Stereo-net tab illustrating the accepted search direction for agents to obtain the fault cube (B).	47
Figure 43 AVO Inversion workflow illustrating the input data, process and the results obtained. The numbers in the text boxes represent the sub-chapter where the particular study is discussed.	48
Figure 44 A.i Deterministic wavelet extracted from near stack seismic. A.ii Power spectrum of deterministic wavelet extracted from near stack seismic. B.i Deterministic wavelet extracted from mid stack seismic. B.ii Power spectrum of deterministic wavelet extracted from mid stack seismic. C.i Deterministic wavelet extracted from far stack seismic. C.ii Power spectrum of deterministic wavelet extracted from mid stack seismic.	49
Figure 45 Frequency spectrum of the seismic data used for low-frequency model.	50
Figure 46 A. Low-frequency model of P-impedance. The black dotted line shows the interpreted top and bottom surface. B. Low-frequency model of S-impedance. C. Top Ekofisk surface with navigation of cross section D-D' shown in A and B.	51
Figure 47 Cross-plot of acoustic impedance log versus density log for the wells of the reservoir. The black line shows the best-fit polynomial function used for computing the density cube from the P-impedance cube.	51
Figure 48 Time to depth conversion and the 3G Grid construction workflow illustrating the conversion of horizons and seismic cubes into the depth domain and the construction of a 3D grid using horizons as surfaces.	52
Figure 49 Fracture modelling workflow based on the fracture intensity and intensity drivers as the input data.	53
Figure 50 A. Fracture length histogram modelled by a power law. B. The relation between fracture aperture and fracture permeability defined by cubic law. Note that the Permeability-Fracture aperture cross-plot is displayed in semi-logarithmic scale.	57

Figure 51 Gamma-Ray (GR), neutron (NPHI), bulk density (RHOB), compressional wave velocity (Vp), shear wave velocity (Vs), porosity, water saturation (Sw) and Young Modulus log of the Rigs-2 well. For the location of the well, refer to Figure 52. Note the high porosity in both the Ekofisk (upper reservoir) and Tor (lower reservoir) formations. Porosity is more homogenous in the Tor Formation than in the Ekofisk Formation.	59
Figure 52 Map showing the location of all wells. This figure is a reference map for Figures 51 to 56.	60
Figure 53 A. Density versus neutron porosity cross-plot colour-coded by Gamma-Ray. B. Density versus neutron porosity cross-plot colour-coded by different wells. For the location of the wells, refer to Figure 52.	60
Figure 54 A. Porosity versus Young Modulus cross-plot for Ekofisk Formation color-coded by Gamma-Ray. B. Porosity versus Young Modulus cross-plot for Tor Formation color-coded by Gamma-Ray. C. P-wave velocity versus Young Modulus cross-plot for Ekofisk Formation color-coded by Gamma-Ray. D. P-wave velocity versus Young Modulus cross-plot for Tor Formation color-coded by Gamma-Ray. The data in each plot corresponds to the well Rigs-1, Rigs-2, Rigs-3c and SA-1A. For the location of the wells, refer to Figure 52.	61
Figure 55 A. S-wave versus P-wave velocity cross-plot colour-coded by fracture intensity for Ekofisk Formation for well SA-1A. B. A. S-wave versus P-wave velocity cross-plot colour-coded by fracture intensity for Tor Formation for well SA-1A. The blue circle represents high fracture intensity points. For the location of the well SA-1A, refer to Figure 52.	62
Figure 56 A. Porosity versus Young Modulus cross-plot colour-coded by fracture intensity for Ekofisk Formation for well SA-1A. B. Porosity versus Young Modulus cross-plot colour-coded by fracture intensity for Tor Formation for well SA-1A. The blue circle represents high fracture intensity points. For the location of the well SA-1A, refer to Figure 52.	63
Figure 57 Cross-section A. I. A random line crossing the anticline structure south of the gas cloud. II. Top Ekofisk surface with navigation of cross section C-C'. Cross-section B. I. A random line crossing the anticline structure north of the gas cloud. II. Top Ekofisk surface with navigation of cross section D-D'	64
Figure 58 Interpreted top Ekofisk surface along with the trajectories of the drilled wells and the interpreted faults from the aggregated Ant-tracking cube. The wells are colour-coded, and marked circles represent the base location of the wells. The grey circle depicts the area of low-quality seismic data due to the gas cloud. A. NNW-SSE lineament trend observed inside the reservoir boundary. B. WNW-ESE lineament trend observed inside the reservoir boundary. C. NNE-SSW lineament trend present inside the reservoir boundary. D. ENE-WSW lineament trend present inside the reservoir boundary. E. Overburden polygonal faults trending ENE-WSW present outside the reservoir boundary. F. N-S lineament trend present inside the reservoir boundary.	65
Figure 59 A. A random line crossing the anticline structure south of the gas cloud along with the faults obtained from ant tracking. B. Top Ekofisk surface with navigation of cross section (C-C') shown in A. Note that the location of the random line is the same as that in Figure 57 Cross-section A.	66
Figure 60 A. Top Ekofisk surface illustrating the ENE-WSW lineament trend obtained from the Ant-tracking algorithm using the stereo-net functionality. The black and blue colour signifies the presence of lineaments. B. Stereo-net used for generating the fault cube for ENE-WSW lineament trend. i. Lineaments extracted 150 ms above the top Ekofisk surface. ii. Lineaments extracted on the top Ekofisk surface. iii. Lineaments extracted 150 ms below the top Ekofisk surface. Note the decrease in ENE-WSW lineaments from i to iii.	67

Figure 61 Variance attribute displayed for the time-slice (-2730 ms) within the reservoir. High variance values indicate discontinuities (i.e., faults). The grey circle highlights the area affected by the gas cloud. The yellow dashed line illustrates the reservoir boundary. A: Variance high-lighting NNW-SSE lineaments. B: WNW-ESE lineaments. C: NNE-SSW lineaments. D: polygonal faults. D': radial faults. 69

Figure 62 t^* attenuation attribute on the time-slice (-2818 ms) inside the reservoir along with the trajectories of the drilled wells. Region A marks the area of high t^* attenuation values while region B marks the area of low t^* attenuation values. 70

Figure 63 t^* attenuation attribute on the time-slice (-2766) inside the reservoir. Red dashed line indicates the reservoir boundary. The red, black, and green lines represent the NNW-SSE, WNW-ESE, and the N-S lineament trends respectively. 71

Figure 64 Dip azimuth histogram of fractures for wells SA-2, SA-6B, and SA-6C. Y-axis represents the number of times a particular frequency value is encountered in the dataset. Red dashed lines indicate the borehole direction of the three wells. For the location of the wells, refer to Figure 58. 72

Figure 65 Stereo-net showing the dip azimuth of fracture data for the well SA-2. The coloured area represents the interpreted fracture trends derived from the histogram methodology. Coloured arrows represent the strike directions of the interpreted fracture trends. Grey points outside the coloured area in the stereo-net are noise. For the location of the well SA-2, refer to Figure 58. 73

Figure 66 Top Ekofisk surface showing the faults obtained from the ant-tracking algorithm and trajectories of the wells. The wells are marked in different colours at their bottom depth. The arrows on the wells represent the different fracture trends of the corresponding well interpreted from the dip azimuth data. A. Brown arrows represent WNW-ESE fracture trend. B. Blue arrows represent NNW-SSE fracture trend. C. Green arrows represent N-S fracture trend. D. Orange arrows represent NNE-SSE fracture trend. 74

Figure 67 Upscaled P-impedance and Young Modulus, both based on AVO inversion displayed together with the corresponding well log data for well SA-1A. Green lines represent the contacts between the different formations. Note the mismatch in the Young Modulus between the seismic data and the well log data for the Ekofisk Tight Zone. For the location of the well SA-1A, refer to Figure 58. 76

Figure 68 A. Ant-tracking and Young Modulus results illustrated on a time-slice (-2788 ms) inside the reservoir. The red box shows the region displayed in B. B. Magnified image of the Ant-tracking and Young Modulus results illustrating the trend of both datasets in the north of the gas cloud. Red arrows indicate some of the regions where the Young Modulus follows the fault/lineament pattern. The grey area displays the gas cloud. Note that the low Young Modulus values are masked in both figures. Young Modulus values are higher where faults are present. 77

Figure 69 A. Variance and Young Modulus results illustrated on a time-slice (-2788 ms) inside the reservoir. The yellow box shows the region displayed in B. B. Magnified image of the variance and Young Modulus results illustrating the trend of both results to the north of the gas cloud. Black arrows indicate few of the regions where the Young Modulus follows the variance. Note that the low Young Modulus values are masked in both figures. 78

Figure 70 A. t^* attenuation and Young Modulus results illustrated on a time slice (-2788 ms) inside the reservoir. The yellow box shows the region displayed in B. B. Magnified image of the t^* attenuation and Young Modulus results illustrating the trend of both the results on the north of the gas cloud. Note that the low Young Modulus values are masked in both the figures. 79

Figure 71 A. Variance versus Young Modulus cross-plot of Rigs-2 well. B. t^* Attenuation versus Young Modulus cross-plot of Rigs-2 well. For the location of the well Rigs-2, refer to Figure 52. 80

Figure 72 Permeability distribution in i direction for different concentrations, keeping other fracture parameters constant. A, B, C, D and E give the permeabilities for fracture concentration values of 0.5, 1, 2, 4, and 8, respectively. The black arrow highlights the trend of the data.	81
Figure 73 Permeability distribution in i direction for different fracture aperture, keeping other fracture parameters constant. A, B, C, D and E give the permeabilities for the aperture value of 0.000075 mm, 0.00015 mm, 0.0003 mm, 0.0006 mm, and 0.0012 mm, respectively. The black arrow highlights the trend of the data.....	82
Figure 74 A. Modelled variogram for horizontal direction of the variance attribute (used as the secondary variable). B. Modelled variogram for the vertical direction of the variance attribute.....	83
Figure 75 Dip angle distribution of the fractures present in the three formations. Note the low dip angle of fractures present in Ekofisk Tight Zone.	83
Figure 76 Permeability in i direction in the horizontal slice in Tor Formation obtained using the fracture intensity guided by (A) standard statistical procedure, (B) variance attribute, and (C) Young Modulus.....	85
Figure 77 A. Dip azimuth histogram of fracture data for the well SA-3A illustrating interpreted fracture trends. B. Dip azimuth histogram of fracture data for the well SA-1B illustrating interpreted fracture trends. For the location of the wells, refer to Figure 58.....	96
Figure 78 A. Dip azimuth histogram of fracture data for the well SA-4A illustrating interpreted fracture trends. B. Dip azimuth histogram of fracture data for the well SA-6C illustrating interpreted fracture trends. For the location of the wells, refer to Figure 58.....	96
Figure 79 A. Dip azimuth histogram of fracture data for the well SA-5B illustrating interpreted fracture trends. B. Dip azimuth histogram of fracture data for the well SA-7 illustrating interpreted fracture trends. For the location of the wells, refer to Figure 58.....	97
Figure 80 Dip azimuth histogram of fracture data for the well SA-6B illustrating interpreted fracture trends. Brown rectangle indicates the WNW-ESE fracture trend, while orange colour indicates the NNE-SSW fracture trend. Red dash line indicates the borehole azimuth. For the location of the well SA-6B, refer to Figure 58.....	97
Figure 81 Dip azimuth histogram of fracture data for the well SA-2 illustrating interpreted fracture trends. Brown rectangle indicates the WNW-ESE fracture trend, while orange colour indicates the NNE-SSW fracture trend. Red dash line indicates the borehole azimuth. For the location of the well SA-2, refer to Figure 58.	98
Figure 82 Change in permeability in j direction with the change in concentration, keeping other parameters constant. A, B, C, D and E define the concentration value at 0.5, 1, 2, 4, and 8, respectively.	98
Figure 83 Change in permeability in j direction with the change in aperture, keeping other parameters constant. A, B, C, D and E define the aperture value at 0.000075 mm, 0.00015 mm, 0.0003 mm, 0.0006 mm, and 0.0012 mm, respectively.....	99
Figure 84 Change in permeability in k direction with the change in concentration, keeping other parameters constant. A, B, C, D and E define the concentration value at 0.5, 1, 2, 4, and 8, respectively.	99
Figure 85 Change in permeability in k direction with the change in aperture, keeping other parameters constant. A, B, C, D and E define the aperture value at 0.000075 mm, 0.00015 mm, 0.0003 mm, 0.0006 mm, and 0.0012 mm, respectively.....	100
Figure 86 Permeability in j direction in the horizontal slice in Tor Formation obtained using the fracture intensity guided by (A) standard statistical procedure, (B) variance attribute, and (C) Young Modulus.	101
Figure 87 Permeability in k direction in the horizontal slice in Tor Formation obtained using the fracture intensity guided by (A) standard statistical procedure, (B) variance attribute, and (C) Young Modulus.	102

1. INTRODUCTION

Fractures are paramount elements in reservoirs, and they are omnipresent in almost all outcrops. Many reservoirs are fractured to the degree that they can be treated as fractured reservoirs. The value of fractures lies in their ability to provide permeable pathways and consequently increase the reservoir permeability, potentially enhancing the flow rate of tight reservoirs. Therefore, fracture characterisation and modelling are of great practical importance in hydrocarbon exploration and production. They are critical factors for determining reservoir parameters, as well as for well-drilling planning (Cui et al., 2015).

Well logs provide essential information regarding fractures with high validity in the close vicinity of the wells. However, fracture characterisation and fracture modelling away from the wellbores is still challenging. Hence, fracture characterisation and fracture modelling require additional efforts to extrapolate fracture properties away from the wells. While additional information for fracture properties (i.e., length, aperture, and orientation) are often obtained from outcrops and analogues, the most significant uncertainty is related to the fracture intensity. Elastic inversion of 3D seismic data to estimate rock physics properties (e.g., Young Modulus) and seismic attributes provide valuable information, which can act as an additional guide for characterising fracture intensity. Consequently, elastic inversion and seismic attributes combined with Discrete Fracture Network (DFN) modelling can enhance the reliability of fracture models (Emsley et al., 2014).

The area of study is the South Arne field which is located within the Central Graben in the western part of the Danish North Sea. The South Arne field is one of the northernmost chalk fields in the Danish North Sea, extending 12.5 by 4 km and consisting of an elongated anticline in a naturally fractured chalk reservoir (Figure 1). The study done by Astratti et al. (2015) suggests that the two fracture sets developed in the South Arne reservoir are along the same WNW-ESE structural trend and are not separable on the seismic data. However, well data and, image log analysis show a wider azimuth distribution of fractures (Mackertich and Goulding, 1999).

1.1. Objectives of the Study

The motivation of this thesis is to provide a detailed analysis of fractures and their relationship to the Young Modulus calculated by P- and S- impedance and density. These three parameters result from the amplitude versus offset (AVO) inversion of seismic data from the study area. This thesis focuses on the application of using seismically derived Young Modulus and seismic attributes cubes as a guide for modelling fracture intensity. Hence, different fracture models can be built and

compared to fracture models produced by simple interpolation. Finally, fracture models are calculated and up-scaled to generate the permeability models suitable for reservoir simulation. An additional objective is to perform a sensitivity analysis of the fracture parameters (i.e., fracture aperture, fracture concentration) and their influence on the modelling results.

1.2. Impact of the Study

This thesis can help to better solve problems associated with modelling of fractured reservoirs. It can aid enhance the interpretation and modelling of fractures leading to a better understanding of fractured reservoirs. The comparison of non-seismic-based and seismic-based fracture models allows highlighting the differences in flow connectivity between these models. It also highlights the disadvantages of standard fracture modelling procedures with respect to seismic-based fracture models. In addition, sensitivity analysis aids in the understanding of the influence of the fracture parameters on the permeability model.

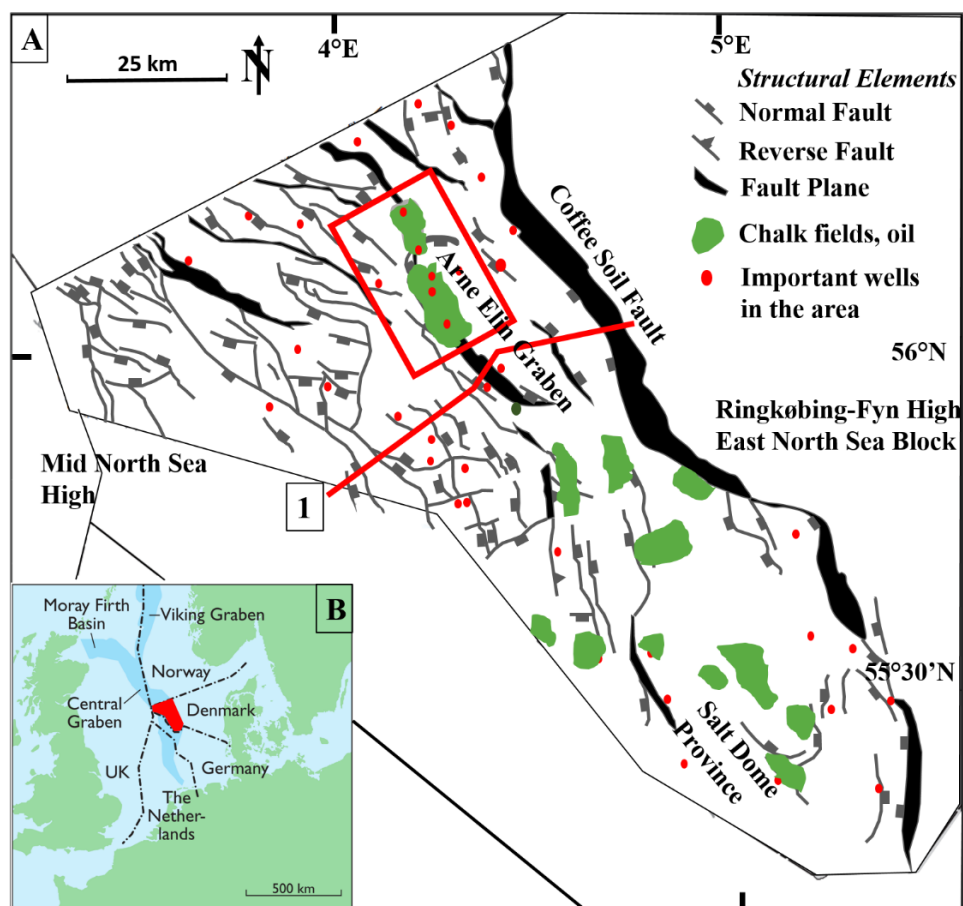


Figure 1 A. Map of the Danish North Sea showing the location of the South Arne Field (marked in as red square). The line 1 in the figure corresponds to the geological cross-sections in Figure 2. Modified from (Møller and Rasmussen, 2003) B. Inset box shows the location of the Danish North Sea (coloured in red) and international borders.

2. GEOLOGICAL SETTING

2.1. Regional Geology

The South Arne Field is located within the Danish sector of the Central Graben. The Central Graben is an intracratonic basin representing the southern arm of the North Sea rift system, which reaches into the Dutch, Germany, UK and Norwegian waters (de Vries, 2014). In the Dutch waters, this graben is known as the Dutch Central Graben. The Danish Central Graben consists of NNW-SSE trending half-grabens bounded towards the east by the Ringkøbing-Fyn High, and towards the west by the Mid North Sea High (Japsen et al., 2003) (Figures 1 and 2). The basement of the Central Graben is deformed by normal faults having large offsets, which results in a typical horst and graben system (Bishop, 1996). The graben formed due to rifting during the Triassic and Jurassic, followed by inversion in the Late Cretaceous and Cenozoic (Javed, 2012).

2.2. Tectonic Evolution

The basic structural framework of the Central Graben is mainly the result of Upper Jurassic/ Lower Cretaceous rifting, partly controlled by older structural elements (Halland et al., 2011). The following section gives an overview of the tectonic evolution of the Central Graben.

2.2.1. Carboniferous to Permian to Triassic

The first tectonic phase of the Central Graben can be dated back to the Later Carboniferous, when the Arctic-North Atlantic rift system initiated between Greenland and Scandinavia (de Vries, 2014). During this time, two basins developed with deposition of thick evaporite sequences (the Zechstein Group). Uneven loading of the younger sediments over the evaporite sequences initiated halokinetism. This was important for the generation of closed structures, including hydrocarbon traps (Halland et al., 2011). During the Early Triassic, the major N-S to NE-SW rifting between Greenland and Scandinavia intensified, which resulted in the development of the Viking Graben and Central Graben.

2.2.2. Jurassic to Cretaceous

The rift pulses developed during the Later Jurassic and the Early Cretaceous causing differential movement, uplift and tilting of fault blocks. They caused the Permian salt to remobilize and form a number of salt pillows and salt diapirs in the northern and the southern dome provinces of the Central Graben (de Vries, 2014). During the Early Cretaceous, the opening of the Atlantic Ocean changed the regional stress regime, making the horizontal stress more in an E-W direction, thus leading to transpressional movements along the NNW-SSE oriented faults (Gennaro, 2011). During the Late Cretaceous, there was a reduced influx of clastic material and an overall deposition of

chalk in the entire North Sea area. Chalk deposition extended until Tertiary, showing variable thickness across the Salt Dome provinces (Halland et al., 2011).

2.2.3. Tertiary to Quaternary

At the end of the Late Cretaceous and throughout the Paleogene, NNE-SSW compressional tectonic events happened in the Central Graben Area (de Vries, 2014). Subsidence and sedimentation continued in many areas leading to erosion of uplifted blocks. These processes are the main reason for salt tectonics in the Central Graben, which continued into the Holocene (Gautier, 2005). Salt tectonics played a key role in the accumulation of hydrocarbons in the Chalk Group (Vejbæk and Andersen, 2002).

2.3. Arne-Elin Ridge

The Arne-Elin Ridge is one of the several ridges within the Central Graben. It separates the Heno Plateau from the Tail End Graben (Japsen et al., 2003) (Figure 2). During the Late Jurassic, increased fault activity resulted in the generation of several minor sub-basins, including the Arne-Elin Graben (Andsbjerg and Dybkjær, 2003). The Subsidence during this time was concentrated along NNW-SSE trending faults (Møller and Rasmussen, 2003). As a result of Late Cretaceous inversion, the Arne-Elin Graben changed from a depocentre to a structural high, resulting in the uplift of the Arne-Elin Ridge (Vejbæk and Andersen, 2002).

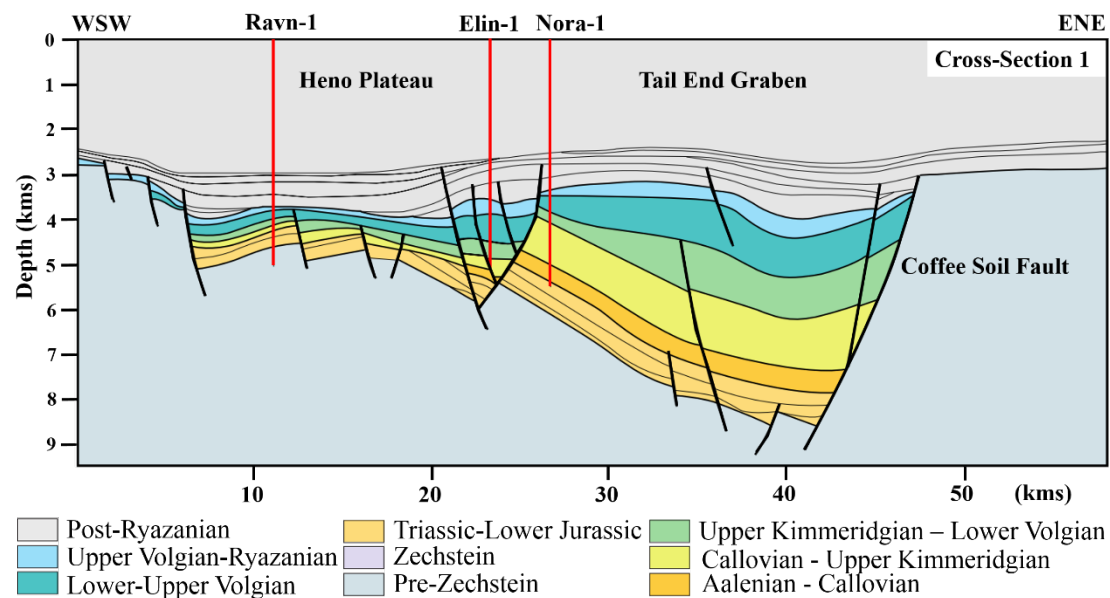


Figure 2 The cross-section across the mid southern part of the Danish Central Graben (Møller and Rasmussen, 2003). See Figure 1 for location of the cross-section.

2.4. South Arne Field

2.4.1. Structural Setting

The South Arne field is located in the Danish North Sea. The field lies at a depth between 2700-2940 meters subsea. The double dipping anticline was formed during the Late Cretaceous to Early Paleocene and the structure is interpreted to be the result of oblique inversion along NNW-SSE basement faults of the Arne-Elin Graben. These faults are of listric nature and characterized by post-depositional inversion during the Late Cretaceous. The northern part of the anticline is characterized by crestal collapse, caused by the withdrawal of Zechstein salt during the Early Paleocene age (Astratti et al., 2015). The oblique movements led to the formation of WNW-ESE faults which are the most distinct structural trend within the chalk on the 3D seismic data, except in the area obscured by a near-surface gas cloud (Herwanger et al., 2010). According to Mackertich and Goulding (1999), a third structural trend is represented by two NNE-SSW lineaments without a clear offset on the seismic sections, presumed to act as significant stratigraphic boundaries during the chalk deposition.

2.4.2. Stratigraphy

The chronostratigraphy of the South Arne Field ranges from the Lower Cretaceous to Middle Paleocene (Figure 3). The Chalk Group (i.e. Ekofisk Formation and Tor Formation) are the two most important reservoirs of the South Arne field and the Central Graben (Lindgreen et al., 2012). The Tor Formation of Maastrichtian age is overlain by the Ekofisk Formation of Danian age. These two reservoirs are separated by a tight zone of reduced porosity, which is easily identified in the well logs (Figure 4). Chalk has been eroded along uplifted blocks, and re-deposited in the slope and the basin environments (McCann, 2008). Inversion tectonics has a significance role for chalk deposition because of the local uplift of fault blocks. The Tor Formation has higher porosity due to re-deposition (Kennedy, 1987). The reservoir is thinner towards the crest of the structure and as the chalk sequence thickens down dip, the porosity and permeability decrease considerably (Garcia and MacBeth, 2013) (Figure 5). Figure 5 also illustrates the varying extent of hydrocarbons on the eastern and western flank of the anticline. The thickness of the chalk varies from 60 metres at the crest and around 150 metres on the flanks of the structure (Mackertich and Goulding, 1999) (Figure 5). A study by Hardman (1982) shows that the amount of clay in the chalk is also of great importance in determining the capability of chalk to be a reservoir rock.

2.4.2.1. Tor Formation

The Tor Formation consists of Maastrichtian white to light grey, hard, chalky limestone (Figure 3). This formation is extensively deposited over the North Sea area. The thickness decreases in the uplifted areas and increases in local depocenters of the Central Graben. The upper boundary represents an unconformity between Cenozoic

and Mesozoic (McCann, 2008). The porosity ranges from 25 to 46% (Figure 4) and the permeability ranges from less than 1mD to 10 mD with an average of around 6 mD (Mackertich and Goulding, 1999). The upper member of the Tor Formation has high porosity due to homogenous chalk (Isaksen and Tonstad, 1989). The Tor Formation has a higher ratio of hydrocarbon reserves as compared to the Ekofisk Formation (McCann, 2008).

2.4.2.2. Ekofisk Formation

The Ekofisk Formation consists of Danian argillaceous chalk and chalky limestone (Figure 3). It is divided into upper and lower parts. The upper part of this formation is composed of homogenous chalks with low clay content (Isaksen and Tonstad, 1989). The lower part has low porosity with a higher terrigenous clay content acting as a barrier between the Tor and the Ekofisk formations and is called the Ekofisk Tight Zone (ETZ) (Isaksen and Tonstad, 1989) (Figure 4). The upper boundary defines the contact between the Ekofisk chalk and the overlying shale deposits. The lower boundary separates the Cretaceous and Tertiary chalks and represent an unconformity (Isaksen and Tonstad, 1989). The porosity ranges from 15 to 45 % and the permeability ranges from 1 mD to 4 mD (Mackertich and Goulding, 1999). The high porosity intervals (i.e. Ekofisk Formation and Tor Formation) are clearly delineated in well logs by a slow-down in P- and S- wave velocity and decrease in bulk density (Vejbæk et al., 2014) (Figure 4).

2.4.3. Fractures of South Arne

The existence of fractures in the South Arne reservoir enables high production rates, which would not have been possible from low matrix permeability sediments. Two generations of fractures are recognised by Mackertich and Goulding (1999) on cores and image logs from the South Arne wells. The older set of fractures is considered syndepositional and has been linked to the gravitational collapse of the semi-lithified chalk, whereas the younger set is developed after lithification in response to oblique inversion tectonics. Both sets of fractures were developed along the WNW-ESE structural trend and it is hard to separate them based on seismic data (Astratti et al., 2015). The study by Mackertich and Goulding (1999) revealed that the WNW-ESE fault trends mapped on 3D seismic data in the South Arne are also the dominant fracture strike trends in the wellbore data. However, image log analysis shows a wider azimuth distribution of fracture strike than the seismic data does (Mackertich and Goulding, 1999).

Astratti et al. (2015) analysed each structural trend on the seismic data with the aim of detecting the azimuthal dispersion of the fractures described in the borehole. They confirmed the WNW-ESE lineaments as the dominant structural feature within the

chalk. The North-South lineament trend is weaker than the WNW-ESE lineament trend, but the strongest lineament belonging to this set corresponds to the eastern shoulder of the Crestal Graben, north of the gas cloud. The NW-SE present-day maximum horizontal stress direction suggests that the ENE-WSW and NNE-SSW orientations might be closed, which would form barriers to the fluid flow (Astratti et al., 2015). Figure 6 illustrates the main structural elements in the Chalk of the South Arne Field. Note the high fracture density over the crest of the field.

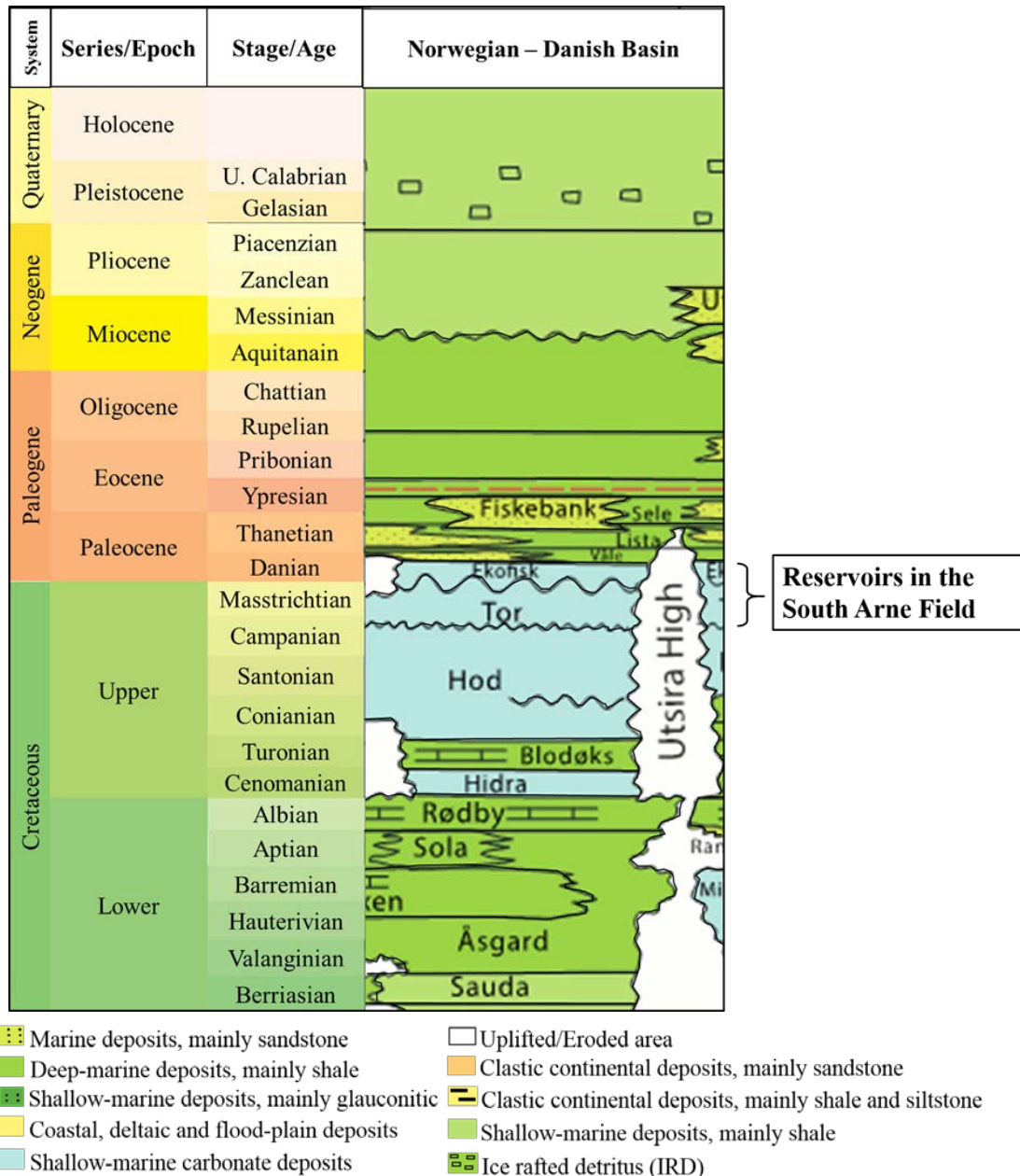


Figure 3 Lithostratigraphic summary for the Central Graben. Modified from Halland et al. (2011).

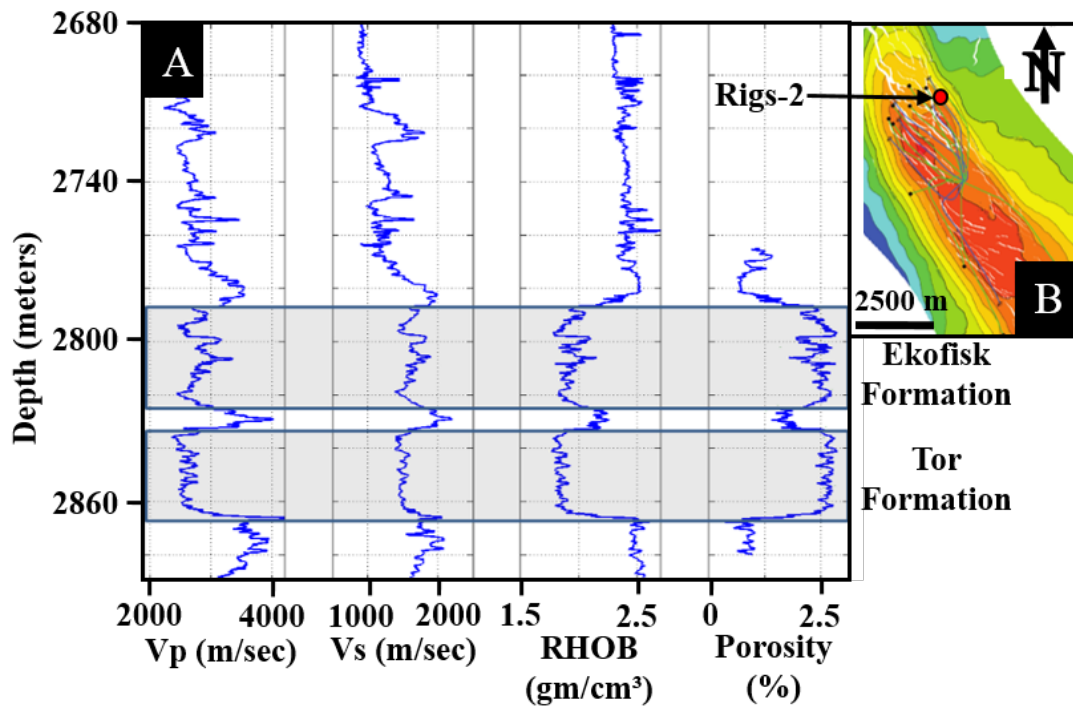


Figure 4 A. Bulk density (RHOB), compressional wave velocity (V_p), shear wave velocity (V_s), and porosity log of the Rigs-2 well. Note the high porosity in both the Ekofisk (upper reservoir) and Tor (lower reservoir) formations. Porosity is more homogenous in the Tor Formation than in the Ekofisk Formation. The Ekofisk Tight Zone (ETZ) is characterised in the logs by low porosity and high P- and S- wave velocity. B. Location of Rigs-2 well displayed on top Ekofisk surface. Modified from Vejbaek et al. (2014).

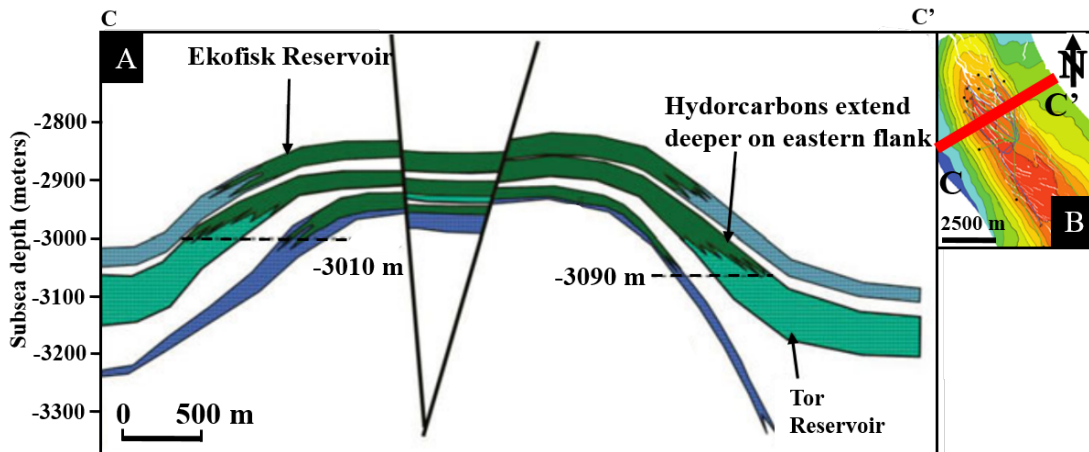


Figure 5 A. A schematic cross-section through the field of study showing the Ekofisk and Tor reservoirs. Note the thickness variation over the crest and the flanks of the structure. B. Top Ekofisk surface with navigation of cross section C-C' shown in A. Modified from Garcia and MacBeth (2013).

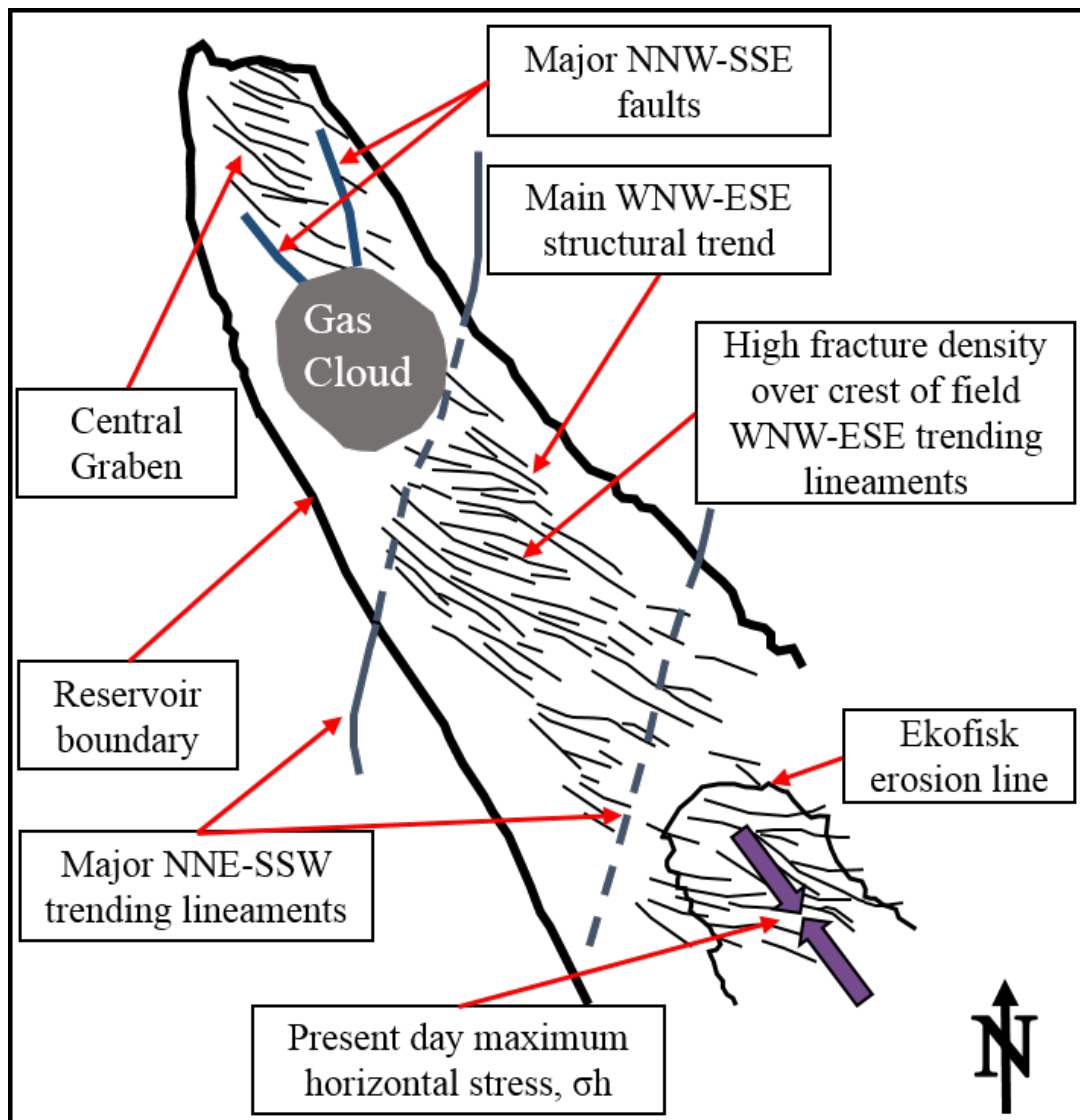


Figure 6 Outline of the main structural elements in the Chalk of the South Arne Field. Modified from Astratti et al. (2015).

Tectonic fractures are considered the most important type of fractures in the South Arne field because of their contribution to the increased permeability of the reservoir. The majority of tectonic fractures in outcrops tend to be shear fractures. In image logs, these fractures commonly have high dip angles (60°-80°) (Mackertich and Goulding, 1999). The fracture study done by Mackertich and Goulding (1999) for the field, revealed the different types of fractures developing in different lithofacies. Hairline fractures are common in the Tor Formation, but they are difficult to detect on image logs because of the lack of resistivity contrast. They are generally less porous and permeable. These fractures are absent from the Ekofisk Formation. In the Ekofisk Tight Zone, the fractures tend to be of low angle and listric in nature.

The clay content of the chalk is a crucial factor as it is considered to influence the frequency of fractures (Mackertich and Goulding, 1999). A study done by Hardman (1982) shows that the porous, clay-poor rock shows a higher intensity of fracturing than the clay-rich rock. This is particularly important since the Tor Formation is re-sedimented chalk and re-sedimentation generally leads to a break up of early cement due to debris flow or suspension; hence the intensity of fracturing is greater in the Tor Formation (Hardman, 1982). Hardman (1982) also shows that fracturing is intense where the chalk is thinnest. A similar relation is also observed with fracture intensity, as fracture intensity is maximum where the uplift (and curvature) is maximum, and the chalk thickness is minimum (Hardman, 1982).

3. DATASET

Hess Denmark provides the dataset of the South Arne field used in this study. The dataset consists of a 3D seismic survey and well data.

3.1. Seismic Data

The seismic 3D survey was shot in 1995. The survey consists of seven hundred in-lines in the NNE-SSW direction and nine hundred cross-lines in the WNW-ESE direction. The total coverage of the seismic cube is approximately 100 km². The maximum two way-travel time is 4500 milli-second. The northern part of the seismic is affected by a shallow gas cloud in the overburden, leading to strong amplitude attenuation and poor quality seismic data (Figure 7). The gas cloud obscures the seismic image of the crest of the structure. Fault reactivation in the Miocene allowed the gas to leak into the overburden (Astratti et al., 2015). The gas cloud is characterised by high amplitudes, absorbing most of the seismic energy beneath it, and making the identification and interpretation of geological structures underneath difficult. The reservoir lies above the salt dome on the crest of the structure. Near (5° - 15°), mid (15° - 25°) and far (25° - 35°) angle stacks seismic are available along with the full-stack seismic. The data also include the velocity cube for the time-to-depth relationship. An inspection of the four cubes shows that the near-angle stack delivers the clearest image of the sub-surface structures compared to the full-stack and the other angle stacks.

3.2. Well Data

The well data consists of check shot surveys, well logs and fracture point data. The logs that are important for this study are summarised in Table 1. It is worthwhile mentioning that all the logs (i.e. RHOB, Vp and Vs) that are needed for rock physics studies and calculation of the rock moduli for comparison with the measured fracture intensity are available for well SA-1A (Figure 8). Most of the horizontal wells are drilled along the NNW-SSE axis of the structure (i.e. parallel to the natural fracture orientation) (Figure 8 and Table 1). Figure 8 illustrates that most of the wells are drilled north of the gas cloud in the collapsed structure. Rigs-1 well is drilled beneath the gas cloud.

3.2.1. Fracture Data

As summarised in Table 1, thirteen wells have fracture point data, which are based on interpretation of formation micro-imager (FMI) logs. The fracture points are available in the form of depth, dip, azimuth and fracture classification (conductive fractures, resistive fractures, and faults). As an example, the fractures of the well SA-1A are displayed in a stereo-net showing the fracture strikes and fracture dip azimuths as points in Figure 9. Fracture points are colour-coded with the dip-azimuth attribute. Also shown

are the fracture azimuths in the form of rose-diagrams. Note the large scattering of the dip and the fracture azimuth.

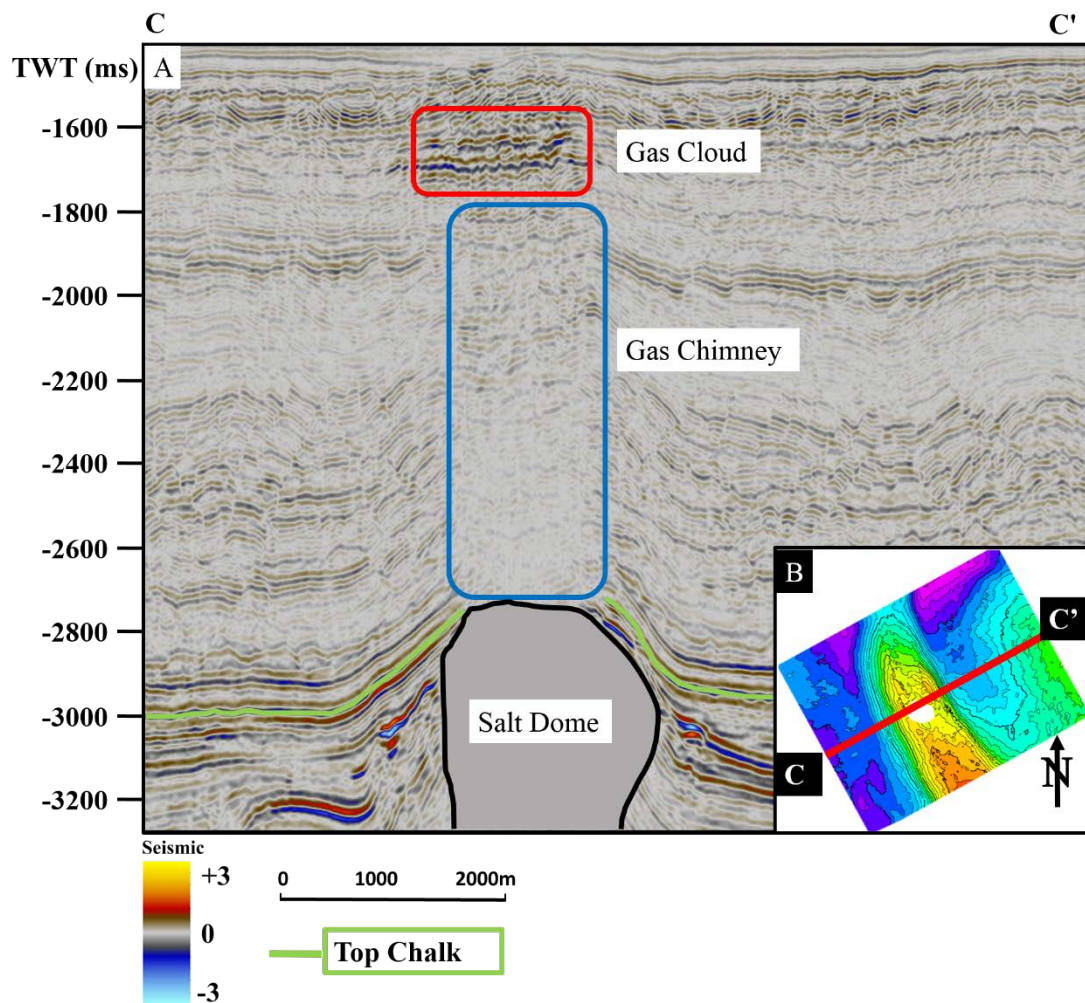


Figure 7. A. Seismic section showing the salt dome, gas chimney (marked in blue) and gas cloud (marked in red) in the overburden along with the interpreted top reservoir (Top Ekofisk). B. Top Ekofisk surface with navigation of cross section C-C' shown in A.

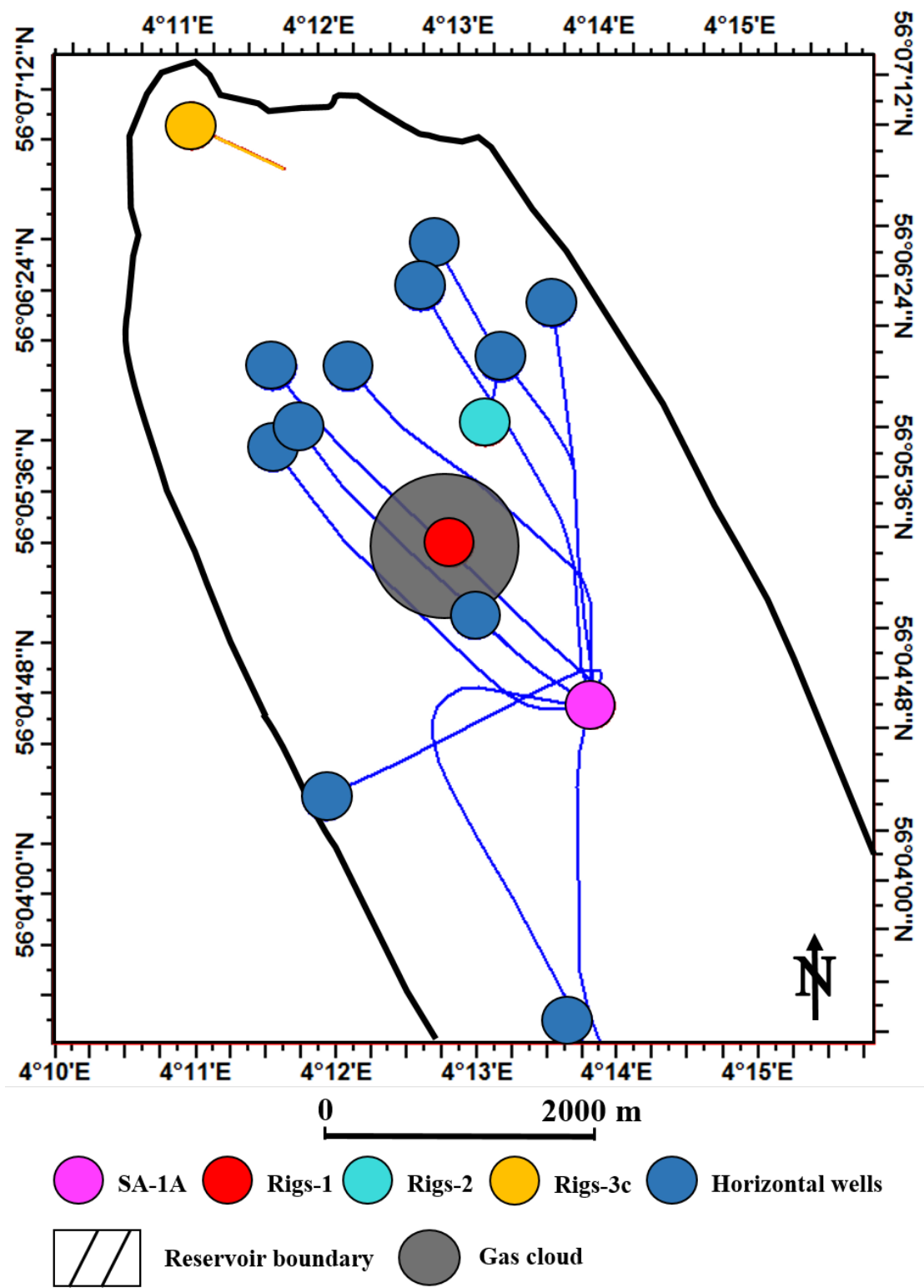


Figure 8 Trajectories of the horizontal wells and vertical wells along with the reservoir boundary. Most of the wells are horizontal. Well names are displayed for few wells only (Table 1).

Table 1. Available wells of the study area along with well type, and different well data present in the well (Green colour represents data is present, red colour represents data is absent). All the data is present for well SA-1A.

Well name/ Dataset	Well type (Horizontal/ Vertical)	DT (Compressional sonic travel time)	DTS (Shear sonic travel time)	RHOB (Density Log)	NPHI (Neutron Log)	Fracture Data
Rigs- 1	Vertical	Green	Green	Green	Green	Red
Rigs-2	Vertical	Green	Green	Green	Green	Red
Rigs-2a	Horizontal	Green	Green	Green	Green	Red
Rigs-3c	Vertical	Green	Green	Green	Green	Red
SA-1A	Vertical	Green	Green	Green	Green	Green
SA-6B	Horizontal	Green	Red	Green	Green	Green
SA-2	Horizontal	Green	Red	Green	Green	Green
SA-4A	Horizontal	Red	Red	Green	Green	Green
SA-5B	Horizontal	Red	Red	Green	Green	Green
SA-7	Horizontal	Red	Red	Green	Green	Green
SA-9	Horizontal	Red	Red	Green	Green	Green
SA-3A	Horizontal	Green	Red	Green	Green	Green
SA-1B	Horizontal	Red	Green	Green	Green	Green
SA-8A	Horizontal	Red	Red	Green	Green	Green
SA-8B	Horizontal	Red	Red	Green	Green	Green
SA-8D	Horizontal	Red	Red	Green	Green	Green
SA-8E	Horizontal	Red	Red	Green	Green	Green
SA-8H	Horizontal	Red	Red	Green	Green	Green
SA-6C	Horizontal	Red	Red	Green	Green	Green

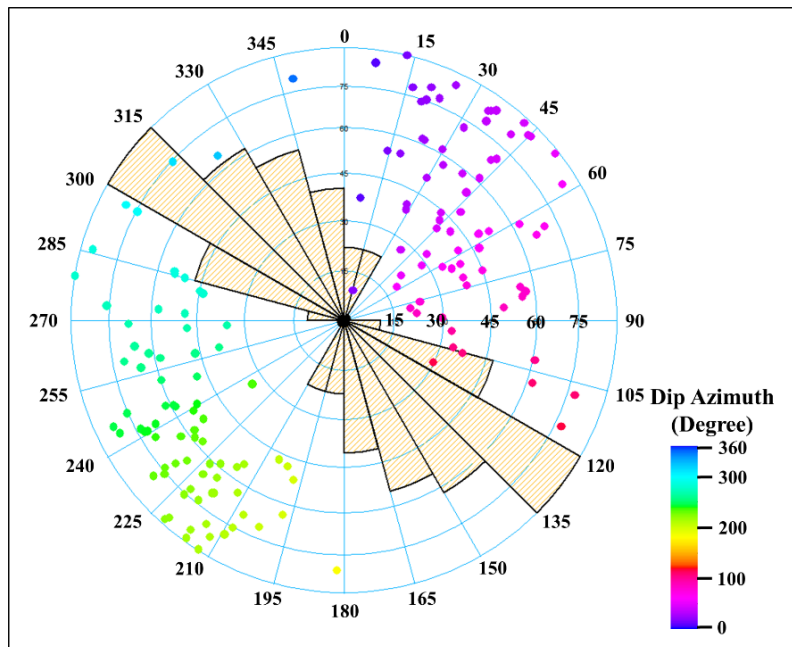


Figure 9 Stereo-net plot with well data from well SA-1A displaying the dip azimuth (points) and strike attribute (shaded area) of the fracture data. For the location of the well SA-1A, refer to Figure 8.

4. THEORY AND BACKGROUND

4.1. Fractures

A fracture can be described as a discontinuity that breaks the rock along cracks, fissures, or joints, and along which there is no displacement parallel to the planes of discontinuity (Van Golf-Racht, 1982). Fractures form when the applied stress reaches the yielding threshold, i.e. the stress at which the rock breaks. Fractures can be separated into shear, extension and, tension fractures. All brittle fracture in rock conforms to one of the above basic fracture types.

Shear Fractures

A shear fracture is a fracture along which the relative movement is parallel to the fracture plane, but there is no perpendicular movement (Figure 10). They form at an acute angle to the maximum compressive stress (σ_1) and at an obtuse angle to the minimum compressive stress (σ_3). The acute angle between two shear fractures is called the conjugate angle. The angle between the shear fracture and σ_1 is called the dihedral angle (Bratton et al., 2006) (Figure 10). Shear fractures form when all three principal stresses are compressive (Nelson, 2001). The orientation of shear fractures can be predicted from the knowledge of the orientation of the fault (Stearns and Friedman, 1972). Shear fractures are developed in conjugate sets (Figure 10).

Extension Fractures

Extension fractures have a sense of displacement perpendicular to and away from the fracture plane. They form parallel to σ_1 and σ_2 and perpendicular to σ_3 (Figure 10). These fractures also form when all three principal stresses are compressive (Nelson, 2001). All three principal stresses must be positive to form an extension fracture.

Tension Fractures

Tension fractures also have a sense of displacement perpendicular to and away from the fracture plane and form parallel to σ_1 and σ_2 (Nelson, 2001) (Figure 10). These fractures resemble extension fractures concerning the sense of displacement. However, at least one principal stress (σ_3) must be negative in case of tension fractures and rocks have a much lower fracture strength in tension than in extension (Nelson, 2001). Stylolites are highly irregular surfaces in a rock body that are the result of pressure dissolution (Figure 10). Stylolites are characterised as fractures perpendicular to the maximum stress (Bratton et al., 2006).

A reservoir fracture is a naturally occurring macroscopic planar discontinuity in the rock due to deformation or physical diagenesis. In case of open fractures, they may have a significant effect on reservoir fluid flow due to increased reservoir permeability

or increased porosity or both (Nelson, 2001). A fractured reservoir is defined as a reservoir in which naturally occurring fractures either have or are expected to have, a significant effect on reservoir fluid flow either in the form of increased reservoir permeability or increased permeability anisotropy (Nelson, 2001).

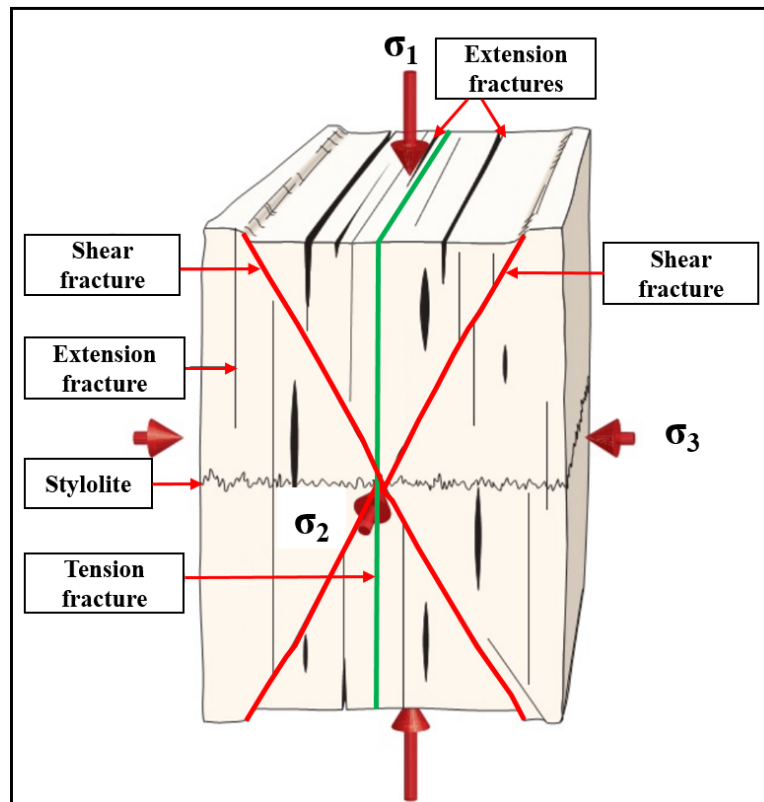


Figure 10 The orientation of various fracture types with respect to the principal stresses. Tension fractures (green) form parallel to σ_1 and σ_2 . The acute angle between two shear fractures (red) is called the conjugate angle. The angle between the shear fracture and σ_1 is called the dihedral angle. Modified from Bratton et al. (2006).

It is of vital importance to identify and categorise the type of fracture system in the reservoir once the reservoir properties of the fracture system are identified. Fractured reservoirs are classified based on the contributions from both the fracture and the matrix systems and the interactions between the relative porosity and the permeability (Figure 11). The classification given by Nelson (2001) (Figure 11) is useful in this regard. In Type I reservoirs, fractures provide both primary porosity and permeability. Type II reservoirs have low porosity and low permeability in the matrix, and fractures provide the essential reservoir permeability. In this case, the influence of the fracture porosity decreases as the matrix porosity increases. In Type III reservoirs, fractures do not contribute significantly to the reservoir porosity and permeability. Type M reservoirs have high matrix porosity and permeability, and natural fractures impede fluid flow in these reservoirs by forming barriers. Type IV reservoir would plot at the origin in Figure 11 because the fracture contribution to permeability in these reservoirs is negative. It is

worthwhile mentioning that the South Arne reservoir is a type III fractured reservoir, where fractures merely enhance the fracture permeability (Luthje et al., 2013).

The origin of fracture system is theorised from the data on fracture dip and strike, layer morphology, relative abundance, and the angular relationships between fracture sets. It is assumed that natural fractural patterns represent the local state of stress at the time of fracturing.

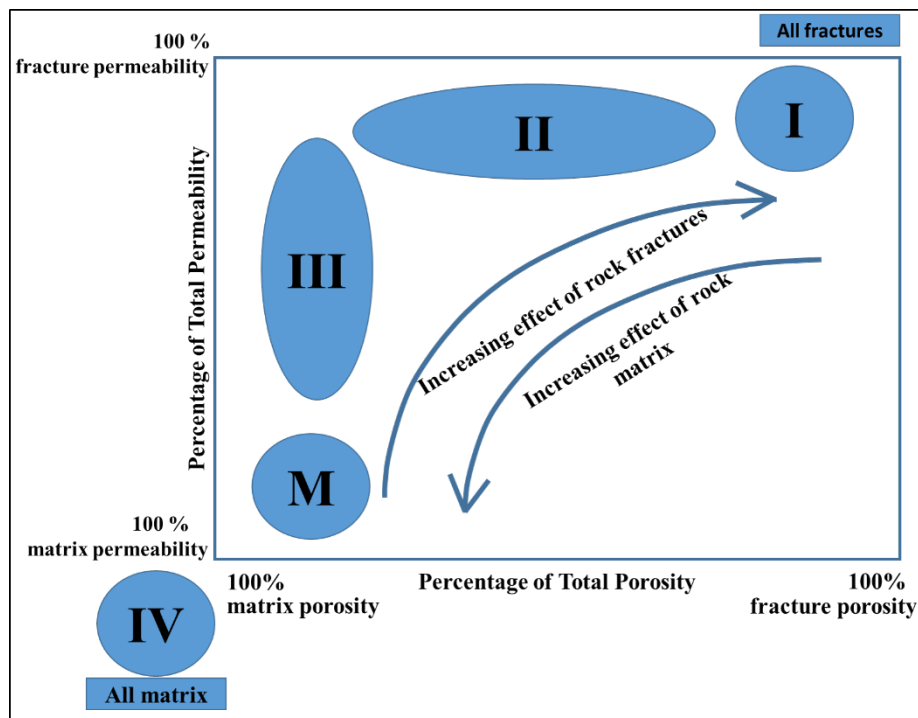


Figure 11 Illustration of different types of fractures with respect to the relation between rock matrix porosity and permeability with the fracture porosity and fracture permeability. Modified from Nelson (2001).

4.1.1. Fractures Associated with faults

Fractures often form as an additional feature spatially related to other structures. The intensity of fracturing associated with faulting depends on lithology, distance from the fault location, amount of displacement along the fault, and total strain in the rock mass (Nelson, 2001). The majority of fractures developed in the vicinity of faults are shear fractures parallel to the fault, shear fractures conjugate to the fault, or extension fractures bisecting the acute angle between these two shear directions (Nelson, 2001). Figure 12 illustrates the rose diagram of conjugate shear fractures associated with a normal fault. This concept was also explained by Trice (2014) in his study of the fractured basement of the West of Shetlands (Figure 13). This figure illustrates the conceptual model of a basement reservoir, in which the amount of fractures is dependent on the distance from the fault zone.

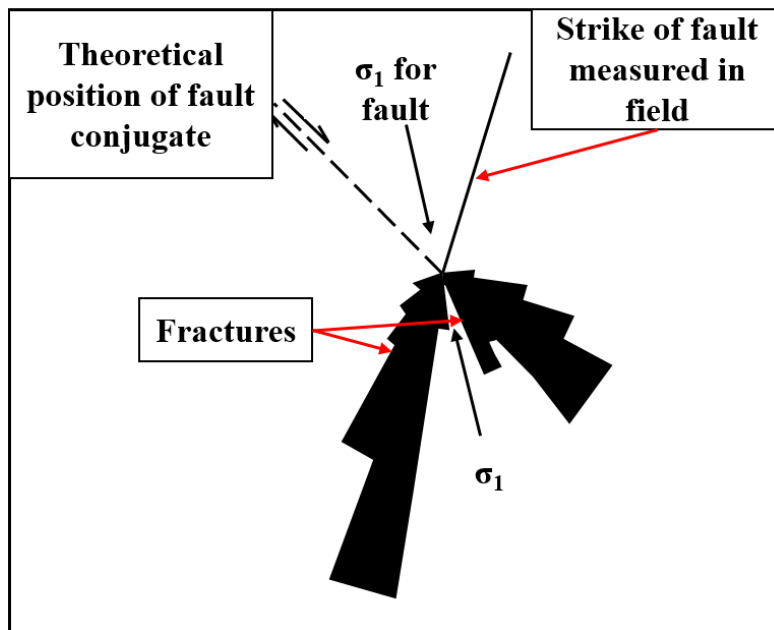


Figure 12 Rose diagram of shear fractures associated with a normal fault. Modified from Nelson (2001)

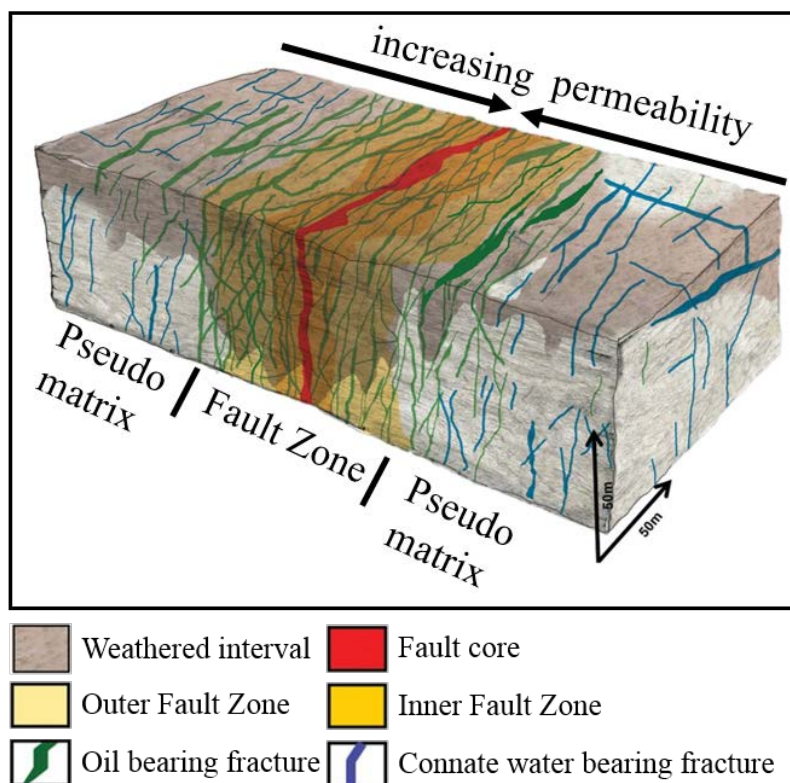


Figure 13 Conceptual model of basement reservoir within the structural closure. The reservoir is divided into three zones: (1) an Inner Fault Zone; (2) an Outer Fault Zone (both of which combine to make up a Fault Zone); and (3) a pseudo matrix (Trice, 2014).

4.2. Fracture Properties

4.2.1. Fracture Aperture

Fracture aperture is the perpendicular distance separating the adjacent rock walls of an open fracture (Singhal and Gupta, 2010). The intervening space in the open discontinuity is air-, water- or hydrocarbon-filled. This parameter is subject to high uncertainty because of the difficulty to derive it reliably. It is measured directly from FMI images, taken from core samples, or estimated based on hydraulic tests. Shear fractures have lower aperture value than tensile fractures (Singhal and Gupta, 2010). The aperture may vary from very tight to wide (Table 2). Table 2 gives aperture ranges and their classifications.

Table 2 Aperture classification by size (Singhal and Gupta, 2010).

Aperture (mm)	Term
< 0.1	Very tight
0.1 - 0.25	Tight
0.25 - 0.50	Partly open
0.50 – 2.50	Open
2-50 – 10.0	Moderately wide
> 10.0	Wide

4.2.2. Fracture Spacing

Fracture spacing is defined as the distance between regularly spaced fractures measured perpendicular to a parallel set of fractures of a given orientation (Singhal and Gupta, 2010). It is related to lithology and thickness of bed, and is given as (Price and Cosgrove, 1990):

$$fs = Y \cdot b \quad (1)$$

where:

fs = Fracture spacing

Y = constant related to lithology

b = thickness of the bed

Figure 14 illustrates the proportional increase in fracture spacing with bed thickness. It also illustrates that with constant bed thickness, fracture spacing varies with different lithologies.

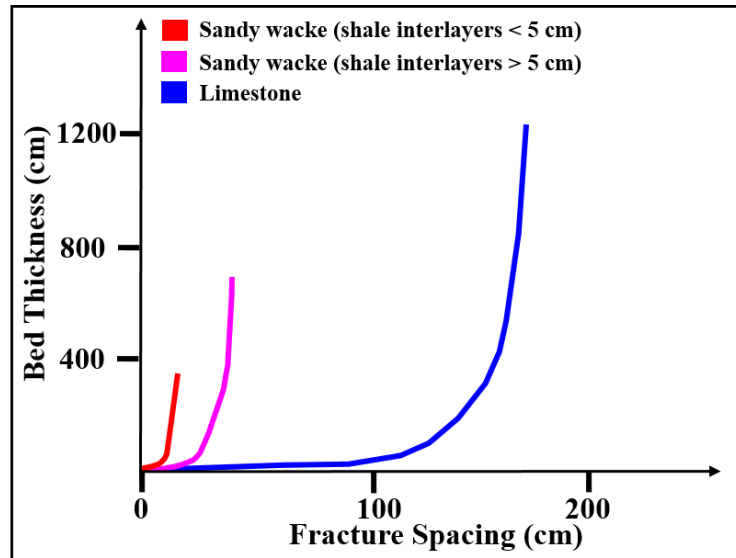


Figure 14 Graph illustrating the relationship between fracture spacing and bed thickness for varying lithologies. Modified from Twiss and Moores (1992)

4.2.3. Fracture Porosity

Fracture porosity is a secondary porosity developed by the fracturing of rocks. Fracture porosity, like matrix porosity, is the percentage of a particular void volume in a rock mass compared to its total volume (Nelson, 2001). It considers only those voids occurring between the walls of fractures. On the other hand, matrix porosity accounts for all voids within a rock except those within fractures (Nelson, 2001). The relationships used to calculate fracture porosity and matrix porosity are presented in Equations (2) and (3) respectively:

$$\phi f = \frac{e}{D+e} * 100 \quad (2)$$

$$\phi m = \frac{Vp}{Vb} * 100 \quad (3)$$

where:

ϕf = fracture porosity

ϕm = matrix porosity

e = average effective width of fractures

D = average spacing between parallel fractures

Vp = volume of pores (other than fractures)

Vb = bulk volume

Equation (2) and (3) lead to the interesting conclusion that the fracture porosity is scale dependent while matrix porosity is not. Nelson (2001) showed this as illustrated in Figure 15. Figure 15-I is an outcrop where fracture porosity and matrix porosity are

calculated. Figure 15-II represents a small area (1 cm²) of an outcrop between fractures. In this case, fracture porosity would be zero. Figure 15-III represents another area of the same size (1 cm²) of an outcrop located over a fracture. In this case, fracture porosity would be quite large, and matrix porosity would be approximately equal to the previous case. This shows that as the size of the sampling window increases, more fractures are encountered, and fracture porosity approaches a more truly representative number. This implies that a sampling window encountering several fractures is required to assess fracture porosity and consequently fracture properties accurately.

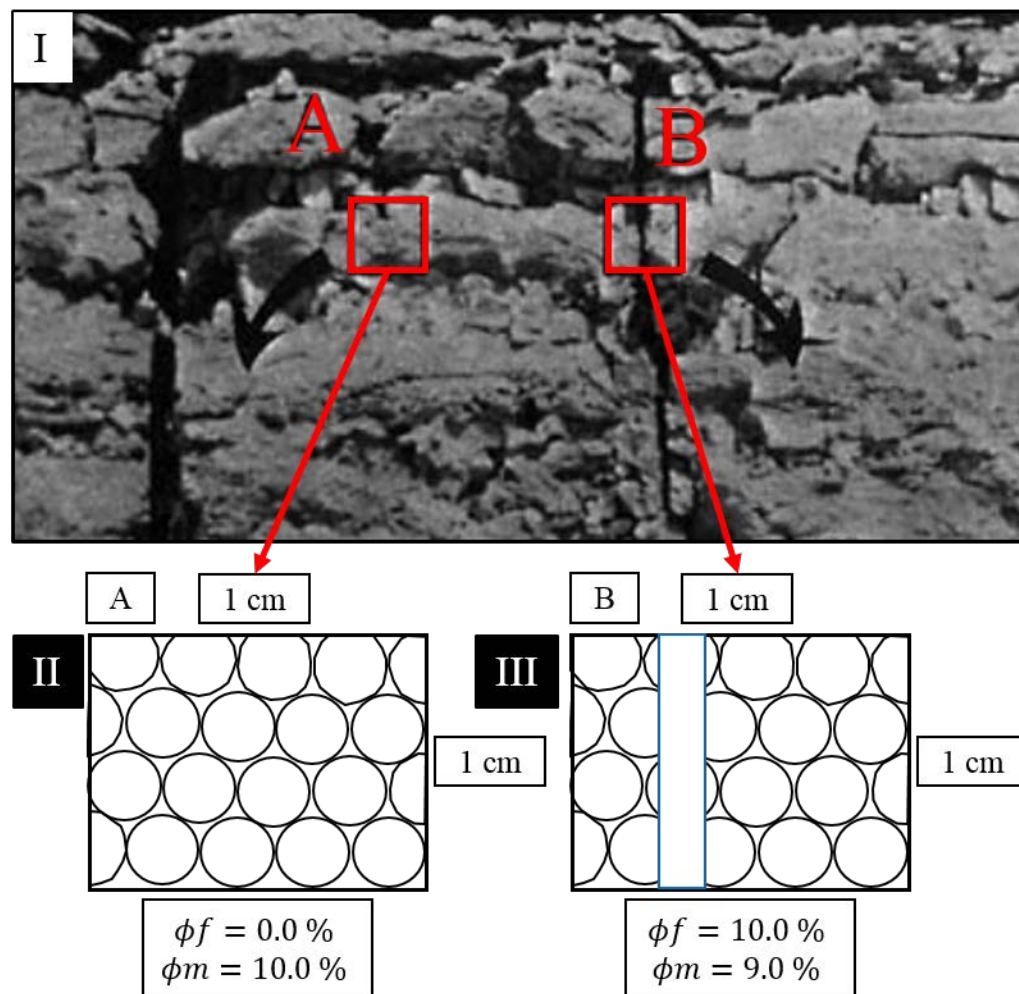


Figure 15 I. An outcrop of rock where fracture porosity and matrix porosity are calculated. II. A small element of an outcrop of area 1 cm² located between fractures. III. A small element of an outcrop of area 1 cm² located over a fracture. The blue line represents a fracture. Note the change in fracture porosity between the two equal areas. Modified from Nelson (2001).

4.2.4. Fracture Permeability

A proper quantification of a reservoir is always challenging, especially during exploration because of lack of data. Understanding subsurface fracture width and its

link to permeability is necessary for an early understanding of the fractured reservoir performance (Nelson, 2001).

The quantitative description of fluid flow Q through porous media was introduced by Darcy (1856) (Nelson, 2001). However, it was later realised that this so-called Darcy equation does not hold true for flow within fractures. Therefore, the parallel-plate theory of flow was developed to describe fracture flow. According to this theory, flow is assumed to occur between two smooth parallel plates separated by a distance e (Figure 16; Equation 4). Figure 16-A illustrates the fluid flow through a fractured material. Asperities (Figure 16-A) are the irregularities within the fracture walls. They reduce the fluid flow, fluid porosity and make fluid velocities irregular (Singhal and Gupta, 2010).

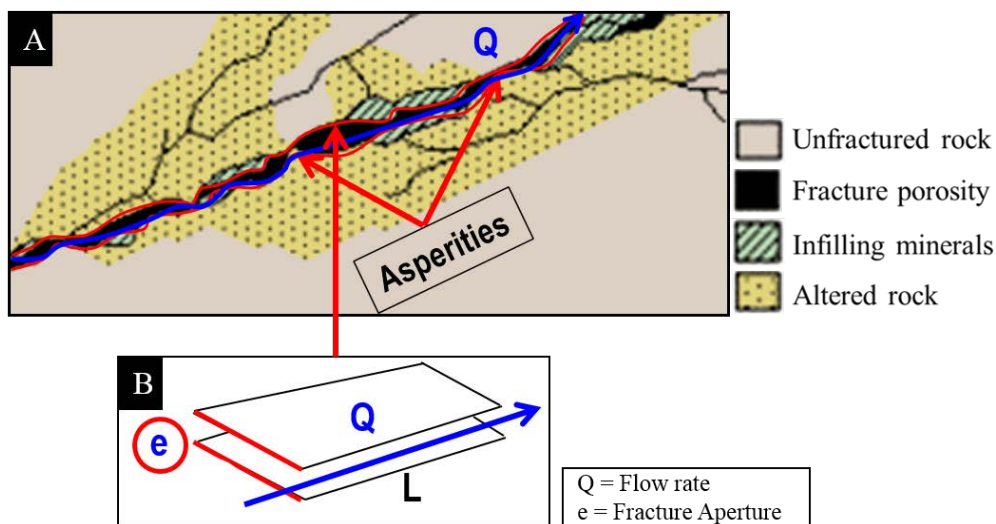


Figure 16 A. Fracture model illustrating infilling materials, alteration and fracture porosity. B. Figure illustrating how flow rate Q is dependent on fracture aperture e . Modified from Paillet and Kapucu (1989).

$$\frac{Q}{A} = \frac{e^3}{12D} \cdot \frac{dh}{dl} \cdot \frac{\rho g}{\mu} \quad (4)$$

where:

Q = flow rate (cm²/sec)

A = cross-sectional area (cm²)

e = fracture aperture (cm)

D = fracture spacing, the average distance between parallel regularly spaced fractures (cm)

ρ = fluid density (g/cm)

g = acceleration due to gravity

μ = fluid viscosity (g/cm.s)

$$\frac{dh}{dl} = \text{head gradient}$$

Equation (4) shows that the flow rate is directly proportional to the cube of the fracture aperture (also known as cubic law), and inversely proportional to the fracture spacing. The permeability decreases with the roughness of the fracture surfaces, i.e. where the flow is turbulent (Stearns and Friedman, 1972). This means that the impact of the fracture system is expected to be greatest where the reservoir contains wide, closely spaced, smooth fractures.

4.3. Rock Physics Properties, Elasticity and Fracture Relationship

Based on the behaviour of rocks under the influence of increasing stress, two different rock classes are defined, i.e. ductile and brittle. Brittle rocks are unable to withstand significant strain before failure and consequently fracture quickly. Typically, they exhibit both naturally occurring and hydraulically induced fractures. In contrast, ductile rocks deform plastically and can undergo significant strain before fracturing (Altimar, 2013).

A study by Mavko (2000) shows how fractures occur primarily in brittle rocks, characterised by low Gamma-Ray values (Figure 17). The study underlines the importance of understanding the reservoir heterogeneity, especially fractures, which may influence the seismic properties (i.e. V_p and V_s). Figure 17 illustrates the different reservoir properties (i.e. GR, V_p and V_s) affected by the number of fractures in a reservoir. It also shows that higher P- and S-wave velocities characterise the fracture zones.

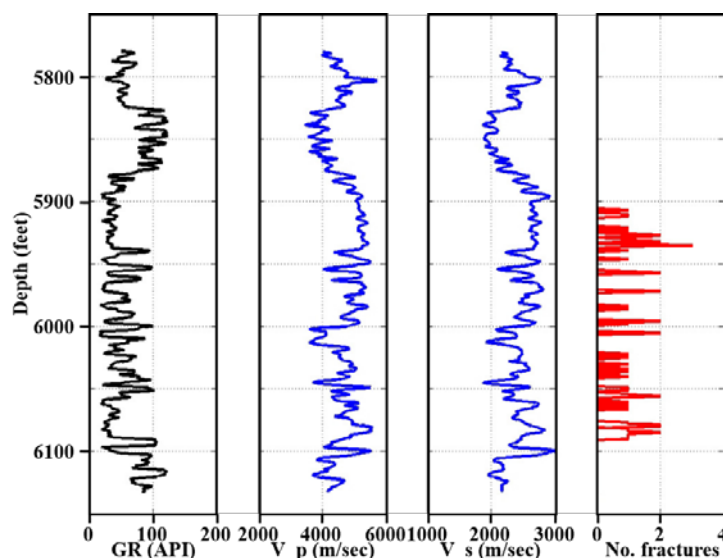


Figure 17 Well-log data over a depth interval corresponding to a limestone reservoir. The first, second, third and fourth columns correspond to Gamma-Ray, P-wave velocity, S-wave velocity and the number of fractures per foot interpreted from FMI data respectively. Modified from Mavko (2000).

The crucial elastic parameter used in rock mechanics is the Young Modulus. The Young Modulus (E) is a measure of the stiffness of a given material (Al-anazi et al., 2011). It is also known as Modulus of Elasticity, Elastic Modulus, and Tensile or Compression Moduli. When a force is applied to a solid, the length of the solid changes. The Young Modulus is defined as the constant of proportion that relates the stress to the strain. It is defined in terms of the proportional change in length of the solid (Figure 18). The relationship is written as:

$$\sigma = E(\Delta l/l) \quad (5)$$

where:

σ = stress expressed as a pressure

$\frac{\Delta l}{l}$ = fractional change in length

E = Young Modulus

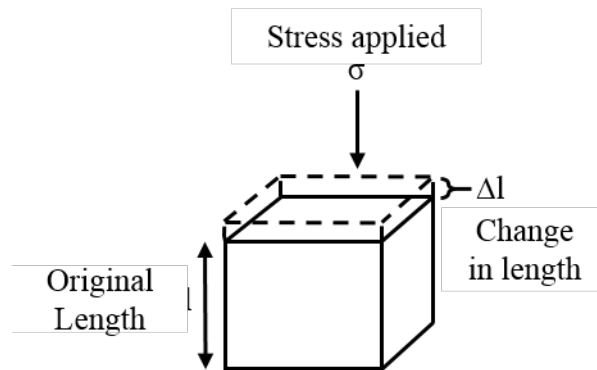


Figure 18 Change in length of the material as a result of applied stress.

Previous studies have pointed out the relationship between fracture intensity and lithology (Stearns and Friedman, 1972; Nelson, 2001; Figure 19). In general, rocks of high brittle constituents will have closer-spaced fractures than ductile rocks. Limestone has low Young Modulus values and consequently a low fracture number. On the other hand, dolomite, a brittle material, has high Young Modulus and a high fracture number. This implies that the fracture intensity of a specific lithology is linked to the Young Modulus.

A non-linear relationship of porosity with rock strength is documented by Dunn et al. (1973) (Figure 20-A). According to this relationship the rock strength decreases with increasing porosity. Another study by Nelson (2001) highlights the relationship between porosity and fracture intensity in a dolomite (Figure 20-B). Low porosity rocks have more fractures than relatively higher porosity rocks. Another study by Xu et al. (2016) on sandstone and mudstone concluded that a positive correlation exists between rock strength and Young Modulus (Figure 20-C). At the same Young Modulus values,

the compressive strength of sandstone is larger than that of mudstone. Figure 20 shows that the fracture intensity is related to properties such as porosity and Young Modulus.

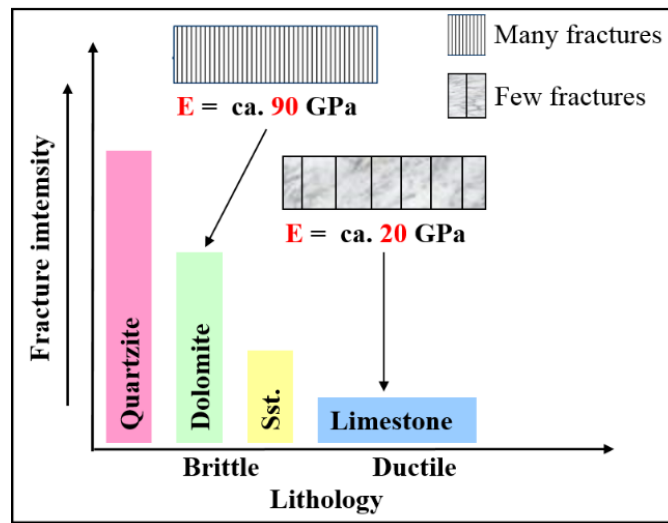


Figure 19 Average fracture number for several common rock types naturally deformed in the same physical environment. Modified from Stearns and Friedman (1972).

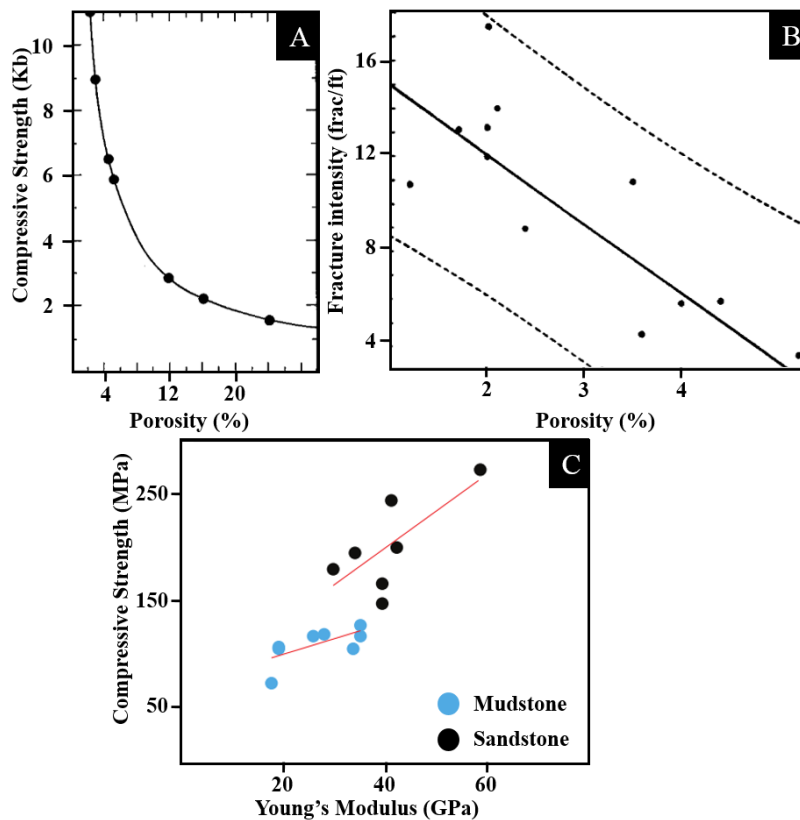


Figure 20 A. Compressive strength as a function of porosity. Modified from Dunn et al. (1973). B. Outcrop measurements of fracture intensity and corresponding porosity in a dolomite. Note the decreasing fracture intensity with increasing porosity. Modified from Nelson (2001). C. Relationship between compressive strength and Young Modulus. Modified from (Xu et al., 2016).

4.4. Seismic Inversion

Seismic inversion is a procedure involving the conversion of an interface property (i.e. a reflection) to a rock property known as impedance, which itself is the multiplication of sonic velocity and bulk density (Figure 21). In this methodology, the impedance values are correlated to internal rock properties, such as lithology type, porosity or the fluid type in the rocks (Francis, 2014). Consequently, inverted data is most suitable for reservoir characterisation.

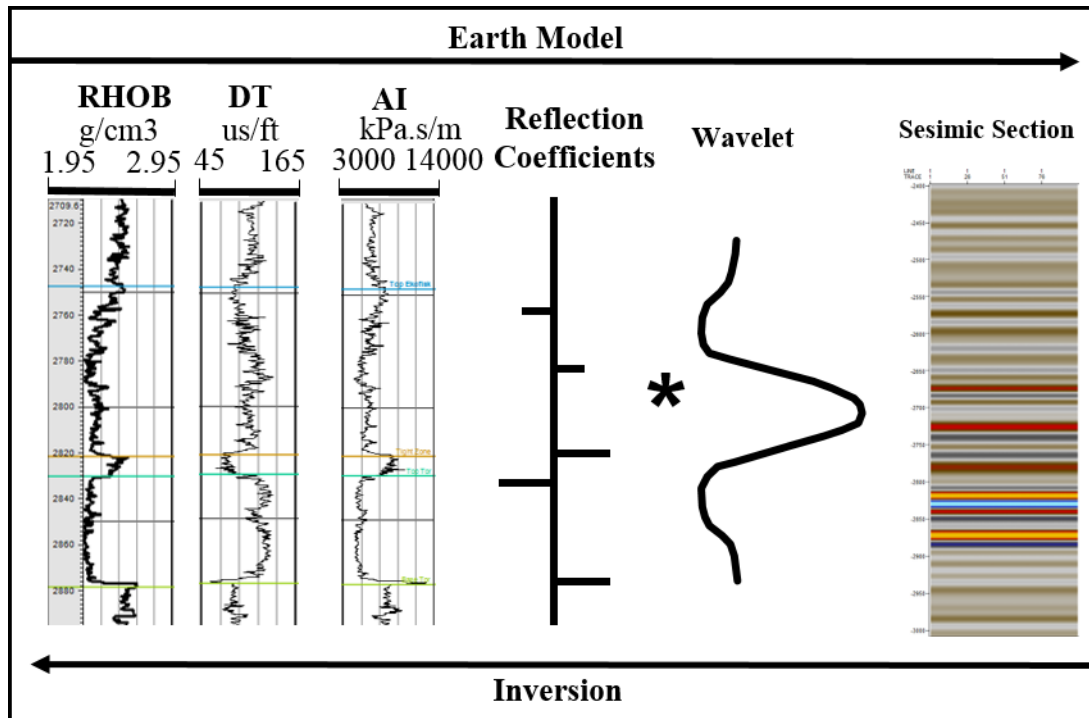


Figure 21 Model data illustrating inversion process.

Due to the band-limited nature of the seismic, inversion of seismic reflectivity data to absolute elastic properties requires the addition of low-frequency information, also known as Low-Frequency Model (LFM) (Figure 22). The figure shows that the frequency range of seismic is limited, and that the LFM introduced to the inversion provides information about the slowly varying vertical trends within the reservoir. Therefore, the LFM is responsible for the accuracy of the impedance data. A typical method for building the low-frequency component is the simple interpolation and extrapolation of well log data within a structural and stratigraphic framework (surfaces) (Sams and Saussus, 2013). An example of LFM and deterministic inversion obtained using LFM is displayed in Figure 23. Note the three wells used for building a Low-Frequency Model in Figure 23-A.

Deterministic inversion delivers a unique solution derived from the seismic data and a predefined low-frequency impedance model. There are a number of approaches to

deterministic seismic inversion and only the one used in this thesis (i.e. Model-based inversion) is outlined below. However, it is important to note that emphasis should be given on careful evaluation of each step along the way rather than the choice of algorithm (Simm and Bacon, 2014).

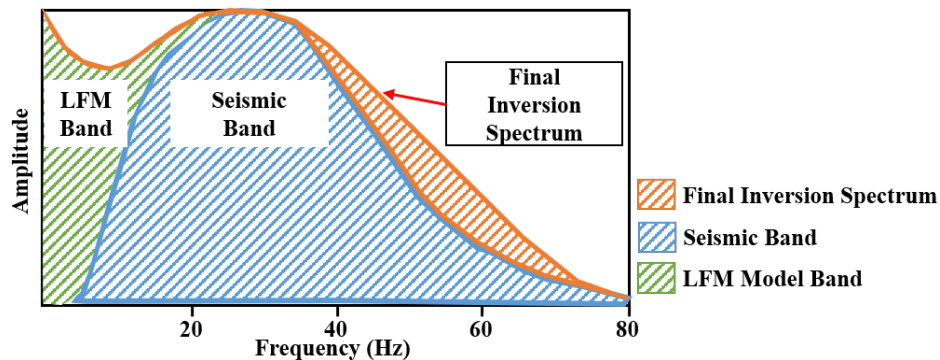


Figure 22 Frequency versus Amplitude plot illustrating the band-limited nature of seismic. Note how the low frequencies fill the band below the seismic and provides a geologic setting. It is possible to gain a few Hz on the high side as illustrated. Modified from Pendrel and Van Riel (2000).

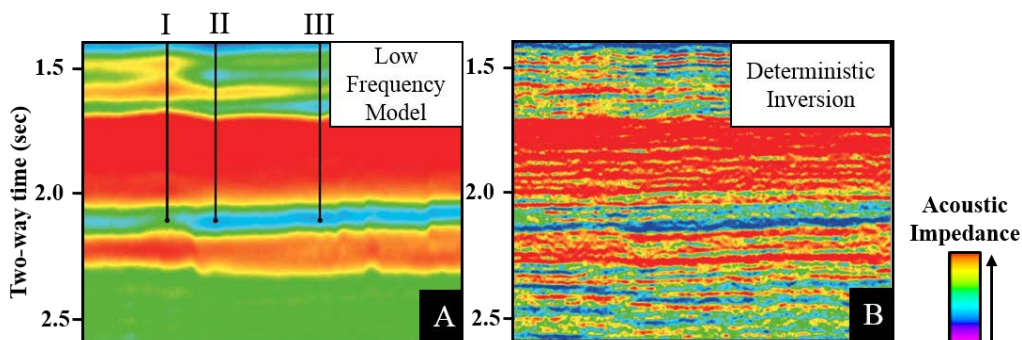


Figure 23 A. The low-frequency model of acoustic impedance used to create the deterministic inversion. The three black lines represent three wells used for building the low-frequency model. Note the variation at the bottom of the well I. B. The results of the deterministic inversion (acoustic impedance) obtained using the low-frequency model. Modified from Francis (2014).

The workflow of the model-based deterministic inversion is illustrated in Figure 24. The model-based inversion uses an iterative forward modelling and comparison procedure. In this method, a wavelet extracted from the original seismic data, the interpreted reservoir surfaces, well log data and the original seismic data is used as input driver. The interpreted reservoir surfaces and well log data are used for building the LFM. The LFM and extracted wavelet are then used for building synthetic seismic at trace level. The synthetic trace is then compared with the original seismic trace. If the error is small, the process moves on to the next trace. If the error is significant, the acoustic impedance of the same trace is modified. The reflectivity is calculated and convolved with the wavelet and the resulting synthetic trace is again compared with the

original seismic trace (Figure 24). An example of original seismic used for inversion, synthetic seismic obtained from inversion, and the difference between the original and the synthetic seismic is displayed in Figure 25. The results of this comparison are then used to iteratively update the model in such a way as to better match the seismic data (Figure 24).

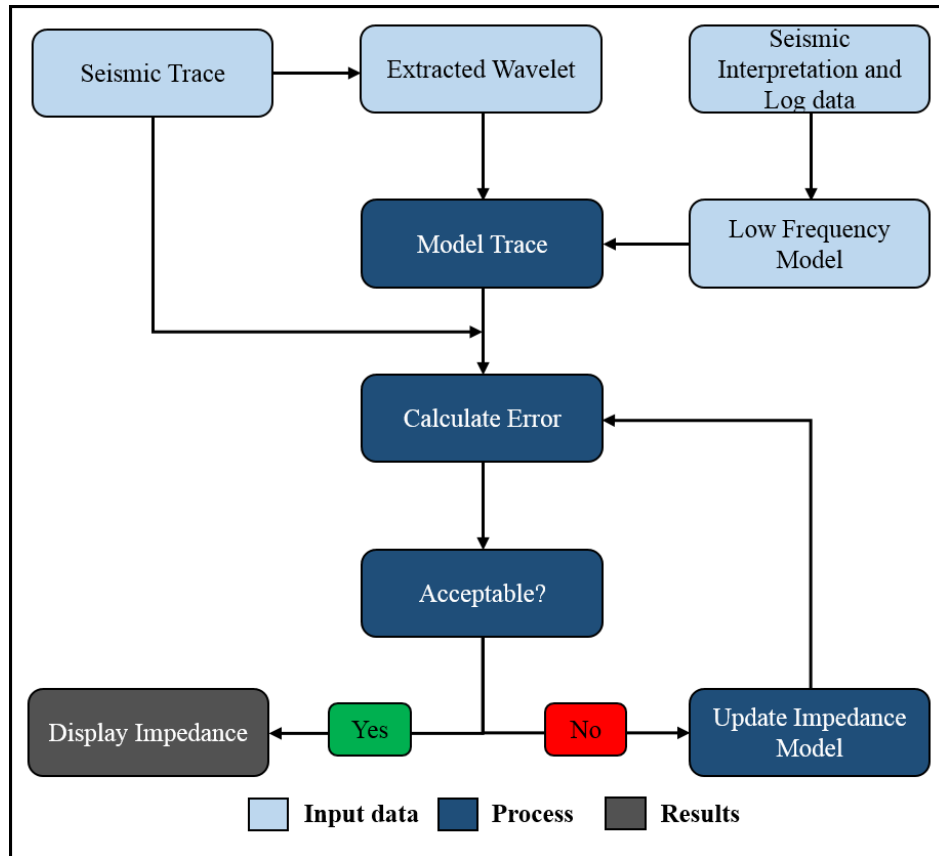


Figure 24 Generalized flow chart for model-based inversion. Light blue text boxes represent the input drivers. Modified from Simm and Bacon (2014).

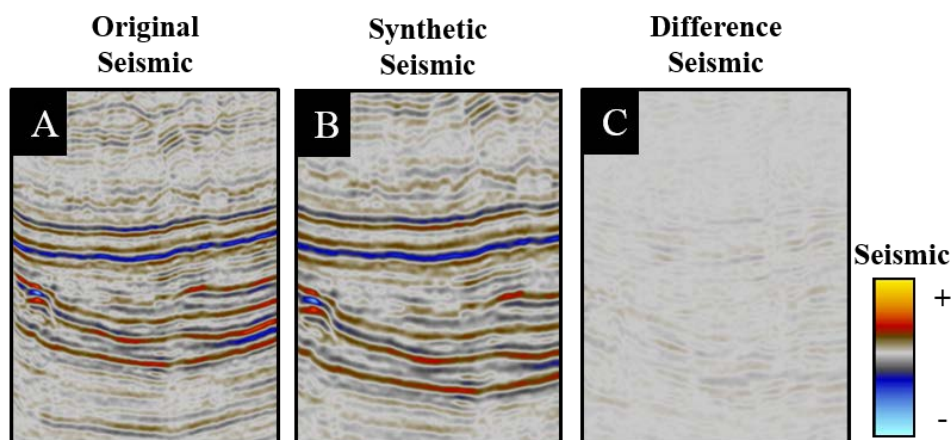


Figure 25 A. Original seismic used for inversion. B. Synthetic seismic obtained from inversion. C. Difference between original and synthetic seismic.

4.4.1. Zoeppritz Equations

Pre-stack (or AVO) seismic inversion is based on the Zoeppritz equation, which is necessary for deriving the wavelets from the angle stacks and the elastic reflectivity from the estimated P- and S-impedance and the density. Therefore, before giving an outline of the AVO inversion, a brief introduction to the Zoeppritz equation and its approximations is given.

The Zoeppritz equations describe the propagation of an acoustic wave across an interface between two viscous media of different acoustic impedances concerning the increasing offset angle (Ganssle, 2012). Figure 26-A represents an interface between two viscous media of different acoustic impedances. The quantities describing the media are as follows: α is the p-wave velocity, β is the s-wave velocity, and ρ is the density, θ_1 is the incidence angle, θ_2 is the transmitted p wave angle, ϕ_1 is the reflected s wave angle, and ϕ_2 is the transmitted s wave angle.

Most AVO inversion algorithms used in commercial software are based on linear or non-linear approximations of the Zoeppritz-equation, such as the Aki-Richards approximation (Aki and Richards, 1980) or the Fatti equation (Fatti et al., 1994). The advantage of these approximations lies in their simple numerical implementation and CPU efficiency. However, the drawback is a lack of accuracy for high-angle reflections. This is illustrated in Figure 26-B for the AVO responses of different approximations to a hydrocarbon benchmark. The variation in AVO responses of different approximations increases as the incident angle increases.

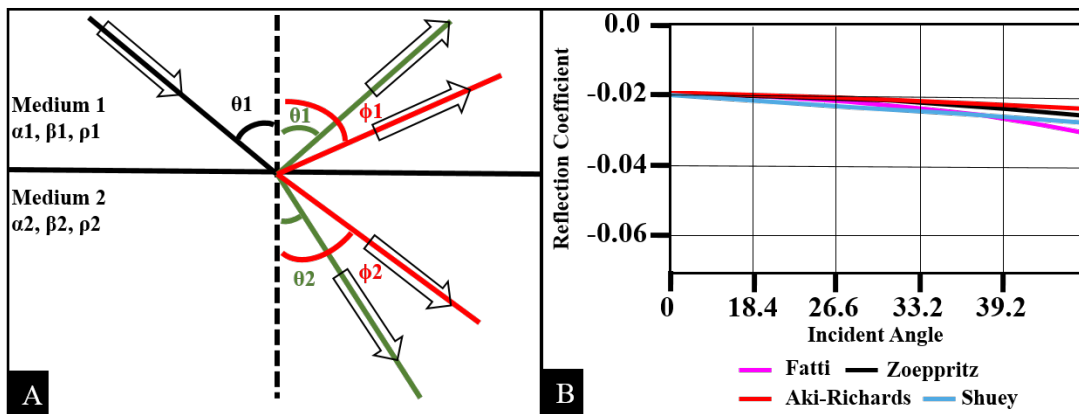


Figure 26 A. Graphical representation of an acoustic wave striking a boundary between two media with different acoustic impedances. B. P-wave reflectivity as defined by different approximations to a hydrocarbon benchmark of shale overlying gas sand. Modified from Booth et al. (2015).

The Aki-Richards approximation is used in the AVO inversion methodology of this thesis to separate the rock properties into p-wave, s-wave, and density components, as described in Equation (6).

$$R_{pp}(\theta) = \frac{1}{2} (1 - 4\beta^2 p^2) \cdot \frac{\Delta\rho}{\rho} + \frac{1}{2 \cdot \cos^2\theta} \cdot \frac{\Delta\alpha}{\alpha} - 4\beta^2 p^2 \cdot \Delta\beta/\beta \quad (6)$$

where:

$\Delta\alpha, \Delta\beta$ and $\Delta\rho$ are the contrasts between the two layers

α, β and ρ are the average P-wave velocity, S-wave velocity, and density, respectively.

ray parameter (p), $p^2 = \sin^2\theta / \alpha^2$

The angle information is contained in θ and in the ray parameter p.

4.4.2. Pre-Stack Simultaneous Inversion

Figure 27 shows the schematic workflow of the model-based pre-stack simultaneous inversion. The pre-stack or AVO simultaneous inversion is based on an estimation of the low-frequency model for acoustic impedance, shear impedance, and density from well log data. Prior to the inversion, the wavelets are derived from the angle-stacks using the Zoeppritz equation or one of its approximations. The simultaneous inversion approach perturbs the P-impedance, S-impedance and density models and calculates the reflectivity from a Zoeppritz approximation for the angles of incidence given by the available angle stacks. The reflectivity traces of the different angles of incidence are convolved with the wavelets of the available angle stacks and the resulting synthetic traces compared with the seismic stacks (Ma, 2002). The AVO inversion used in this study is based on the Aki and Richards approximation described in the previous paragraph.

4.4.3. Deriving Young Modulus from AVO Inversion

Once P-Impedance, S-Impedance, and Density are obtained from the AVO Inversion, P-wave and S-wave velocity can be obtained using the defined relationships. These properties can then be used to calculate the Young Modulus using Equations (7) and (8):

$$Poisson\ Ratio\ (PR) = \frac{\left[\left(\frac{V_p}{V_s}\right)^2 - 2\right]}{\left[2\left(\frac{V_p}{V_s}\right)^2 - 2\right]} \quad (7)$$

$$Young's\ Modulus\ (YM) = [2 * I_s^2 * \frac{(1 + PR)}{RHOB}] \quad (8)$$

where:

I_s = S-Impedance from simultaneous inversion

PR = Poisson Ratio calculated based on Equation (7)

$RHOB$ = Density from simultaneous inversion

V_p = P-wave velocity calculated from P-Impedance and Density obtained from simultaneous inversion

V_s = S-wave velocity calculated from P-Impedance and Density obtained from simultaneous inversion

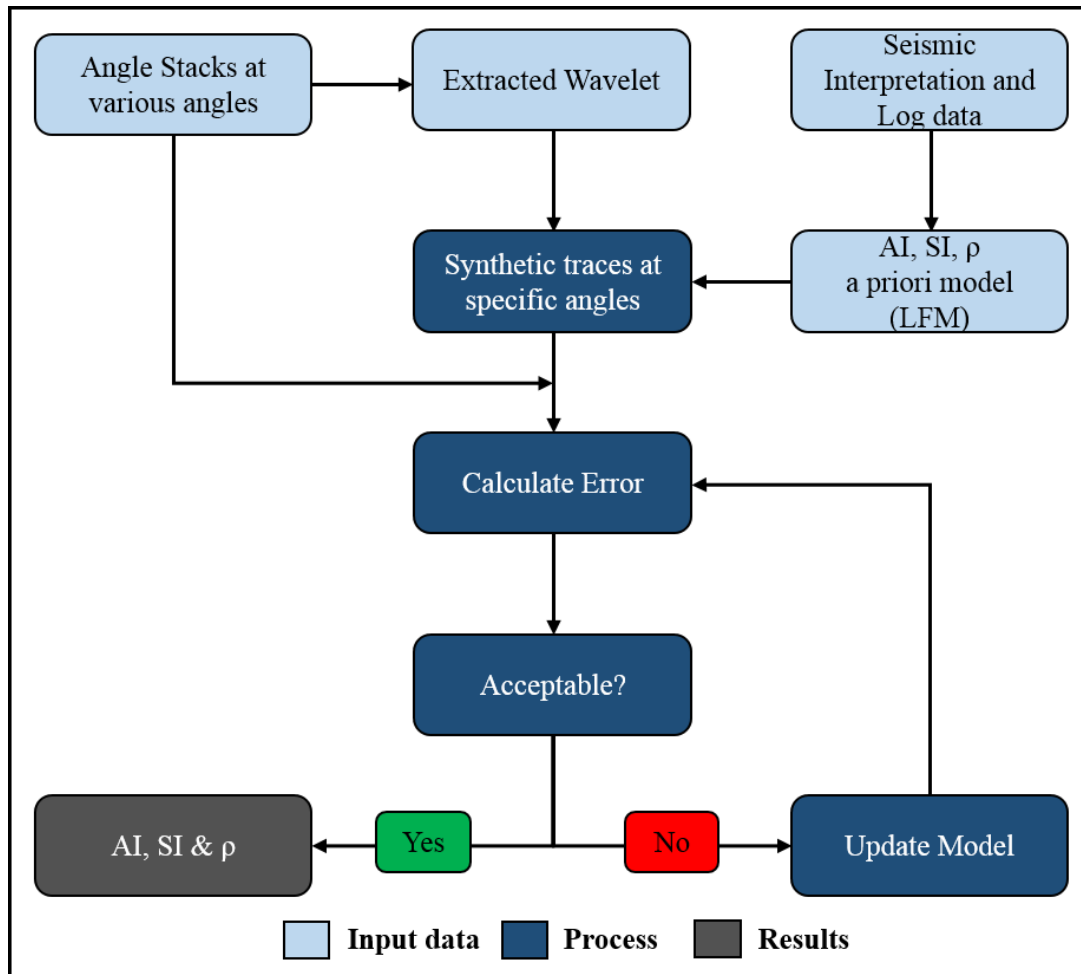


Figure 27 Schematic workflow of model-based pre-stack simultaneous inversion. Light blue text boxes represent the input data for the inversion. Modified from Simm and Bacon (2014).

4.5. Discrete Fracture Network Modelling

The main idea of this thesis is to build a fracture model while using interpreted data from seismic interpretation (i.e. seismic attributes, interpreted faults and fractures) and well log data as fracture drivers (Angerer et al., 2004). The ultimate goal is to populate the 3D grid model with porosity and permeability derived from the modelled fractures. To achieve this goal, a Discrete Fracture Network Model based on fracture intensity is built (Tavakkoli et al., 2009).

The Discrete Fracture Network (DFN) Modelling approach can be defined as the analysis and modelling that explicitly incorporates the geometry and properties of discrete fractures controlling flow and transport (Dershowitz et al., 2004). It refers to a computational approach that explicitly represents the different geometrical properties of individual fractures (i.e. orientation, size, concentration, shape, length, and aperture). A DFN Model can be generated from geological mapping, stochastic realisations of fracture intensity or geomechanical simulation of the stress field to represent different types of rock fractures including joints, faults, veins, and bedding planes (Lei et al., 2017). A robust method for the development of a fractured reservoir model is to quantitatively integrate the seismic parameters with available fracture information (Araujo et al., 2004). In this method, fracture intensity is a critical parameter, derived from the wells and, interpolated between the wells using as guides for the seismic attributes and the estimated Young Modulus.

Not all fractures from the DFN model can be incorporated into the field-scale models because there may be billions of them in each cubic kilometre of reservoir rock (Correia et al., 2011). Therefore, upscaling is used for field scale simulation. Upscaling is an averaging process in which the characteristics of a fine-scale model are assigned to coarse scale cells. This is performed for all the cells in the coarse grid (King et al., 1998). The well log data, the seismic data, and all the properties required for reservoir flow simulation are also upscaled into a 3D grid. A 3D grid is a network of horizontal and vertical lines that divide a model into boxes (Al-Baldawi, 2015). Each box is called a grid cell and will have a single cell property (i.e., rock type, porosity, saturation).

4.5.1. Estimating Fracture Parameters

The fracture parameters used as input for fracture modelling are described below.

4.5.1.1. Fracture Intensity Distribution

The number of dimensions plays an important role in determining fracture intensity. The fracture intensity measured in 1D represents the number of fractures per unit length and is called P_{10} (Dershowitz and Herda, 1992) (Figure 28-A). This value is inversely proportional to the fracture spacing. In general, the intensity defined in 1D is dependent on the orientation and shape of the fractures. However, this intensity is not adequate for 3D fracture modelling. In 3D modelling, fracture intensity is defined in a 3D region, which is independent of the orientation and shape of the fractures (Dershowitz and Herda, 1992). The intensity P_{32} represents the fracture area within a reference volume (Figure 28-B). Since the direct measurement of the intensity based on P_{32} is practically impossible. Dershowitz and Herda (1992) derived a relation between the intensity values P_{32} and P_{10} given by equation (9):

$$P_{32} = C_{10} * P_{10} \quad (9)$$

where:

C_{10} is a constant dependent upon the orientation of the fractures.

It is worthwhile mentioning that P_{32} is equal to P_{10} if the fractures cut the borehole completely.

Generation of fracture intensity by using interpolation algorithm

The estimated fracture intensity in the wells needs to be modelled outside the wells. Kriging is one of the most common algorithm used for this interpolation. The kriging algorithm delivers an optimal interpolation and generates a best linear unbiased estimate at any location (Bohling, 2005). This algorithm is based on the variogram model derived from the input data. It also honours the mean and variance of the input data. The variogram model refers to the spatial variation of the input data (Ringrose and Bentley, 2015). In general, the variogram delivers the mean variance of data pairs of similar distance. The semi-variance represents the mean variance of data pairs as a function of the separation distance. The approximation of the semi-variance by an analytical function delivers the variogram model. This model delivers the variogram parameters like sill, nugget and anisotropy range (Figure 29). The black circles in Figure 29 represent the data points, and the blue line represents the modelled variogram. The modelled variogram along with other parameters (i.e., sill, nugget and anisotropy angle) are then used in kriging. The variogram range is one of the most important parameter, which describes the distance at which the variogram model flattens out. This means that distances closer than the range are spatially autocorrelated, whereas distances farther apart are not. The value attained by the semi-variogram model at the range (i.e. the value on the y-axis) is called the sill. The nugget effect is related to the measurement error or spatial sources of variation at distances smaller than the sampling interval or both. In Figure 29 it can be defined as the value at which the variogram model intercepts the y-axis.

Secondary input drivers (i.e., Young Modulus and seismic attributes) as a guide model are another way of modelling fracture intensity. Co-kriging is a natural extension of the kriging algorithm used to estimate or predict a primary variable with the help of a secondary variable (co-variable) (Azevedo and Soares, 2017). The primary variable should be highly correlated (positive or negative) with the secondary variable. The co-kriging method is appropriate when the primary variable is poorly sampled but is related to the well-sampled secondary variable. Collocated co-kriging is a type of co-kriging that can be applied when the primary variable is present in sparsely distributed points while the secondary variable is located in all points of the grid being estimated (Rocha et al., 2012). In this way, the secondary variable is controlled via its correlation factor with the primary variable.

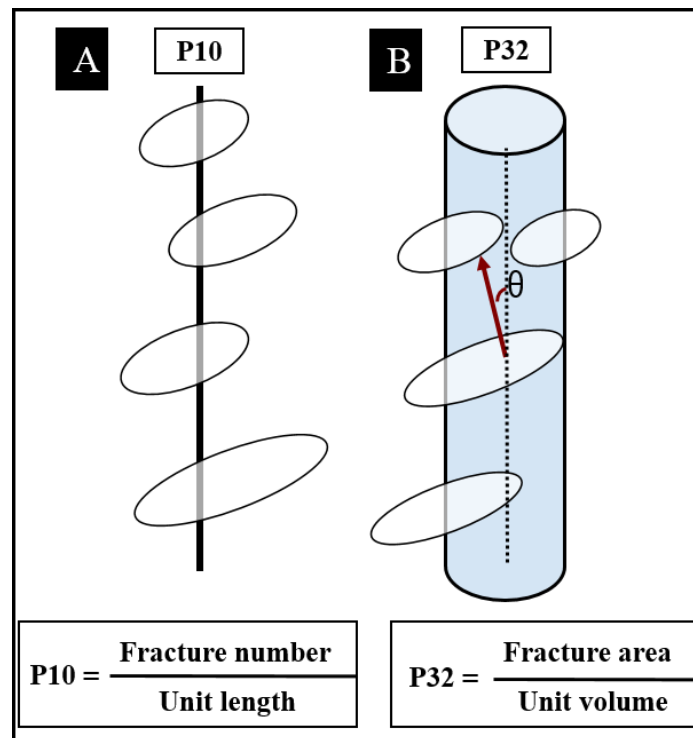


Figure 28 A. Sketch illustrating the fracture intensity represented in 1D (P_{10}). B. Sketch illustrating the fracture intensity represented in 3D (P_{32}). Circles represent fracture surfaces. Modified from Dershowitz and Herda (1992).

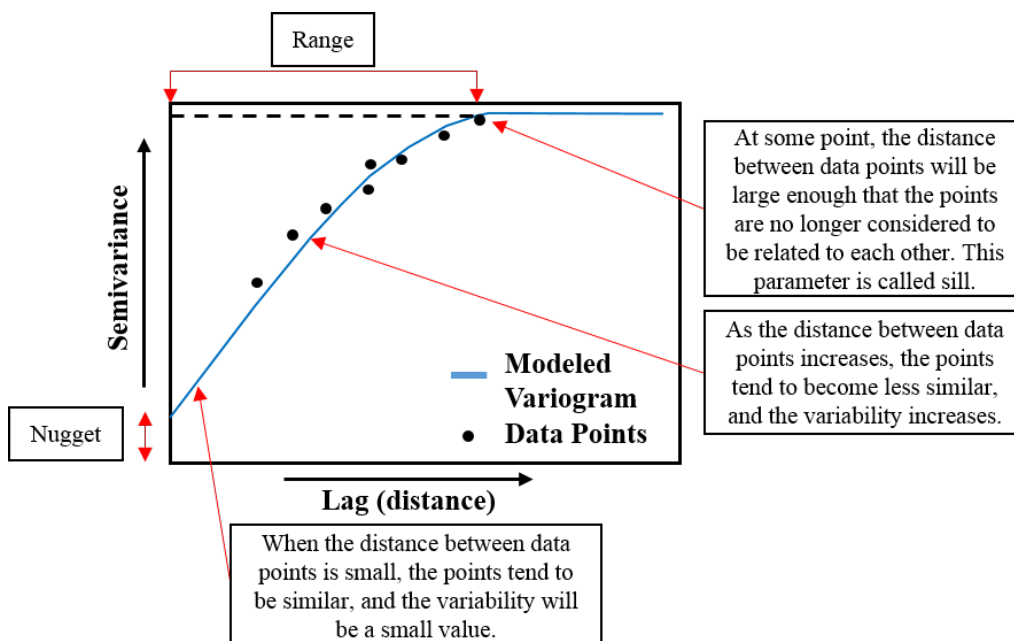


Figure 29 Typical semi-variogram and its components. The black circles represent the data points, and the blue line represents the modelled variogram. The technique of variogram quantifies the spatial variability of a regionalised variable and provides the input parameters for the spatial interpolation of kriging. Modified from Baba et al. (2014).

4.5.1.2. Statistical Laws used for Fracture Length and Fracture Aperture

Statistical laws describe the relationship between fracture length and fracture aperture with fracture intensity. Fracture length is a measure of the extent of the discontinuity surface (Singhal and Gupta, 2010). The statistical laws are used to assign the fracture parameters to the fracture model. The Discrete Fracture Model uses many statistical tools to model fracture length and aperture. In general, the distributions used in fracture modelling are normal, log, exponential and power law. Table 3 illustrates statistical laws along with their controlling parameters. Changing the values of these parameters affects the distribution of the measured fracture properties.

Table 3 Statistical laws used in fracture modelling

Statistical Law	Equation	Controlling parameters
Normal	$p(x) = \frac{1}{\sigma\sqrt{2\pi}} e^{- (x-\mu)/2\sigma^2}$	μ - mean σ - standard deviation
Log-normal	$p(x) = \frac{1}{x\sqrt{2\pi\sigma^2}} e^{- (\ln x-\mu)^2/\sqrt{2\sigma^2}}$	μ - log mean σ - standard deviation
Exponential	$p(x) = \frac{1}{\beta} e^{-x/\beta}$	β - scale parameter
Power law	$p(x) = \frac{\alpha - 1}{X_{min}} \left(\frac{X}{X_{min}} \right)^{-\alpha}$	α - exponent X_{min} = distribution lower bound

4.5.1.3. Fracture Orientation and Concentration Estimation

Fractures log data provide information about the fracture orientation and concentration. Concentration is the spread of the dip azimuth data for a fracture set. The low value (i.e. 0) of concentration gives a wide scatter of the dip azimuth over the complete azimuth range (0-360°), and high value gives a focused distribution. These parameters (i.e. orientation and concentration) are integrated into the DFN model with the help of three different algorithms, namely Fisher, Bingham and Kent. These algorithms allow users to control the orientation and concentration of the fractures. These models are illustrated in Figure 30 with different parameter values in each case. Note that mean dip and mean dip azimuth are kept constant (90° and 70°, respectively) in all cases. The Fisher model requires the mean orientation and concentration parameter as input. This model is similar to the normal distribution. The Kent model is similar to the Fisher model except that the deviation around the preferred direction is anisotropic, resulting in a more elongated distribution of fracture orientations. The Bingham model incorporates two concentration parameters, i.e. azimuthal concentration and radial concentration. The azimuthal concentration controls the variation around the mean azimuth, and the radial concentration controls the variation around the mean dip.

4.5.1.4. Oda Permeability Upscaling Method

The Oda method is one of the most widely used methods in Discrete Fracture Network upscaling to compute fracture permeability (Ahmed Elfeel, 2014). The Oda method is an analytical method that assumes all the fractures within the grid cell contribute to the fracture permeability, and the fracture network has full connectivity (Ahmed Elfeel, 2014). The advantage of using this method is that it enables to compute the fracture permeability quickly (Decroux and Gosselin, 2013).

4.6. Previous Work

Mackertich and Goulding (1999) performed a structural study of the South Arne field and identified the dominant WNW-ESE and NNW-SSE trending faults from the seismic data. Mackertich and Goulding (1999) also observed the subtle lineaments striking in the N-S direction.

Astratti et al. (2015) identified and described several fault sets of the South Arne Chalk group using the seismic edge attribute. This study also revealed a new ENE-WSW seismic trend, within the chalk. However, its presence and extend were not completely confirmed.

A study on the elastic behaviour of chalk from the Ekofisk and the Tor formations in the Danish sector of the North Sea, established different porosity-dependent elastic models for cemented and uncemented chalk due to different degrees of cementation (Gommesen et al., 2007).

Herwanger et al. (2013) did a study on stress changes in the field due to reservoir production and concluded that the rotation in the azimuth of the hydraulic fractures was due to the re-orientation of the principal stress directions.

Christensen et al. (2006) presented an integrated workflow using geophysical, geological, and engineering data for fracture modelling using the Continuous Fracture Modelling (CFM) approach. The modelled porosity, obtained from impedance inversion extracted from the seismic cube and the porosity logs from wells, along with fracture density derived from the FMI logs were used with geomechanical drivers to create a fracture density model. The Discrete Fracture Model (DFN) constructed by Luthje et al. (2013) used seismic attributes as a parameter for guiding the fracture density measured at the wells. The upscaled permeability, calculated using the DFN model, was then calibrated with the help of dynamic (production) data. It is important to note that the studies above do not discuss in detail the relationship between measured fractures and the elastic parameters (i.e. Young Modulus) obtained from seismic data.

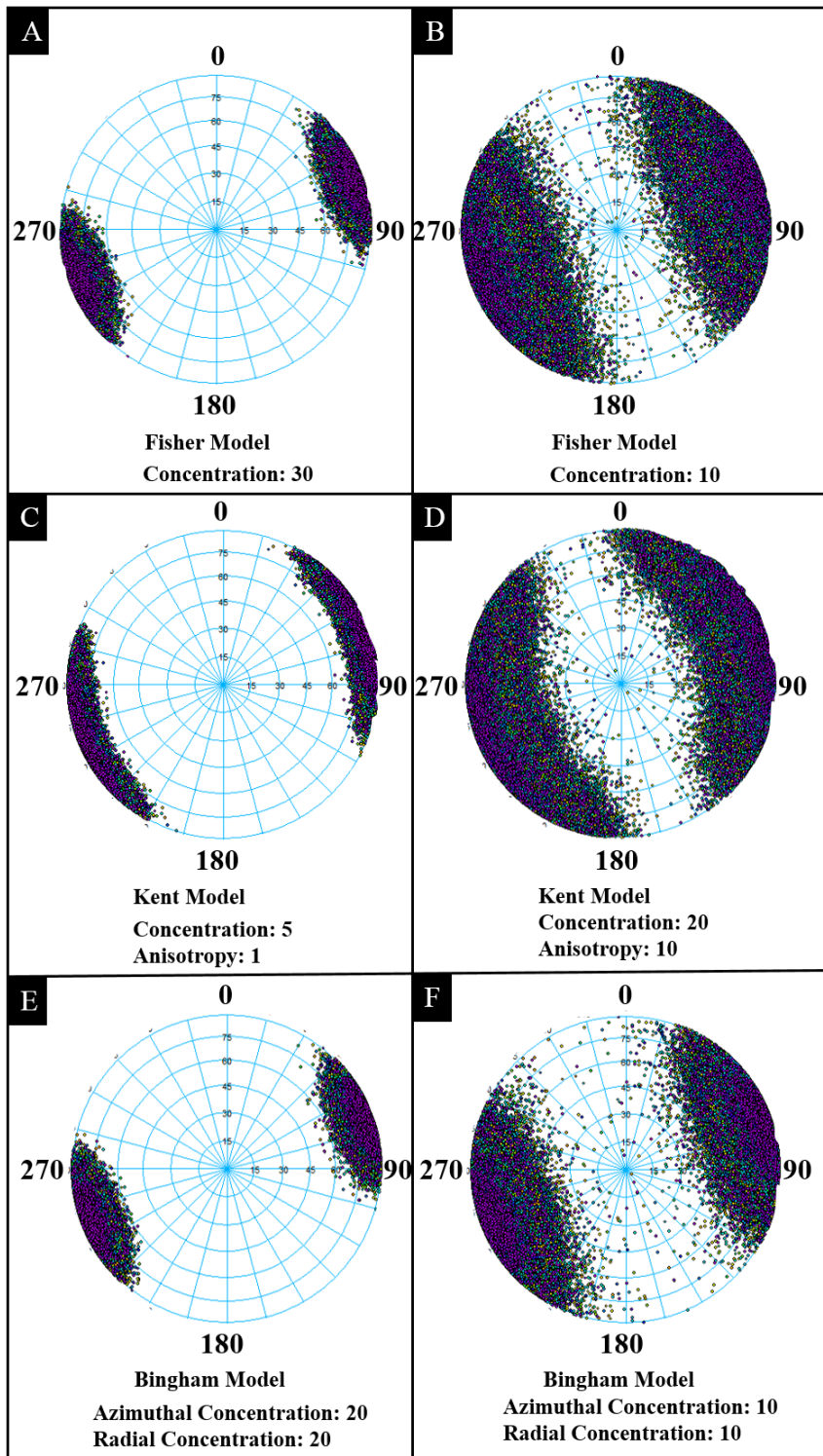


Figure 30 A and B. Distribution of fracture orientation on stereo-net based on Fisher Model with different concentration parameters. C and D. Distribution of fracture orientation on stereo-net based on Kent Model with different concentration and anisotropy parameters. E and F. Distribution of fracture orientation on stereo-net based on Bingham Model with different azimuthal and radial concentration parameters. Note that mean dip and mean dip azimuth are the same, 90° and 70° respectively, in all the cases.

5. METHODOLOGY

5.1. Introduction

The generalised workflow involving well data, seismic data, and fracture modelling is illustrated in Figure 31. This figure mentions the steps that are discussed in detail at the corresponding sub-chapter in the text boxes. Petrel Software Platform is used for this study.

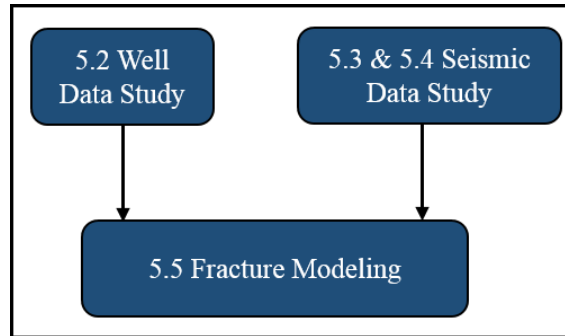


Figure 31 Generalized workflow used in this thesis involving the well data, seismic data and fracture modelling. Numbers in the textboxes represent the sub-chapter where the particular study is discussed.

5.2. Well Data Study

Figure 32 illustrates the well data workflow used in this thesis. The light blue box represents the input data, i.e., well log data in this case. The light grey box represents the interpreted fracture point data received from Hess Corporation in the form of fracture dip angle, dip azimuth and fracture classification. The dark blue boxes indicate the processes used during this study. The dark grey boxes show the results.

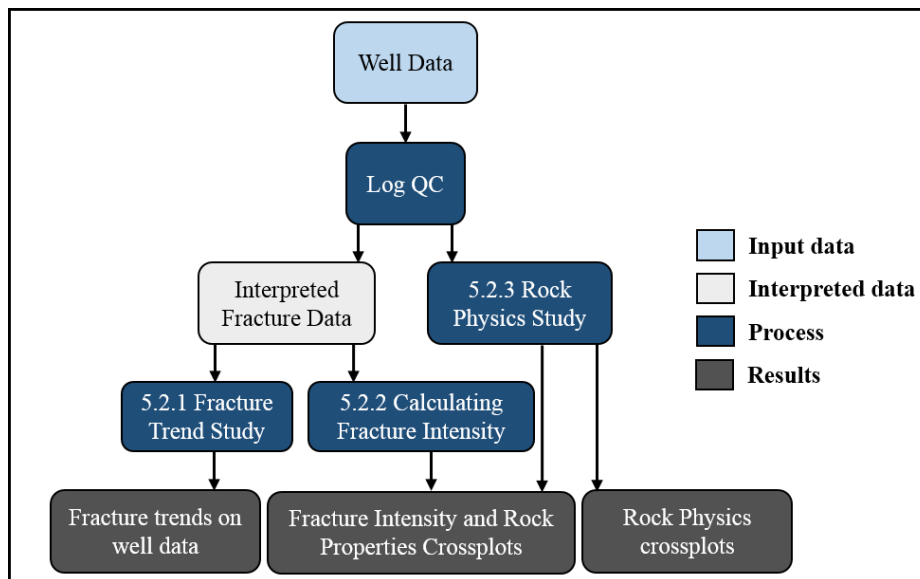


Figure 32 Workflow for well data study Numbers in the textboxes represent the sub-chapter where the particular study is discussed.

5.2.1. Fracture Trend Study

For fractures to be incorporated into a fracture model, it is important to identify the orientation of fractures on a well-by-well basis (Figure 30) (Section 4.5.1.3). The fracture data obtained from image logs and interpreted by Hess Corporation was classified into conductive fractures, resistive fractures, and veins. In the dataset, resistive fractures and veins were classified as one entity. The dataset also contains dip angle and dip azimuth for each interpreted fracture. For this study, the emphasis was given to conductive and resistive fractures.

Following the idea of Mackertich and Goulding (1999), where a wide distribution of azimuth is observed in the well fracture data (Figure 9) (Section 2.4.3), a unique methodology was adopted to identify the dominant fracture trends in each well. In this process, a histogram of dip azimuth (dip direction) was plotted which separates the trend from the noise as the trend is characterized by the local maxima (Figure 33). An important property of histograms is the bin width. The bin width defines the resolution of the histogram. The selection of the bin width is crucial for an appropriate representation of the data in a histogram (Birgé and Rozenholc, 2006). This is because the selection of a low or high bin width value does not portray the histogram data very well. Hence, in this study, an optimal bin width (i.e., 10° in this case) that clearly illustrates the local peaks with respect to the nearest minimum was selected.

Figures 33 and 34 illustrate the well azimuth data of well SA-1A in a histogram and a stereo-net respectively. In Figure 33 the histogram displays the different peaks of dip azimuth. The different peaks could then be linked to the different structural trends recognized in previous articles (Astratti et al., 2015; Mackertich and Goulding, 1999). On the other hand, the stereo-net plot (Figure 34) displays the large scattering of the azimuth data, where only the general direction of the fracture data could be established.

The coloured rectangles in Figure 33 correspond to the interpreted fracture trends. The NNW-SSE and the WNW-ESE fracture trends are displayed in blue and brown coloured rectangle respectively. These interpreted fracture trends are then displayed in the stereo-net plot in Figure 34. Coloured shaded regions in Figure 34 represent the corresponding trend identified from Figure 33. The coloured arrows in Figure 34 represent the strike direction of the corresponding fracture trend. The strike direction was derived based on the mean azimuth of the fracture trend. This histogram-based methodology displays the different fracture trends better than the standard stereo-net plot and helps in the analyses of the fractures. It was adopted for all the other wells.

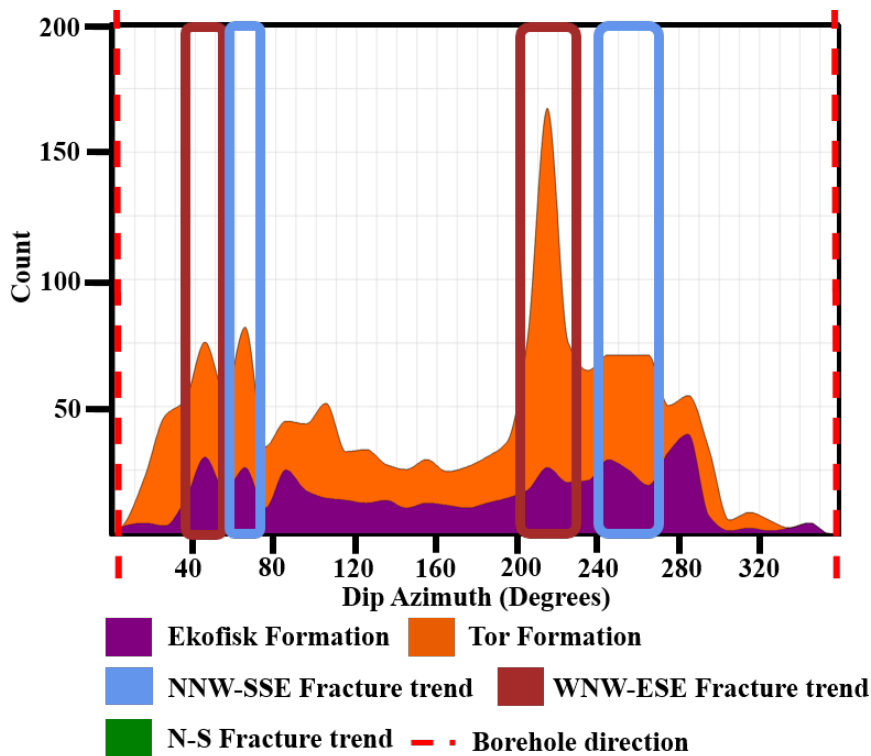


Figure 33 Histogram of dip azimuth (dip direction) of well SA-1A. The x-axis represents the dip azimuth (dip direction), and the y-axis represents the number of times a particular value is encountered in the dataset of well SA-1A, i.e., count or frequency. The coloured rectangle represents the fracture trends identified in the data. Red dashed line represents the borehole direction of the well.

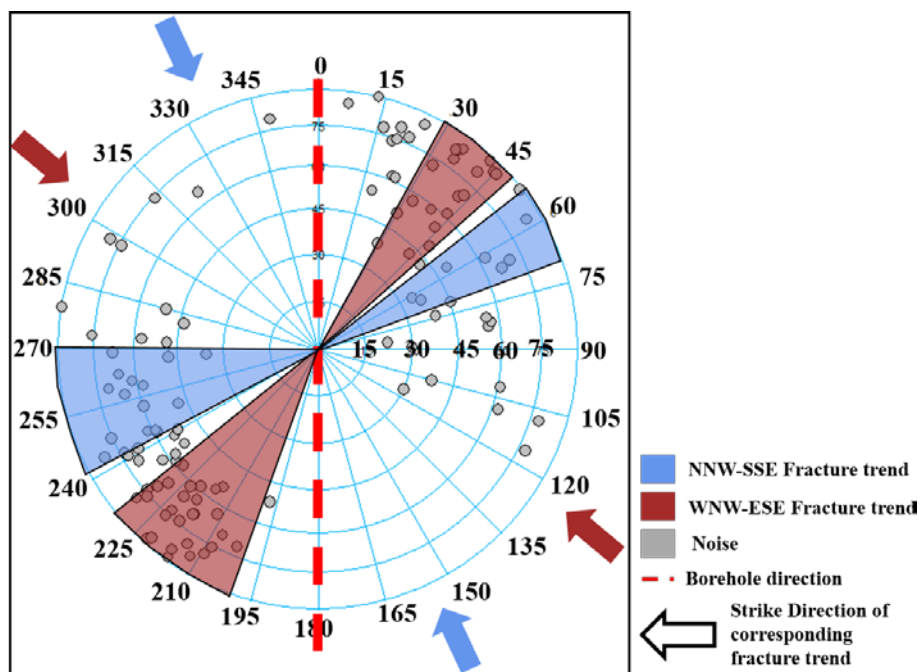


Figure 34 Stereo-net plot of well SA-1A displaying the fracture azimuths. Coloured area represents the interpreted fracture trends derived from the histogram methodology, whereas, coloured arrows represent the corresponding mean strike direction.

5.2.2. Calculating Intensity logs

The fracture intensity log is defined as the derivative of the cumulative log of the measured fracture points. The intensity log is calculated over a user-defined, gliding depth window. The window length has an averaging effect on the slope of the cumulative log and therefore acts as a smoothing filter. The fracture intensity calculated using two different values of window lengths is illustrated in Figure 35.

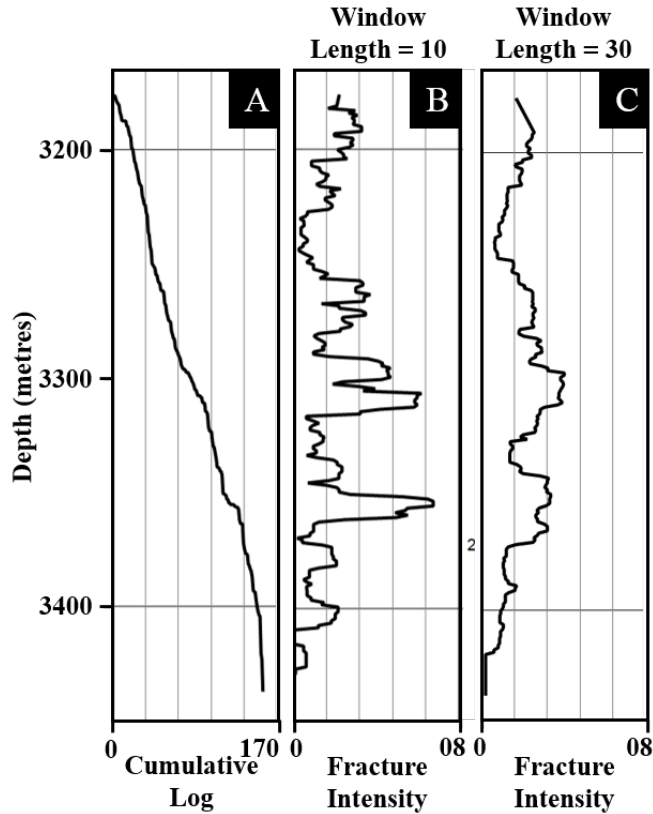


Figure 35 A. Cumulative fracture log of a well, used for calculating the fracture intensity log over a gliding window of user-defined length. B. Fracture intensity calculated using a window length of 10m. C. Fracture intensity calculated using a window length of 30m.

Borehole Correction

The borehole orientation plays a vital role in estimating the fracture intensity. The angle between the borehole and fractures needs to be considered, before the intensity estimation. The borehole correction concept was developed by Terzaghi (1965). It describes the decreasing intensity of the fractures as their strike approaches that of the borehole (Figure 36). Figure 36 shows that case A has the higher probability of sampling the fractures as compared to case B. Hence, case A will result in higher intensity value. The following equation describes the relation between fracture spacing S , fracture frequency F , and the angle α between the borehole and the fracture plane:

$$F = \frac{\cos \alpha}{S} \quad (10)$$

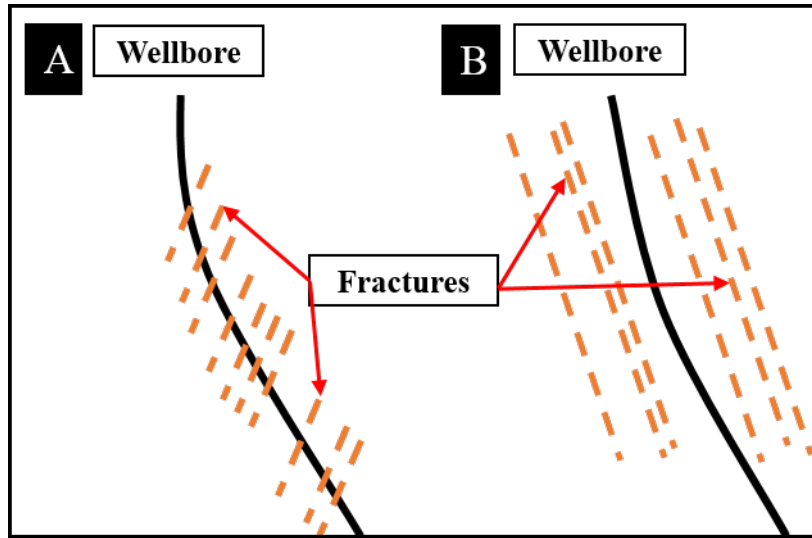


Figure 36 A. Sketch illustrating fractures perpendicular to the borehole. B. Sketch illustrating fractures parallel to the borehole. Note the difference in the number of fractures encountered in the borehole in both the cases. Case A results in higher fracture intensity.

The corrected fracture intensity derived from the above equation was used for comparison with the rock moduli (i.e., Young Modulus) and sampled into a 3D grid for fracture modelling (Section 4.5.1.1).

5.2.3. Rock Physics Study

Rock physics represents the link between geophysical and geological observations and is an integral part of reservoir characterisation (Golyan, 2012). Rock physics is crucial for relating seismic data to reservoir properties because it allows setting up the relationship between the elastic properties (velocity, density, impedance) to the reservoir properties (porosity, saturation) (Butt, 2012). Figure 37 illustrates the rock physics workflow used in this thesis. It shows the different input logs and the calculated logs (i.e., P- and S- impedance and Young Modulus) that were cross-plotted to observe the rock properties that allow to better characterise the reservoir. In this study, the emphasis was given to the Tor and Ekofisk formations. The Gamma-Ray log was used to characterise the chalk based on the shaliness of the chalk. This characterisation is important since the clay content of the chalk influences the frequency of fractures (Section 2.4.3). In addition, the rock properties were compared with calculated fracture intensity to understand how the fractures influence the reservoir properties (Section 4.3).

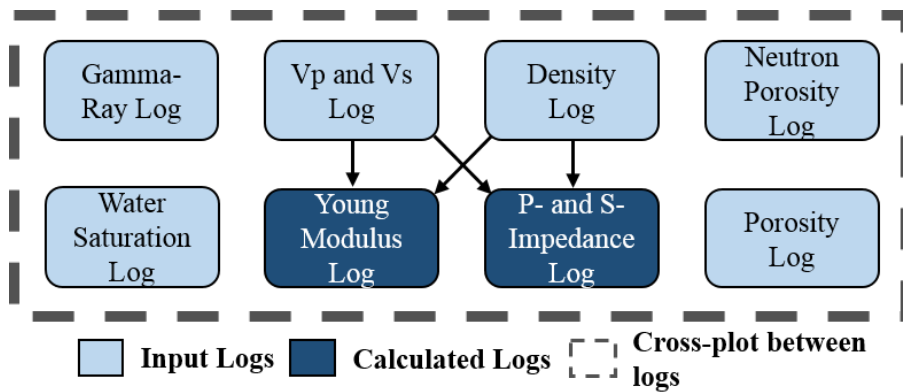


Figure 37 Workflow for rock physics study illustrating the input, and the calculated logs. The grey dashed line around the boxes illustrates the cross-plots between the input and the calculated logs.

5.3. Seismic Study

Figure 38 illustrates the seismic data study performed in this thesis. The workflow consists of several steps. The interpreted seismic horizons along with the seismic data are used for the AVO Inversion (Section 4.4.2) and the structural analysis workflows. The results obtained from these processes (i.e., Young Modulus cube, Ant-tracking cube, Variance cube, and t^* attenuation cube) were used to analyse the different structural trends. These cubes were later resampled into the 3D grid and used as a secondary variable for modelling the fracture intensity (Section 4.5.1.1).

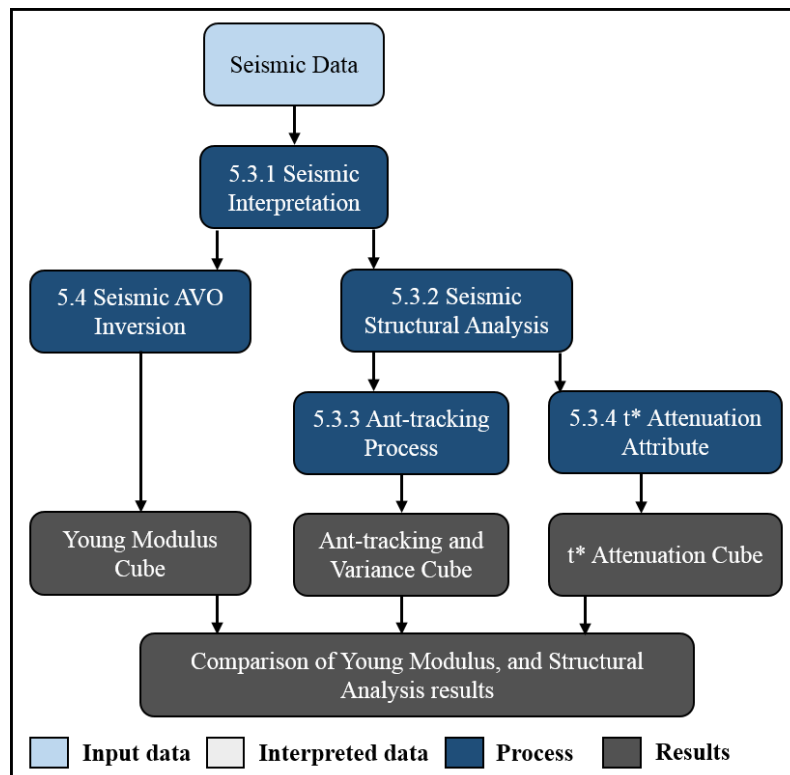


Figure 38 Workflow of seismic data illustrating the process and the results obtained.

5.3.1. Seismic Interpretation

Interpreting seismic data is crucial for the study since the interpreted reservoir top and bottom surfaces are used for the 3D model and for building the low-frequency model (Section 4.4) of the AVO Inversion process.

5.3.2. Structural Analysis Study

As discussed in Section 4.1.1, fractures are associated with faults. It is important to identify the small-scale faults and fractures associated with faults on the seismic scale. However, the detection of small-scale faults and fractures swarms is difficult in seismic due to the band-limited nature of seismic (i.e., fracture swarms and small-scale faults require a very high seismic resolution and very high signal-to-noise ratio (S/N)) (Chopra and Marfurt, 2007). Identifying structural features using different seismic attributes leads to a more reliable interpretation of small-scale faults (Chopra and Marfurt, 2007). Seismic attributes are described as the information obtained from the seismic data, either by direct measurements, logical or experience-based reasoning (Taner, 2001). The attributes and processes used in this study are:

1. Ant-tracking including variance and edge enhancement
2. t^* Attenuation attribute

5.3.3. Ant-tracking Workflow

The Ant-tracking algorithm creates an enhanced fault volume by considering all spatial discontinuities in three dimensions. The ant-tracking uses the principle of swarm intelligence, which describes the collective behaviour of a large group of social insects. For example, ants use swarm intelligence for finding the shortest path between the nest and a food location by communicating via a chemical substance - pheromones (Pedersen et al., 2005). In the case of seismic attribute data, many “artificial ants” track and capture the seismic discontinuities that need to be available as amplitude anomalies. Consequently, the seismic cube needs to be conditioned to represent the faults as large amplitudes. A complete workflow of the fault cube generation using ant-tracking is illustrated in Figure 39. The stereo-nets in this figure are explained below.

Typically, the ant-tracking workflow consists of three steps:

- a. Variance attribute applied to seismic cube
- b. Edge enhancement applied to variance cube
- c. Ant tracking applied to edge enhancement cube

The Variance attribute is a fault enhancing attribute that measures the local variation of the input signal on a trace-to-trace level (Pereira, 2009). Generally, the variance along a continuous reflection is small. Faults and fracture swarms may cause discontinuities which have an impact on the continuity of the seismic horizons; hence they are

detectable in the seismic volume (Abul Khair et al., 2012). Consequently, the variance attribute will show high values across discontinuities such as faults (Randen et al., 2001).

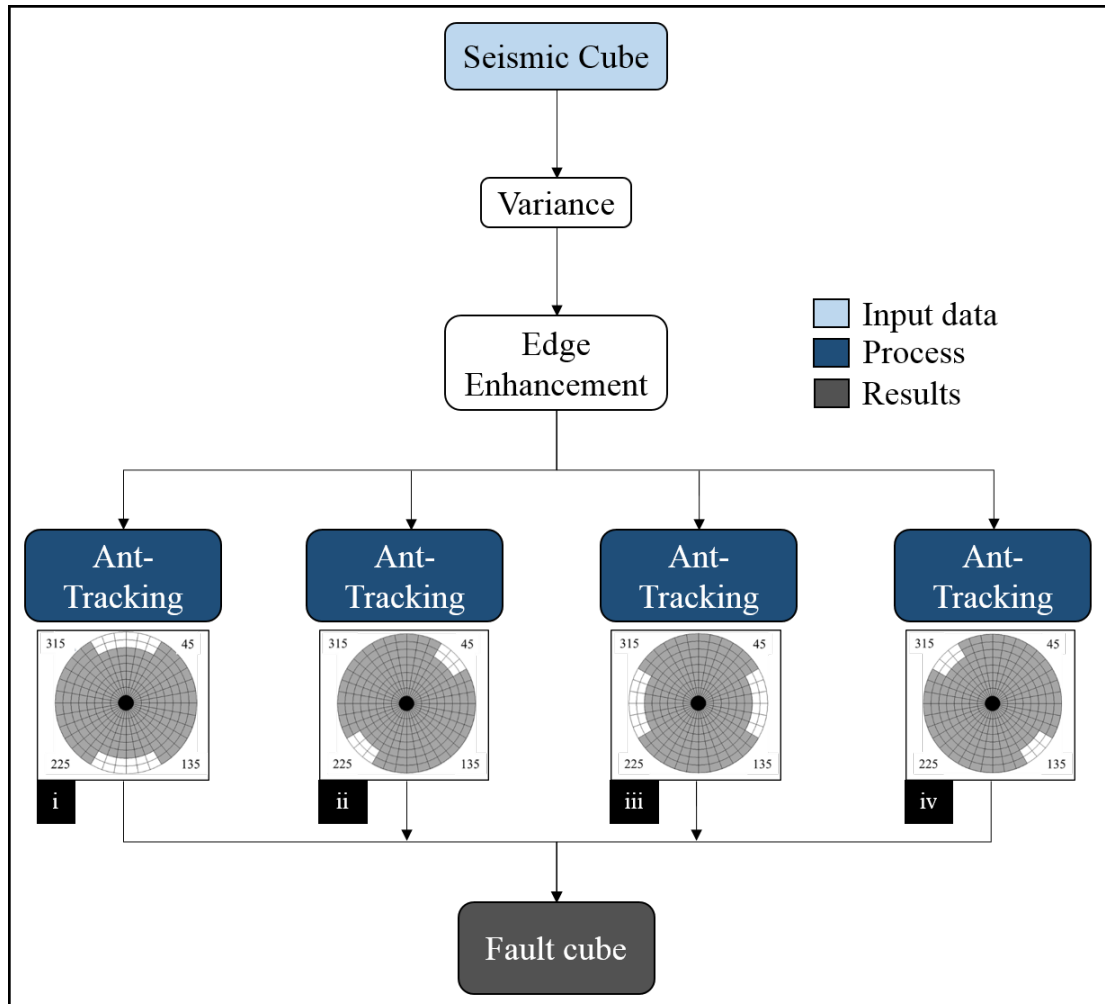


Figure 39 Workflow for generating fault cube using Ant-tracking process. Ant-tracking faults obtained from (i) and (ii) are illustrated in Figure 41 and from (iii) and (iv) in Figure 42.

The second step in the workflow, i.e., edge enhancement, highlights the changes of the signals across neighbouring traces. Typically, faults show a steep dips and consequently, this process enhances them. This means that subtle faults are easily captured, and no artefacts are introduced by smoothing, which makes it the preferred attribute for fault representation (Randen et al., 2001). The third step, i.e., Ant-tracking, generates the ant-track volume. This step improves the fault amplitudes by removing noise that is characterised by lack of continuity of events.

Ant tracking allows the identification of faults/ lineaments within user-defined dip and azimuth ranges that are defined via a stereo-net-tab (Figure 40). In this way, it was

possible to derive Ant-tracking volumes that capture different sets of faults in the seismic data that are distinguished via their mean strike directions. This approach assisted in identifying the different fracture trends already interpreted on the well fracture data (Section 5.2.1). Four different Ant-tracking volumes generated using the stereo-net tab functionality are displayed in Figures 41 and 42. The four Ant-tracking volumes were then stacked to form an aggregated fault cube. This not only led to the retention of stronger lineaments showing a lower dip compared to the faults, but also to the enhancement of subtle faults.

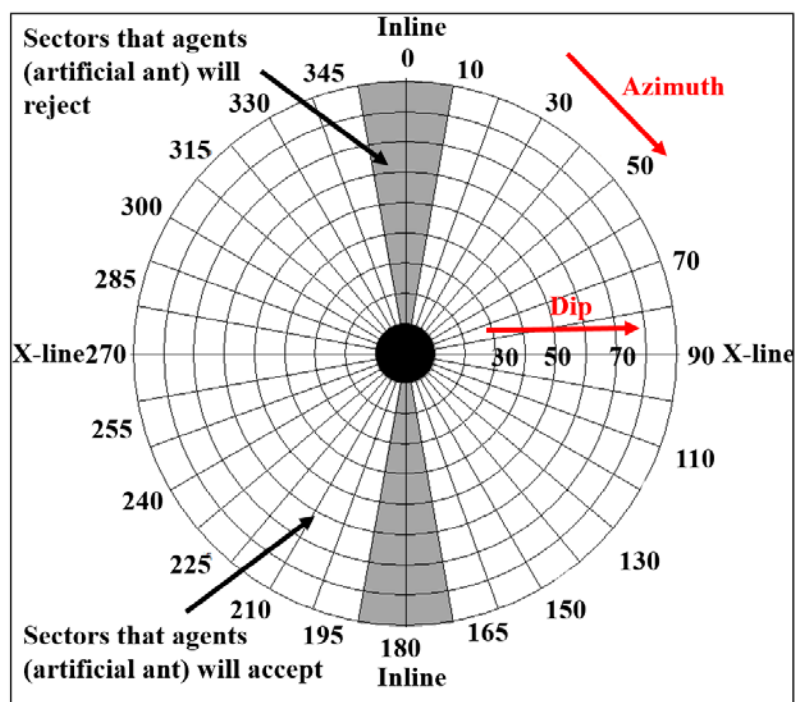


Figure 40 Stereo-net tab used in the Ant-tracking workflow. The white coloured area represents the open area for agents and grey coloured area represents the restricted area for agents. Note that the azimuth is measured with reference to the inline direction and not the true North. Modified from Schlumberger (2010).

5.3.4. t^* Attenuation attribute

Geir U. Haugen (2000) discussed the idea of seismic energy scattering caused by fractures resulting in an attenuation of higher frequencies of the seismic data. Najmuddin (2001) introduced a fracture indicator attribute, based on the above concept of high-frequency attenuation, called t^* attenuation. Larger t^* values indicate greater attenuation of higher frequencies and consequently a shift of the amplitude spectrum towards lower frequencies (Najmuddin, 2001). High t^* values may either indicate a higher fracture intensity, or larger thickness of the fractured layer or a combination of the two (Najmuddin, 2004).

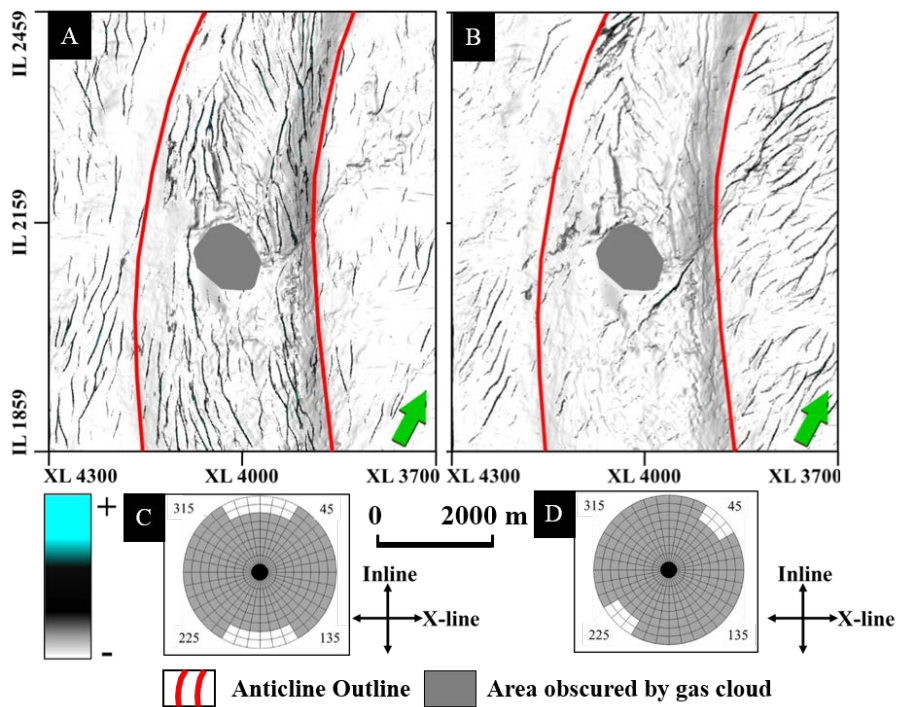


Figure 41 A. and B. Ant-tracking faults obtained from the different aperture directions displayed on the top reservoir surface. C. Stereo-net tab illustrating the accepted search direction for agents to obtain the fault cube (A). D. Stereo-net tab illustrating the accepted search direction for agents to obtain the fault cube (B).

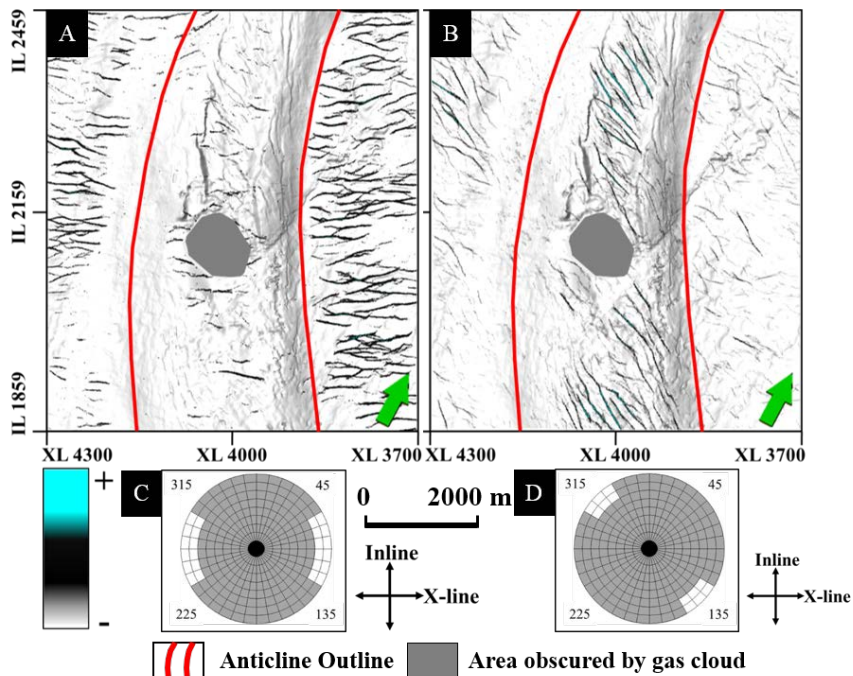


Figure 42 A. and B. Ant-tracking faults obtained from the different aperture directions displayed on the top reservoir surface. C. Stereo-net tab illustrating the accepted search direction for agents to obtain the fault cube (A). D. Stereo-net tab illustrating the accepted search direction for agents to obtain the fault cube (B).

5.4. Seismic AVO Inversion

Figure 43 illustrates the AVO inversion workflow used during this study. Well log data, and reservoir top and bottom surfaces were used for building the low-frequency model, typically for the P- and S-impedance and the density. For the three angle stacks, the wavelets were extracted. Finally, AVO inversion was done using the extracted wavelets and the low-frequency models.

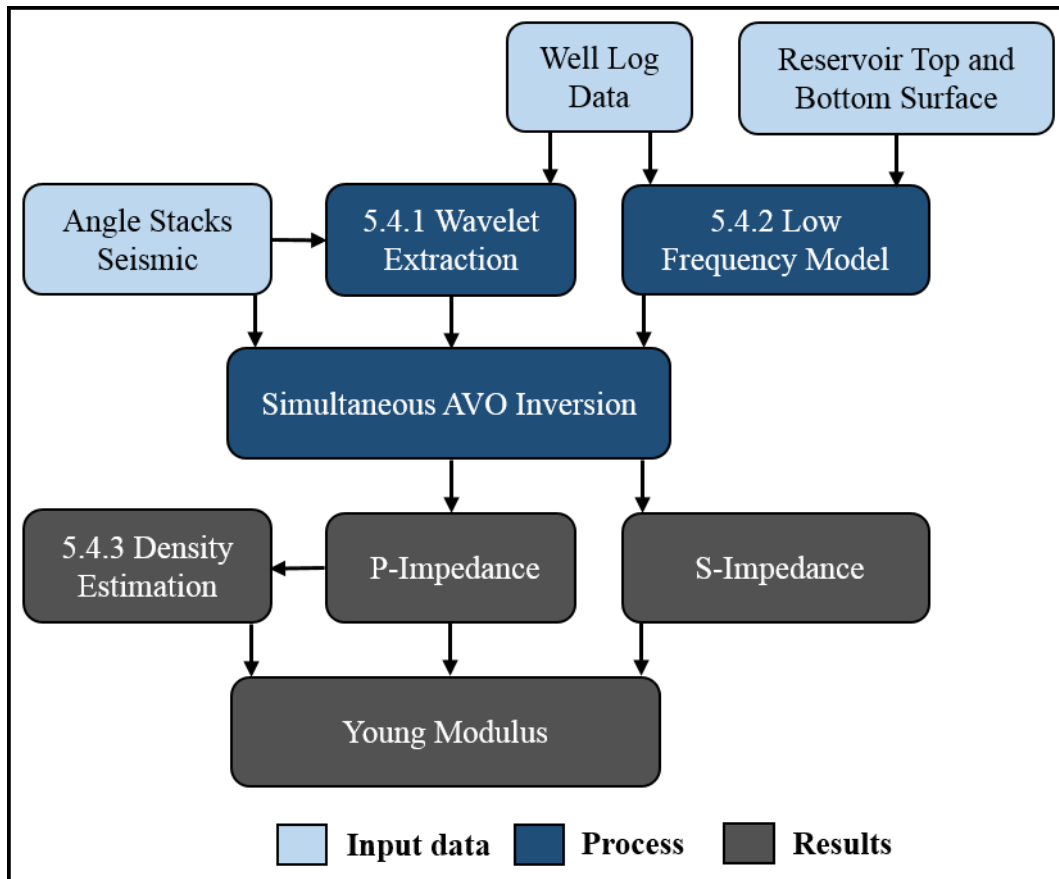


Figure 43 AVO Inversion workflow illustrating the input data, process and the results obtained. The numbers in the text boxes represent the sub-chapter where the particular study is discussed.

The performance of the inversion depends on the quality of the pre-stack migration method applied to the raw seismic data, seismic data of high S/N (signal-noise ratio), and the quality of well log data available. Even in the presence of perfectly migrated, noise-free seismic data, the reliability of the inversion can always be challenged (Contreras et al., 2006). Apart from the above factors, the number of angle-stacks plays a crucial role for the accuracy of the estimated properties, especially the density, resulting from the AVO Inversion. Contreras et al. (2006) show that with few angle stacks, density is the least accurate estimated parameter, whereas P- and S- Impedance are the most accurate and reliable estimated parameters. In this study, the seismic data contains three angle-stacks, whose number is not sufficient to obtain a reliable density

estimation. Therefore, as illustrated in Figure 43, a different approach was used to estimate the density, i.e., estimating density from P-impedance cube.

5.4.1. Wavelet Extraction

Extracting the wavelet from the seismic data is essential for deriving a reliable seismic inversion. For the AVO inversion in this study, deterministic wavelets were extracted from the three angle stacks seismic (Figure 44) using the Zoeppritz approximations (Section 4.4.1). Figure 44 (A.ii, B.ii, and C.ii) shows that the power frequency spectrum is shifted to lower frequencies from near to far stack seismic.

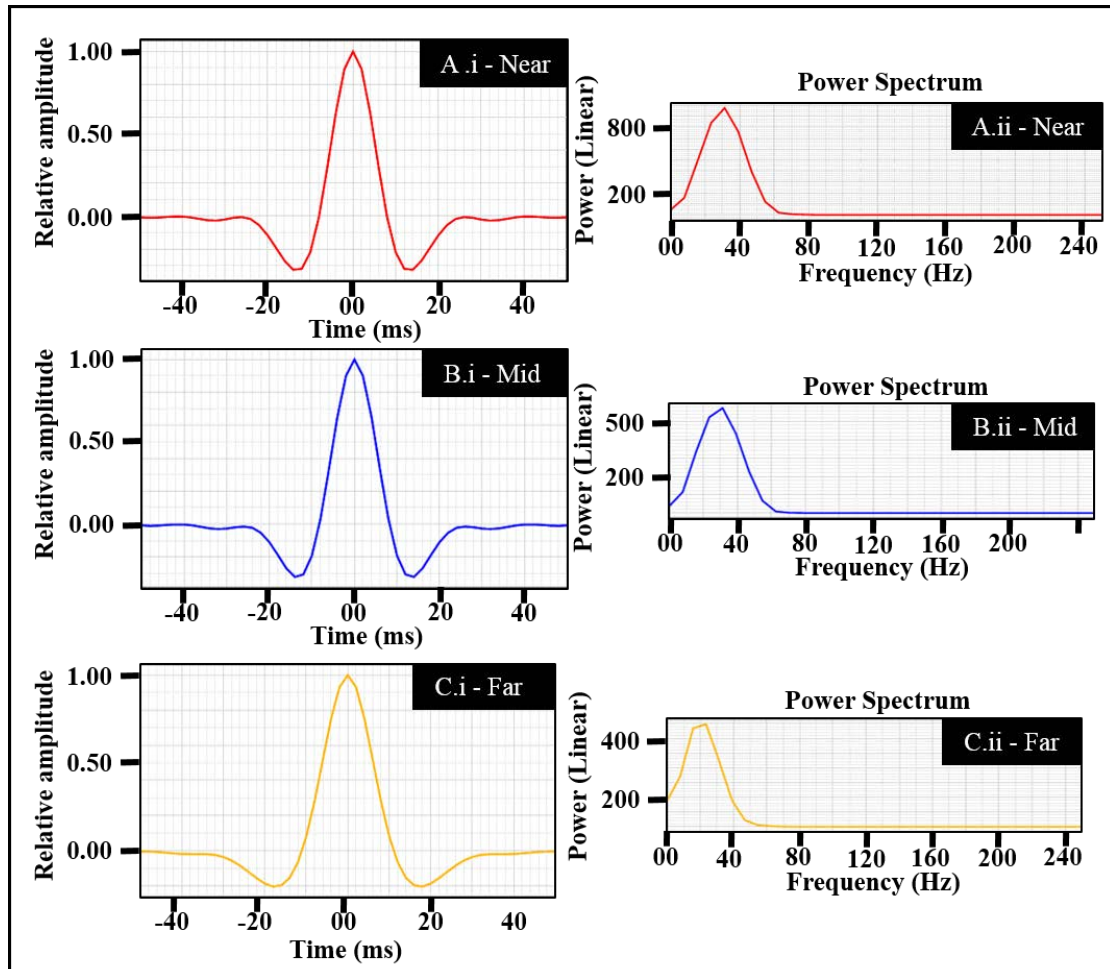


Figure 44 A.i Deterministic wavelet extracted from near stack seismic. A.ii Power spectrum of deterministic wavelet extracted from near stack seismic. B.i Deterministic wavelet extracted from mid stack seismic. B.ii Power spectrum of deterministic wavelet extracted from mid stack seismic. C.i Deterministic wavelet extracted from far stack seismic. C.ii Power spectrum of deterministic wavelet extracted from mid stack seismic.

5.4.2. Low-Frequency Model

The Low-Frequency Model (LFM) enhances the seismic inversion results by introducing the slowly varying trends of the P- and S- inversion and the density (Section 4.4) (Figure 23). The data used for low frequency modelling in this study are the interpreted horizons and the well logs for the P- and S- impedance and the density. The low-frequency model of these three attributes is based on the Moving Average algorithm that interpolates the well data within the space defined by the seismic cube to be inverted. The interpreted seismic horizons define the zones within which the interpolation of the well data is done. The frequency spectrum of the seismic data plays an important role in the low-frequency modelling since it provides the information about the elastic properties of the study area below the seismic bandwidth of the dataset (Section 4.4; Figure 22). Therefore, a high-cut filter of 14 Hz was applied to the interpolated log cubes to obtain the final low-frequency model (Figure 45). A low-frequency model of the P- and S-impedance along with the interpreted top and bottom surface is shown in Figure 46. This figure shows that the P- and S-impedance value decreases from the overburden to the reservoir.

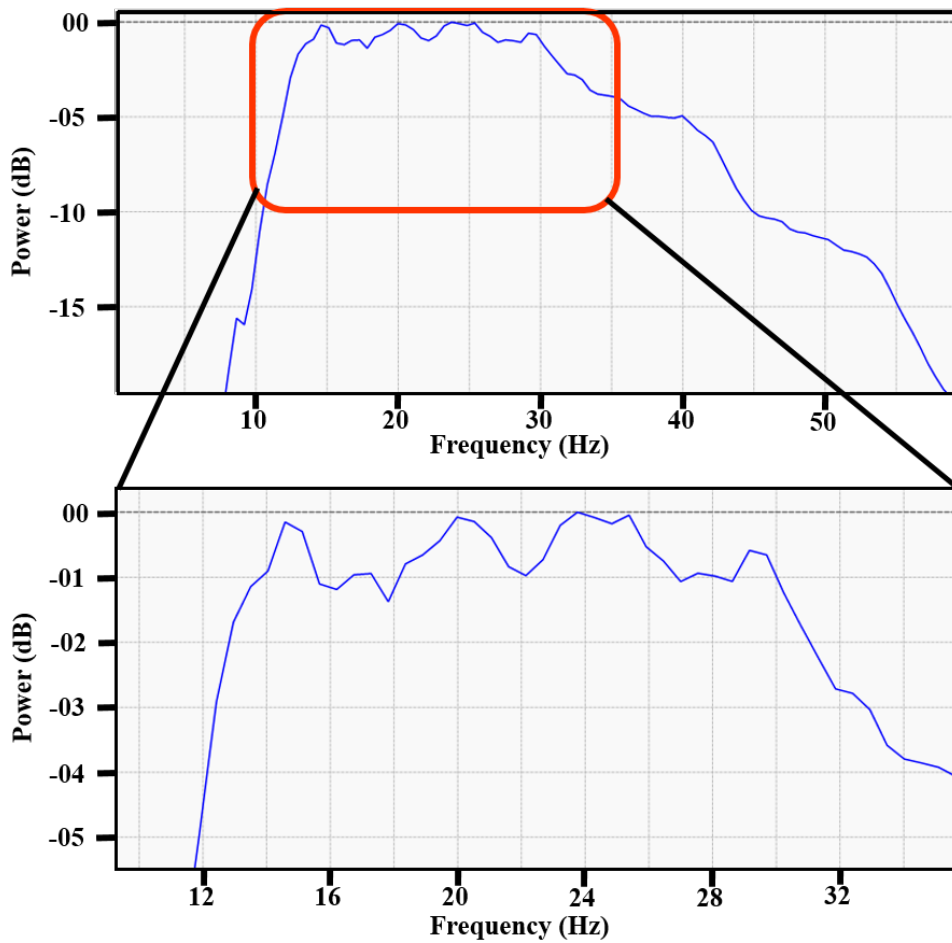


Figure 45 Frequency spectrum of the seismic data used for low-frequency model.

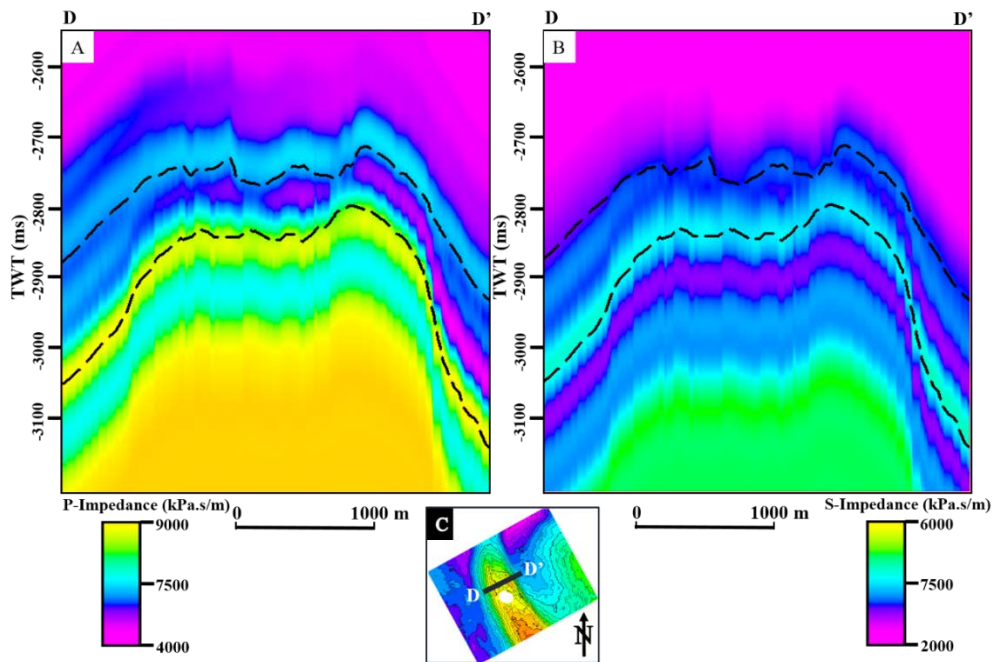


Figure 46 A. Low-frequency model of P-impedance. The black dotted line shows the interpreted top and bottom surface. B. Low-frequency model of S-impedance. C. Top Ekofisk surface with navigation of cross section D-D' shown in A and B.

5.4.3. Density Estimation

As discussed in the AVO inversion workflow, the density cube is the least reliable parameter obtained from AVO inversion while using few angle stacks. In this approach, a best-fit polynomial equation from the cross-plot of the acoustic impedance log and the density log for the depth range used in the inversion was used to derive the density cube from the P-Impedance cube (Figure 47). P-Impedance cube results from the AVO inversion.

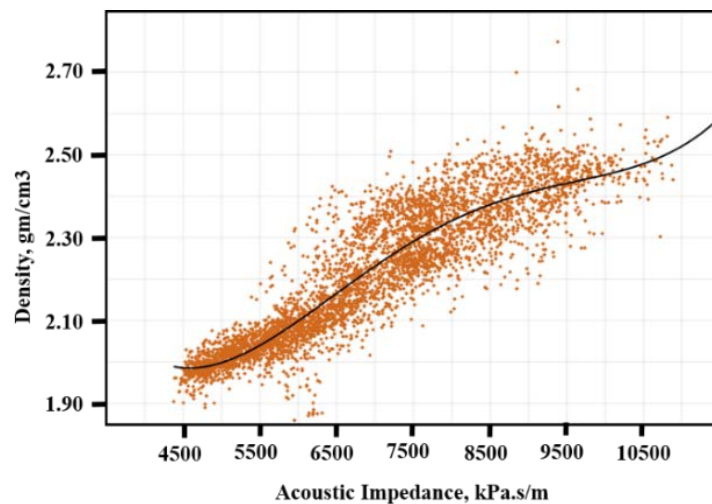


Figure 47 Cross-plot of acoustic impedance log versus density log for the wells of the reservoir. The black line shows the best-fit polynomial function used for computing the density cube from the P-impedance cube.

5.5. Fracture Modelling

Figure 48 illustrates the time to depth conversion and the 3D grid construction workflow. Seismic horizons and seismic cubes (i.e., Young Modulus cube and Seismic Attributes cubes) were converted into depth domain using the velocity model obtained from Hess Corporation. Then a 3D grid was constructed using depth converted seismic horizons as surfaces and the depth converted seismic attribute cubes were resampled into the 3D grid. The resampled cubes, i.e., t^* attenuation, variance, and Ant-tracking cubes were cross-plotted against the Young Modulus cube along the wells to observe the relation between the seismic attributes and the Young Modulus.

The selection of the grid size is one of the sensitive parameters in the construction of the 3D grid (Hassanpour and Deutsch, 2010) (Section 4.5). A larger grid size does not preserve the geological shapes, and on the other hand, a smaller grid size leads to more significant number of grid cells and consequently longer computational times (Hassanpour and Deutsch, 2010). A grid size of 50 m by 50 m was used in this study. Vertical layering, another important parameter in constructing the 3D grid, is defined as the internal layering that divides the zones between the surfaces. In this study, the 3D grid was divided into 100 vertical layers resulting in a vertical resolution of ca 2 metres.

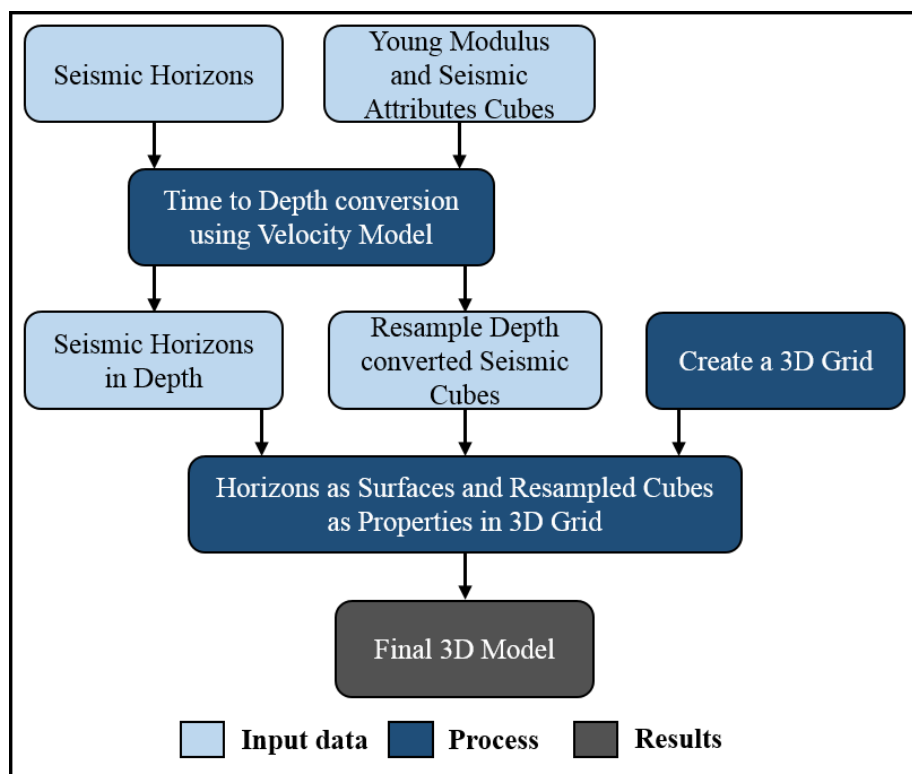


Figure 48 Time to depth conversion and the 3D Grid construction workflow illustrating the conversion of horizons and seismic cubes into the depth domain and the construction of a 3D grid using horizons as surfaces.

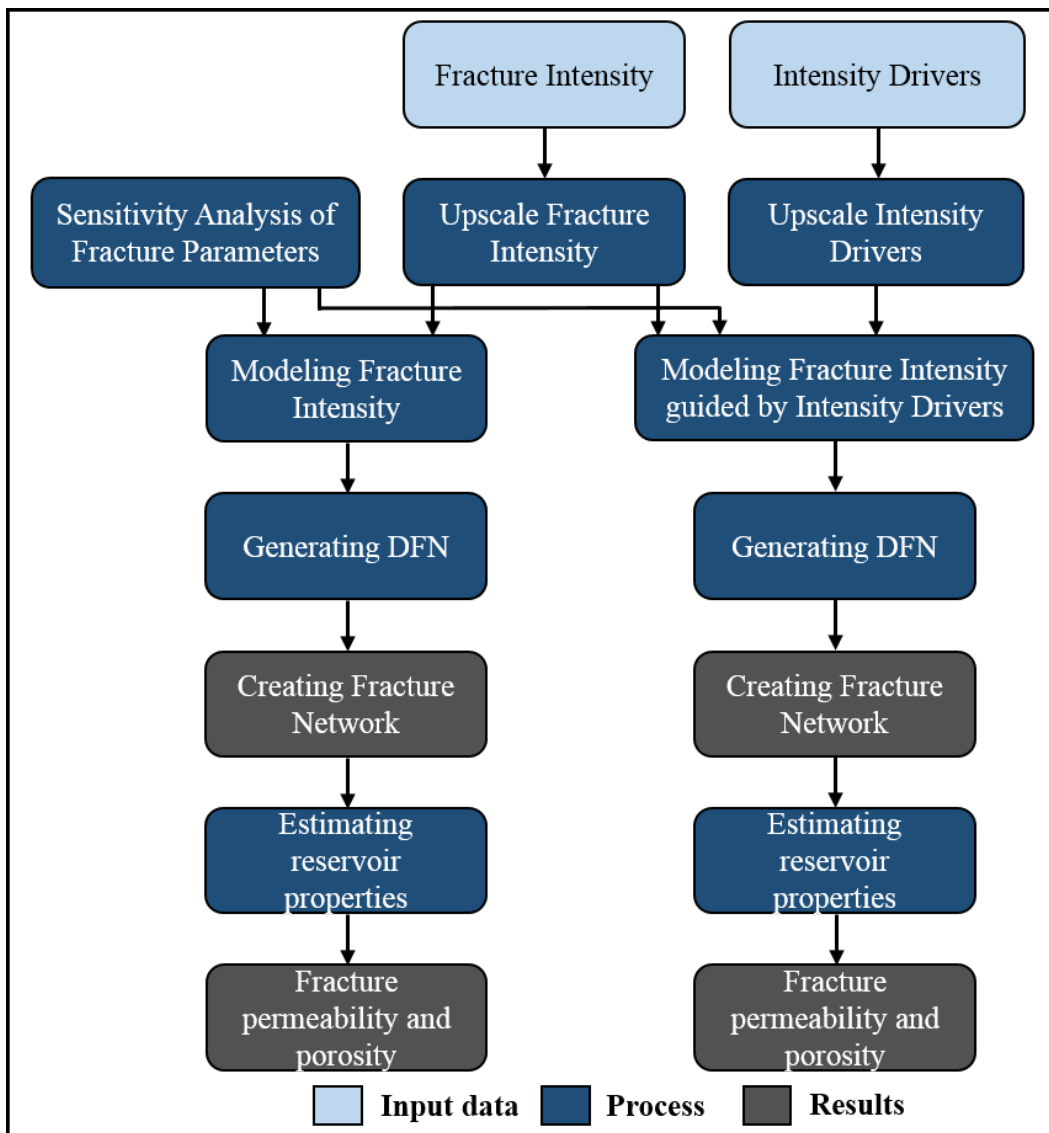


Figure 49 Fracture modelling workflow based on the fracture intensity and intensity drivers as the input data.

Figure 49 illustrates the workflow that was followed for the fracture modelling study. Fracture intensity data calculated from the well log, and the Young Modulus obtained from seismic inversion and seismic attributes (i.e., variance, ant tracking, t^* attenuation) were used as the input data. The Young Modulus and seismic attributes (secondary variables) are the intensity drivers used for modelling fracture intensity (primary variable) (Section 4.5.1.1). Fracture intensity is modelled with and without the intensity drivers (Figure 49). These different models help in observing the impact of intensity drivers on the resulting permeability model. The generation of the DFN modelling (grey blue coloured box in Figure 49) involves two primary processes: creating the fracture network, and upscaling the fracture network properties, i.e.,

fracture porosity and fracture permeability into the 3D grid. Reservoir engineers use this 3D grid for flow simulation that allows calibrating the permeability model.

Since the direct determination of most fracture parameters is difficult or even impossible, it is essential to know the impact of these fracture parameters on the permeability. This can be achieved by doing a sensitivity analysis study (Figure 49). The results of this analysis deliver the parameters that are most influential on the permeability and consequently should be handled with special care.

5.5.1. Sensitivity Analysis of Fracture Parameters

A sensitivity analysis study was performed to investigate the impact of fracture concentration (Section 4.5.1.3), fracture aperture (Section 4.2.1) and fracture length on the permeability model. This study was done on a synthetic 3D model of simple geometry and geological layering to neglect the effect of other factors such as changes in lithology, and layer geometry.

The influence of a fracture parameter on the modelled permeability was captured by building fracture models for different values of this parameter while keeping all other parameters at their base case values. Table 4-6 gives the assumed base case values for the main fracture parameters together with the value range for the fracture concentration, fracture aperture and fracture length used for the sensitivity analysis. The fracture orientation was described in terms of mean dip angle and azimuth. It was modelled with the Fisher distribution (Section 4.5.1.3) due to the simplicity of this algorithm. For each fracture model, the fractures and their permeability were upscaled into the 3D grid and the permeability in the i, j and k direction calculated. Note that the indices i,j, and k describe the local orientation of the individual grid cells. All static modelling is typically done in the i,j,k coordinate system.

This study allows ranking the fracture parameters according to their influence on the permeability. This way, the parameters with the highest influence on the permeability model are identified.

Table 4 Different values of concentration (marked in bold) used in the sensitivity analysis study.

Case	Concentration	Mean Dip (Degrees)	Mean Azimuth (Degrees)	Aperture (metres)	Length
Case 1	.5	90	0	0.000075	500
Case 2	1	90	0	0.000075	500
Case 3	2	90	0	0.000075	500
Case 4	4	90	0	0.000075	500
Case 5	8	90	0	0.000075	500

Table 5 Different values of fracture aperture (marked in bold) used in the sensitivity analysis study.

Case	Concentration	Mean Dip (Degrees)	Mean Azimuth (Degrees)	Aperture (metres)	Length
Case 1	.5	90	0	0.000075	500
Case 2	.5	90	0	0.00015	500
Case 3	.5	90	0	0.0003	500
Case 4	.5	90	0	0.0006	500
Case 5	.5	90	0	0.0012	500

Table 6 Different values of fracture length (marked in bold) used in the sensitivity analysis study.

Case	Concentration	Mean Dip (Degrees)	Mean Azimuth (Degrees)	Aperture (metres)	Length
Case 1	.5	90	0	0.000075	500
Case 2	.5	90	0	0.000075	400
Case 3	.5	90	0	0.000075	300
Case 4	.5	90	0	0.000075	200
Case 5	.5	90	0	0.000075	100

5.5.2. Fracture Modelling guided by Intensity Drivers

The resampled cubes, i.e., Young Modulus, variance, Ant-tracking and t^* attenuation cubes were used as drivers for guiding the fracture intensity (Figure 48). The spatial variation in the resampled cubes was estimated via horizontal and vertical variograms (Section 4.5.1.1). The well data do not provide a reasonable estimation of the horizontal

variogram range. On the other hand, the vertical wells provide a reliable estimation of vertical variogram because of the densely sampled fracture intensity logs. Obviously, the horizontal wells cannot provide a reliable estimation of the vertical variogram range, and the only vertical well with the fracture data had reference depth issue. Consequently, the resampled seismic cubes were used for estimating both, the horizontal and vertical variogram range. The modelled variogram was then used in collocated co-kriging (Section 4.5.1.1) to guide the fracture intensity using a seismic resampled cube as the secondary variable. The correlation factor controls the influence of the secondary variable on the fracture intensity. A large correlation factor was used in collocated co-kriging because the assumption is that the fractures are associated with faults. The variogram range used in this study is illustrated in Table 7.

Table 7 Variogram ranges in major, minor and vertical direction for the fracture drivers.

Intensity Driver	Horizontal Direction (metres)	Vertical Direction (metres)
Variance	900	30
Young Modulus	850	25

Estimating reservoir properties

The fracture parameters estimated based on sensitivity analysis and the analogue data were used to generate different fracture models. Based on the fracture study of the well data, the preferred direction of fractures was used as an input for the fracture orientation concentration. The Bingham model (Section 4.5.1; Figure 30) was used for modelling the direction of the fractures since it allows controlling their radial and azimuthal concentration.

The sensitivity analysis study of the permeability shows the minor impact of fracture length on the permeability. Therefore, the high case fracture length (i.e., 500 metres) was selected because it is much less CPU demanding compared to the modelling of smaller fracture lengths. The fracture aperture value was selected based on a fracture aperture study done on chalk reservoirs of the North Sea (Buller et al., 1990). The power law (Table 3) was used for modelling the fracture aperture distribution and fracture length distribution. Figure 50-A shows the histogram of fracture length modelled by the power law. A similar relation was obtained for the fracture aperture distribution based on the power law. Figure 50-B shows the relation between fracture aperture and fracture permeability defined by cubic law (Equation 4).

The different fracture models use the same fracture parameters but are based on different approaches of fracture intensity interpolations (i.e., without intensity driver,

with Young Modulus as fracture intensity driver and seismic attributes as fracture intensity driver). These fracture models were upscaled into the 3D grid that represents the South Arne reservoir. For the upscaling of the fracture permeability, the Oda method was used (Section 4.5.1.4).

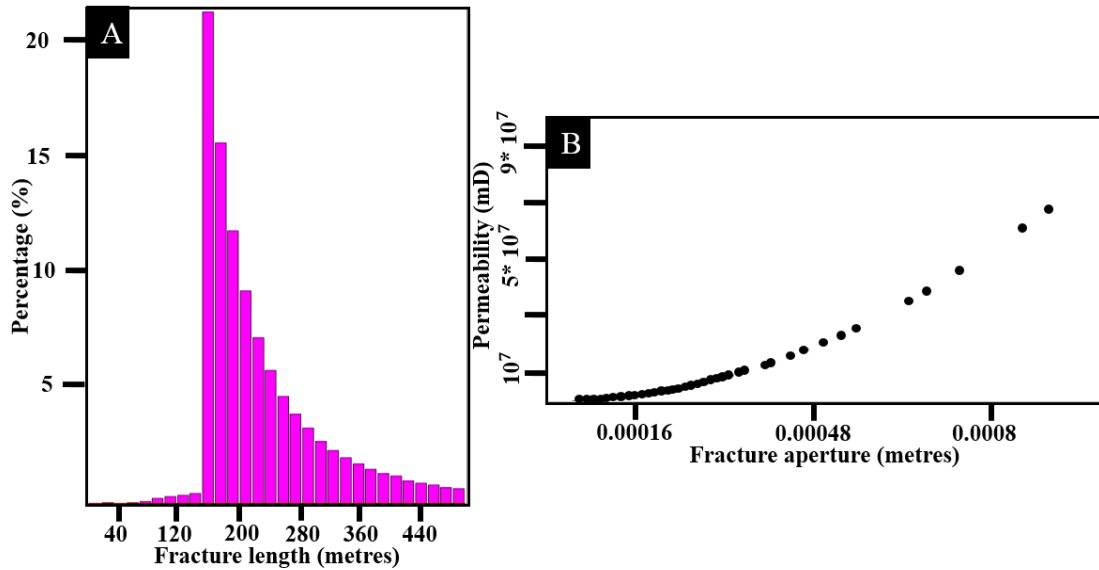


Figure 50 A. Fracture length histogram modelled by a power law. B. The relation between fracture aperture and fracture permeability defined by cubic law. Note that the Permeability-Fracture aperture cross-plot is displayed in semi-logarithmic scale.

6. RESULTS

This chapter presents the key results obtained by following the methodology discussed in Chapter 5. It consists of four main sections: Rock physics study, faults and fractures study, seismic inversion and comparison with seismic attributes, and fracture modelling study. Section 6.1 presents the rock physics results obtained by using the key wells in the area. Section 6.2 shows the faults and fractures study and is sub divided in two parts: Seismic faults and well fracture data. The seismic faults study shows the results obtained from the seismic data using the seismic attributes discussed in Section 5.3. The well fracture study shows the different fracture trends obtained from the well log data. Section 6.3 shows the results of the seismic inversion and compares the Young modulus obtained from the inversion with the seismic attributes. Section 6.4 shows the fracture modelling results. This section is divided into two parts: Sensitivity analysis of the fracture parameters and the South Arne fracture modelling.

6.1. Rock Physics Study

As described in Section 5.2.3, rock properties were cross-plotted to understand the rock physics properties that may influence the fracture intensity of the two reservoir formations. Additionally, it is analysed whether the Young Modulus can be used to guide the modelling of the fracture intensity.

Figure 51 shows the log data of the Rigs-2 well. The location of this well is displayed in Figure 52. The three intervals in Figure 51 are the two reservoir formations (i.e., Ekofisk and Tor formations) delineated by the ETZ. Figure 51 shows that the ETZ is distinguishable from the two formations based on density, neutron porosity, p-wave velocity, and s-wave velocity. It is characterised by low porosities whereas the other logs show higher values compared to the Ekofisk and Tor formations (Figure 51).

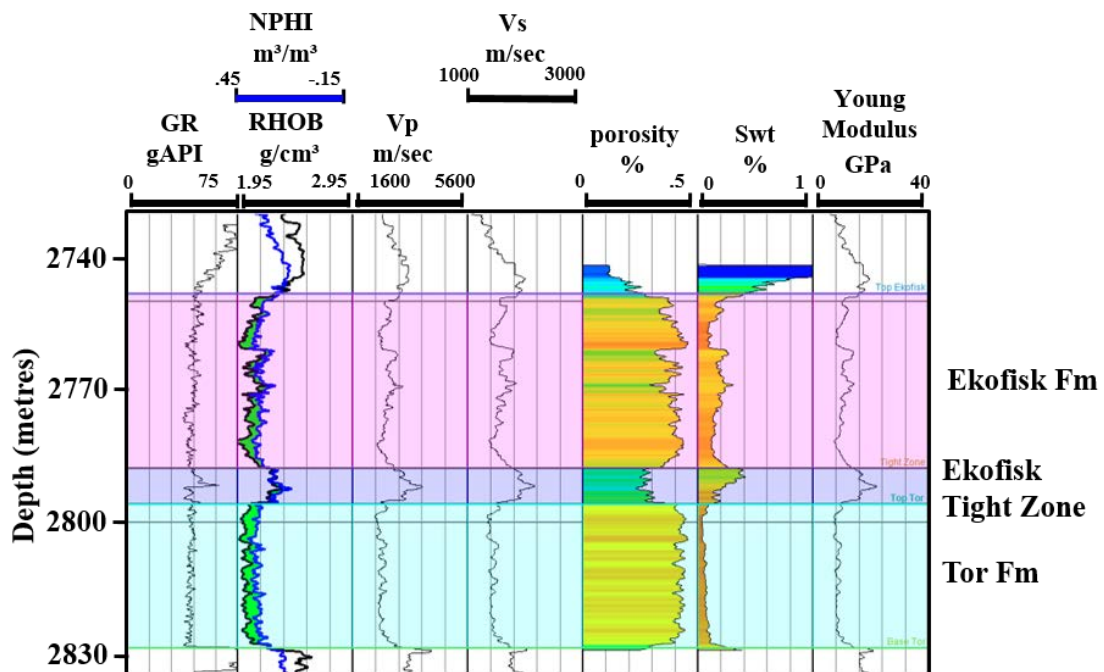


Figure 51 Gamma-Ray (GR), neutron (NPHI), bulk density (RHOB), compressional wave velocity (Vp), shear wave velocity (Vs), porosity, water saturation (Sw) and Young Modulus log of the Rigs-2 well. For the location of the well, refer to Figure 52. Note the high porosity in both the Ekofisk (upper reservoir) and Tor (lower reservoir) formations. Porosity is more homogenous in the Tor Formation than in the Ekofisk Formation.

Figure 52 shows the location of the wells discussed in Figures 53 and 54. The wells Rigs-1, Rigs-2, Rigs-3c and SA-1 are used for analysing the rock physics properties of the two reservoir formations (Figures 53 and 54). These wells were selected based on the availability of the well logs. In addition, these wells cover the lateral extent of the reservoir, hence, they provide an overview of the rock physics properties within the reservoir. The observations from Figures 53 and 54 are documented in Table 8.

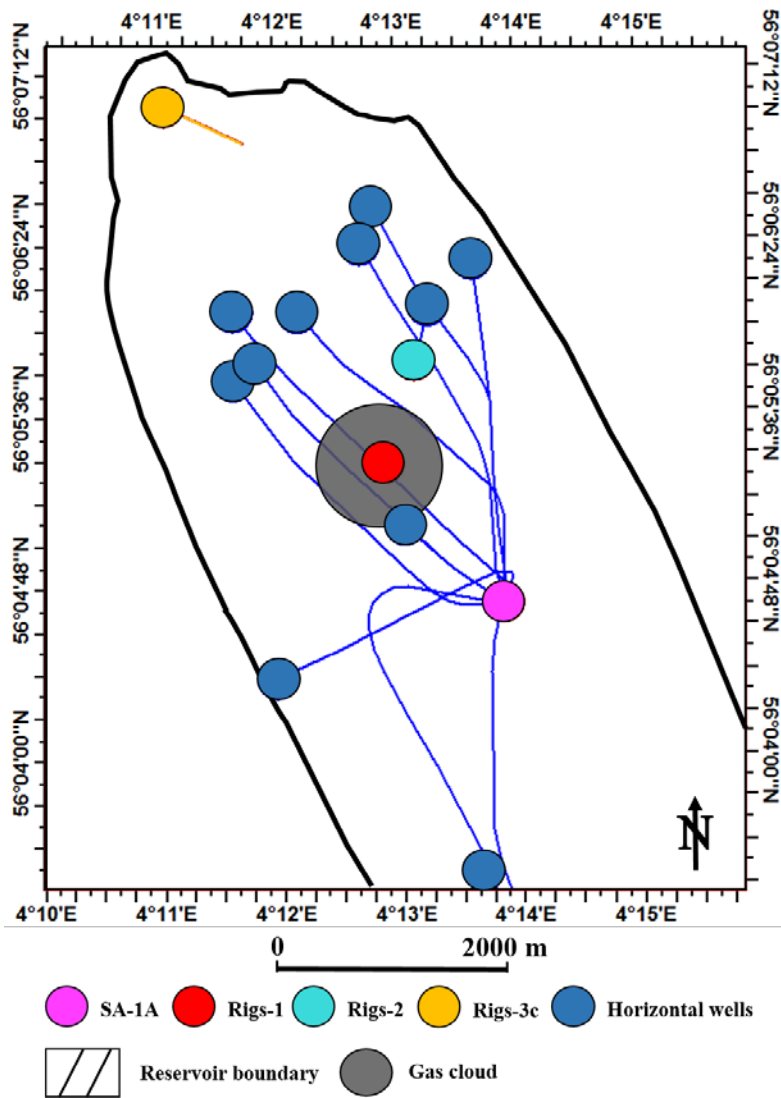


Figure 52 Map showing the location of all wells. This figure is a reference map for Figures 51 to 56.

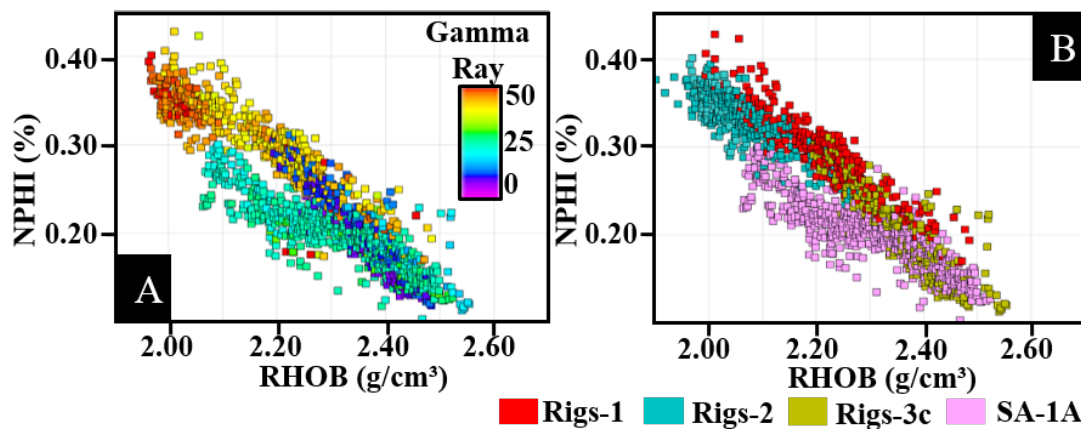


Figure 53 A. Density versus neutron porosity cross-plot colour-coded by Gamma-Ray. B. Density versus neutron porosity cross-plot colour-coded by different wells. For the location of the wells, refer to Figure 52.

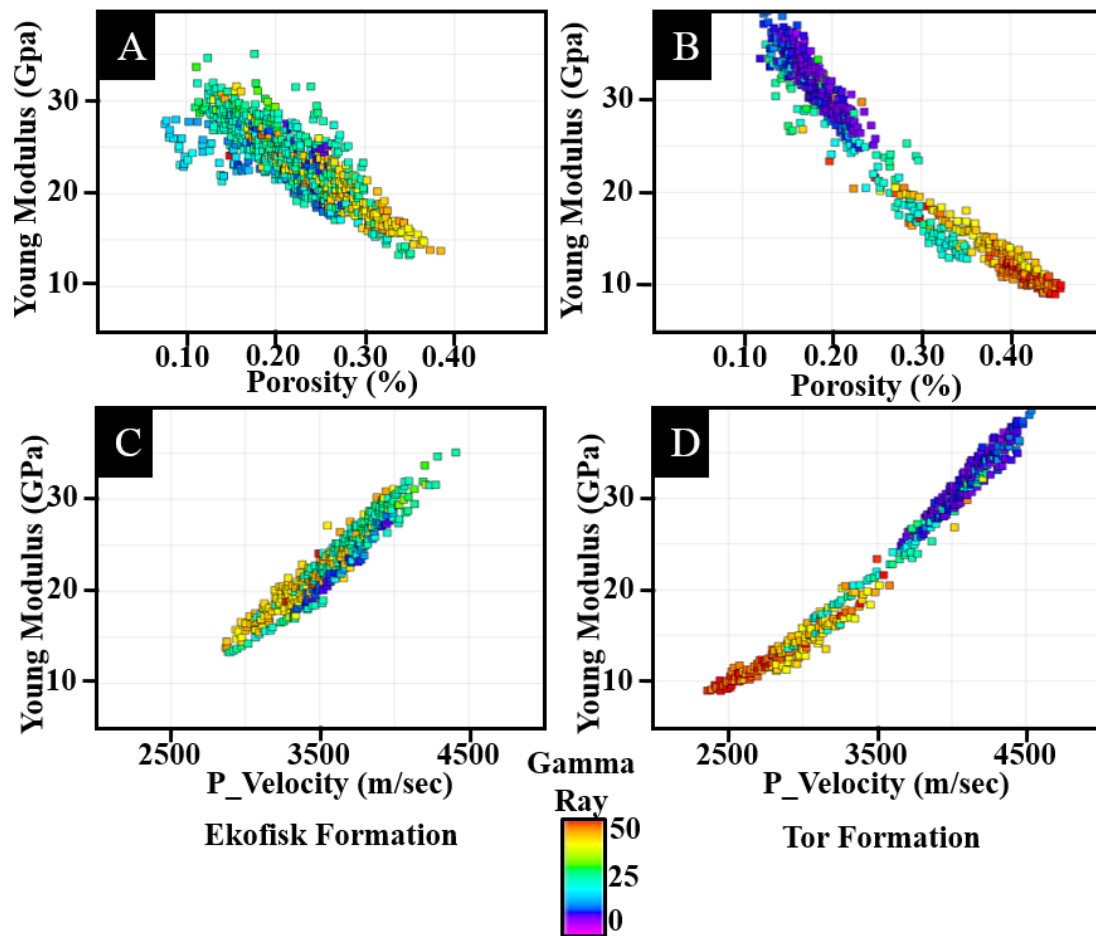


Figure 54 A. Porosity versus Young Modulus cross-plot for Ekofisk Formation color-coded by Gamma-Ray. B. Porosity versus Young Modulus cross-plot for Tor Formation color-coded by Gamma-Ray. C. P-wave velocity versus Young Modulus cross-plot for Ekofisk Formation color-coded by Gamma-Ray. D. P-wave velocity versus Young Modulus cross-plot for Tor Formation color-coded by Gamma-Ray. The data in each plot corresponds to the well Rigs-1, Rigs-2, Rigs-3c and SA-1A. For the location of the wells, refer to Figure 52.

Table 8 Relation between different reservoir properties from Figures 53 and 54.

Type of chalk (characterised based on the Gamma-Ray Log)	Gamma-Ray	Density	Porosity	P-wave Velocity	Young Modulus
Clay-rich Chalk	High GR (Ductile)	Low	High	Low	Low
Clay-poor Chalk	Low GR (Brittle)	Density	Low	High	High

Cross-plots of Figure 54-B and -D show that the Tor Formation has two trends, each one having a different Gamma-Ray (GR) value range. Consequently, these trends can

be associated to clay-rich and clay-poor chalk respectively (Table 8). On the other hand, cross-plots A and C from the Ekofisk Formation show only one trend with no separation between different GR value ranges. Consequently, the chalk of this formation seems to be more heterogeneous compared to the Tor Formation. The combined results from Figure 54-A and -B suggest that there is a scattering in Young modulus values for porosity less than 30%. This scattering could be due to the presence of fractures which will be discussed latter.

Figures 55 and 56 displays the relationship of different rock physics properties with fracture intensity for the Ekofisk and Tor formations. The relationships of high fracture intensity with reservoir properties from Figures 55 and 56 are documented in Table 9.

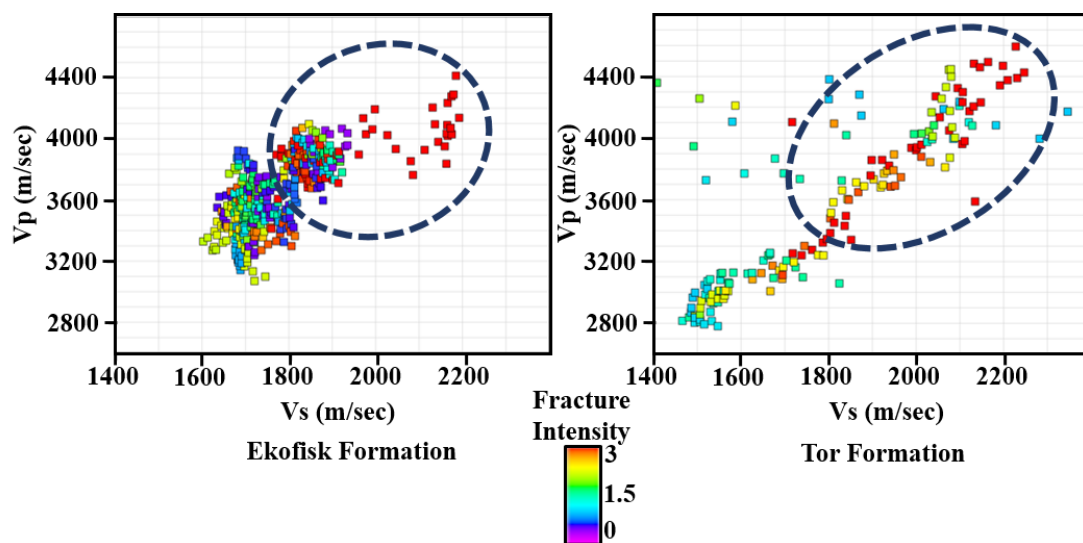


Figure 55 A. S-wave versus P-wave velocity cross-plot colour-coded by fracture intensity for Ekofisk Formation for well SA-1A. B. A. S-wave versus P-wave velocity cross-plot colour-coded by fracture intensity for Tor Formation for well SA-1A. The blue circle represents high fracture intensity points. For the location of the well SA-1A, refer to Figure 52.

Note that fewer data points are present in the Tor Formation for well SA-1A (Figures 55 and 56). However, a similar trend is observed in both formations. Low fracture intensity points are also observed in the area dominated by high fracture intensity points. Observations from Figures 55 and 56 suggest that the reservoir properties are affected by the fractures and there exists a relation between the high fracture intensity and the Young Modulus.

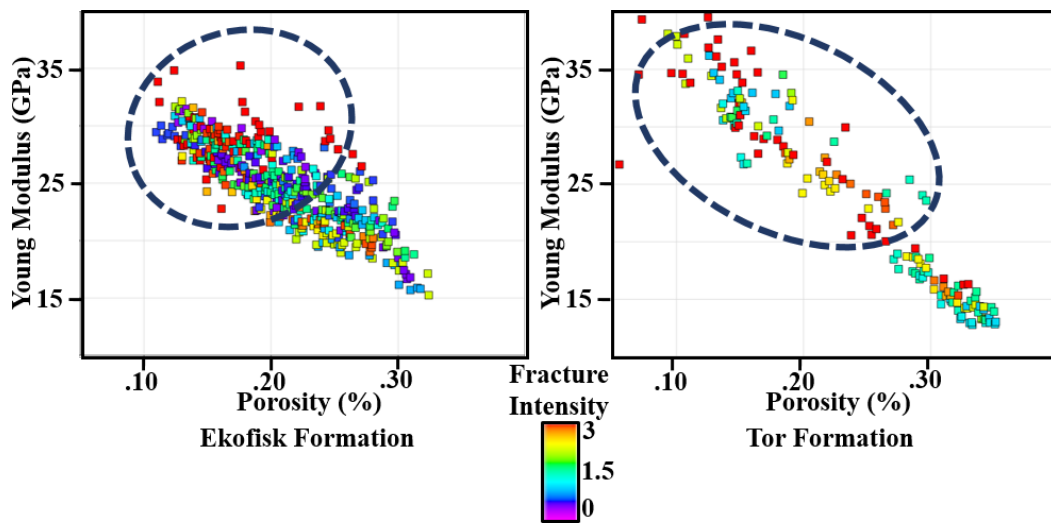


Figure 56 A. Porosity versus Young Modulus cross-plot colour-coded by fracture intensity for Ekofisk Formation for well SA-1A. B. Porosity versus Young Modulus cross-plot colour-coded by fracture intensity for Tor Formation for well SA-1A. The blue circle represents high fracture intensity points. For the location of the well SA-1A, refer to Figure 52.

Table 9 Relation between high fracture intensity and reservoir properties observed from Figures 55 and 56.

Fracture Intensity	P-wave Velocity	S-wave Velocity	Young Modulus	Porosity
High	High	High	High	Low

6.2. Faults and Fractures Study

This study tries to combine the faults and fractures interpreted from the seismic data with the fracture trends interpreted from the well log data. This section gives an overview of the reservoir by showing the top Ekofisk surface interpreted from the 3D seismic data. Faults are interpreted with the help of seismic attributes, namely the Ant-tracking algorithm and variance attribute (Section 5.3.3). In addition, the t^* attenuation attribute (Section 5.3.4) was used as a fracture indicator on the seismic data. The second part of this section discusses the possible influence of the wellbore direction on the measured fracture intensity (Section 5.2.2) and the fracture trends interpreted from the well log data (Section 5.2.1).

6.2.1. Seismic Faults Study

Cross-section A in Figure 57 illustrates a line perpendicular to the WNW-ESE anticline structure south of the gas cloud (Figure 57, cross-section A-II). This figure shows the three different horizons (i.e., top Ekofisk, top Tor and base Tor) and the interpreted faults. The reservoir is thin at the crest of the anticline while it thickens towards the flanks of the structure. The faults die out within the reservoir (i.e., just above Base Tor)

and have shallow dip (Figure 57, cross-section A). Cross-section B in Figure 57 illustrates a random line north of the gas cloud along with the interpreted horizons and faults. The faults offset the whole reservoir and the thickness of the reservoir at the crest of the structure is higher than the one in Cross-section A. Consequently, most of the wells are drilled north of the gas cloud.

Figure 58 illustrates the interpreted Ekofisk surface along with the trajectories of the drilled wells. The figure displays the faults obtained from the stacked aggregated Ant-tracking fault cubes based on the fault cubes of different azimuth directions (Section 5.3.3). The figure shows a northwest plunging anticlinal structure with a collapsed structure to the north of the gas cloud. The different lineament/fault trends observed from the ant tracking algorithm are documented in Table 10.

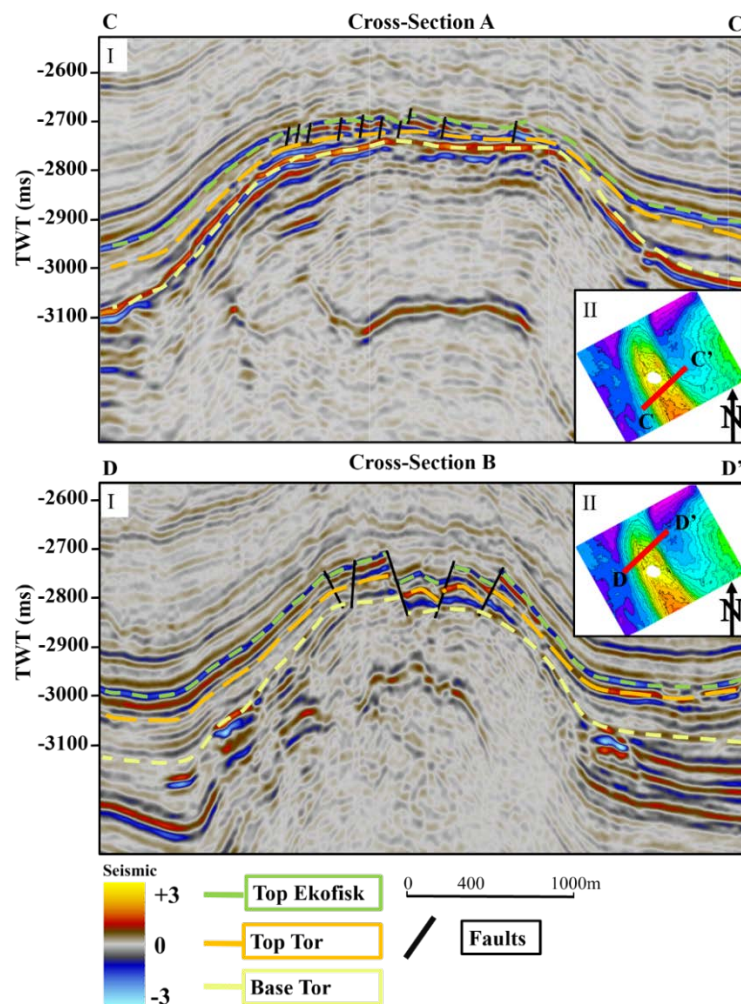


Figure 57 Cross-section A. I. A random line crossing the anticline structure south of the gas cloud. II. Top Ekofisk surface with navigation of cross section C-C'. Cross-section B. I. A random line crossing the anticline structure north of the gas cloud. II. Top Ekofisk surface with navigation of cross section D-D'.

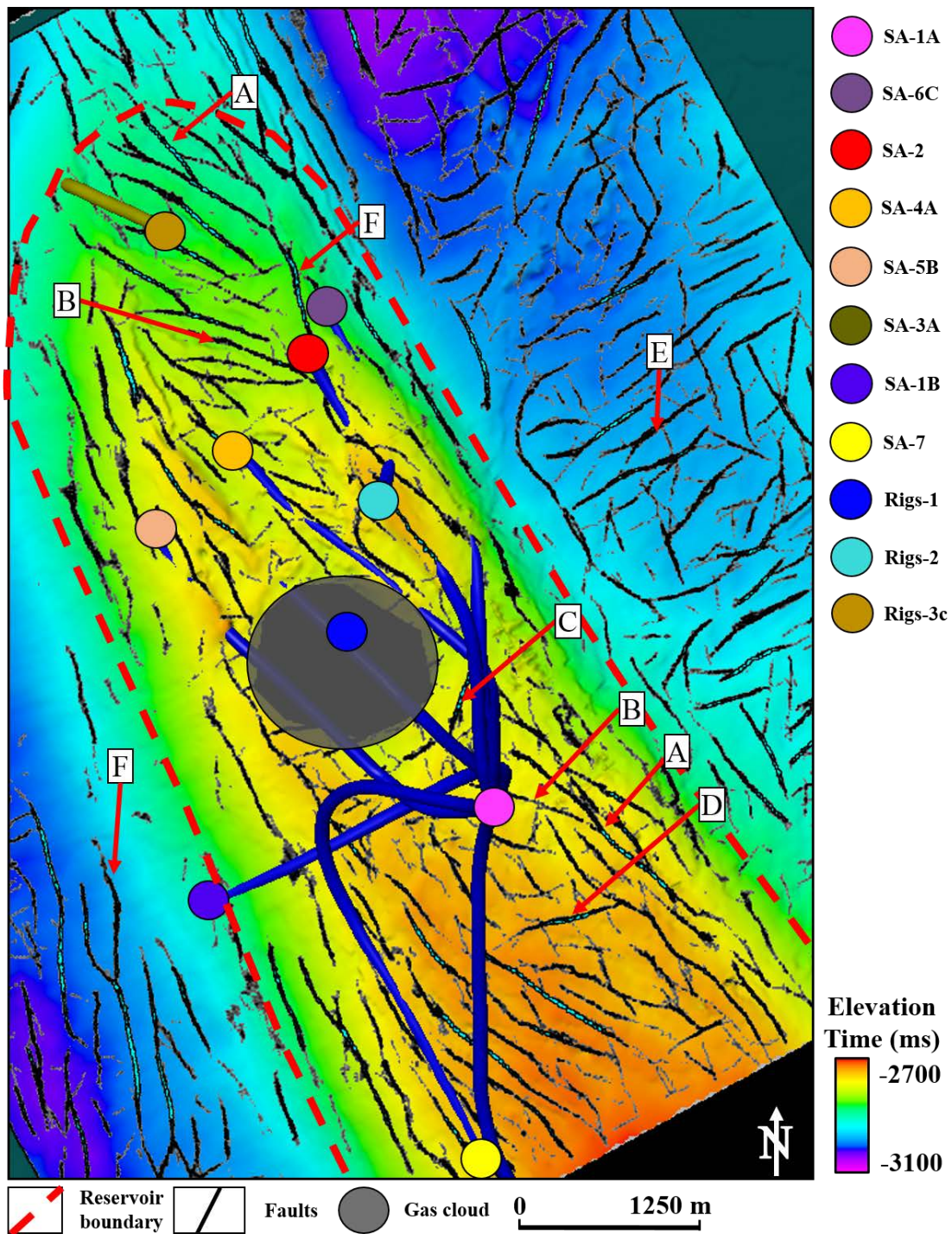


Figure 58 Interpreted top Ekofisk surface along with the trajectories of the drilled wells and the interpreted faults from the aggregated Ant-tracking cube. The wells are colour-coded, and marked circles represent the base location of the wells. The grey circle depicts the area of low-quality seismic data due to the gas cloud. A. NNW-SSE lineament trend observed inside the reservoir boundary. B. WNW-ESE lineament trend observed inside the reservoir boundary. C. NNE-SSW lineament trend present inside the reservoir boundary. D. ENE-WSW lineament trend present inside the reservoir boundary. E. Overburden polygonal faults trending ENE-WSW present outside the reservoir boundary. F. N-S lineament trend present inside the reservoir boundary.

Table 10 Different lineament trends interpreted from the Ant-tracking algorithm. The labels in column 1 corresponds to the labels in Figure 58.

Label	Lineament Trend	Remarks	
		Inside the reservoir boundary	Outside the reservoir
A	NNW-SSE	Observed in the north and south of the gas cloud	Absent
B	WNW-ESE	Most dominant structural trend	Absent
C	NNE-SSW	Few lineaments are observed in the south of the gas cloud	Absent
D and E	ENE-WSW	Few lineaments are observed in the south of the gas cloud (D)	Present (E)
F	N-S	Observed in the eastern shoulder of the crestal graben	Present in SW

Figure 59 illustrates the same random line as Figure 57, cross-section A, but with the faults from the Ant-tracking algorithm. The Ant-tracking algorithm is able to detect shallow dipping faults observed south of the gas cloud.

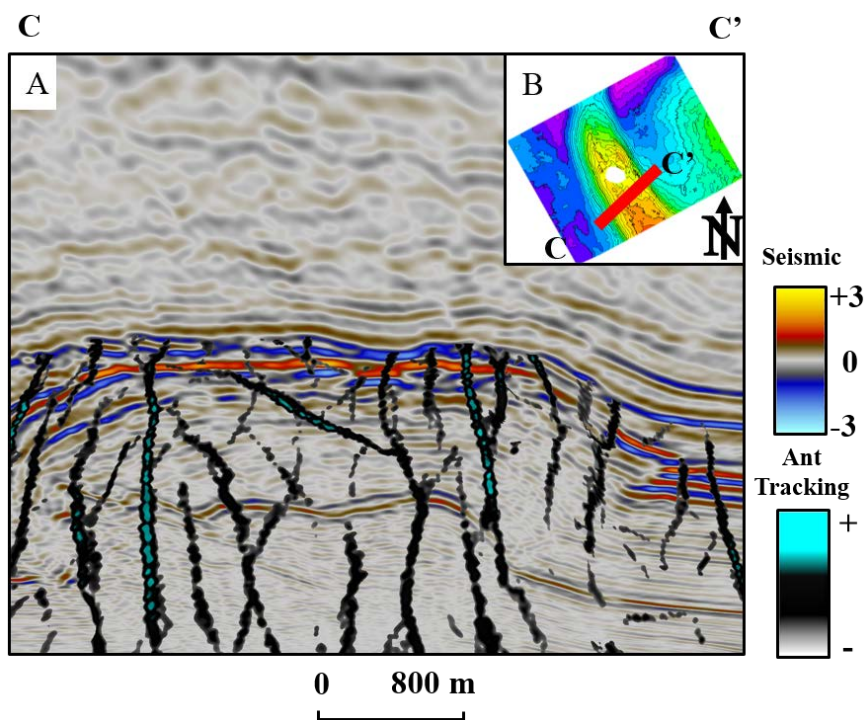


Figure 59 A. A random line crossing the anticline structure south of the gas cloud along with the faults obtained from ant tracking. B. Top Ekofisk surface with navigation of cross section (C-C') shown in A. Note that the location of the random line is the same as that in Figure 57 Cross-section A.

Figure 60-A and -ii illustrates the ENE-WSW lineament trend on the Ekofisk surface obtained from the Ant-tracking algorithm using the stereo-net functionality (Figure 60-B). Figure 60-i and -iii illustrates the E-W lineament trend 150 ms above and below the top Ekofisk surface respectively. The black and blue colour signifies the presence of lineaments. Figure 60-i, -ii and, -iii show that the intensity of the ENE-WSW trending lineaments decreases from the overburden to the reservoir. This decreasing tendency signifies that few or no ENE-WSW trending fractures are expected in the wells within the reservoir zone.

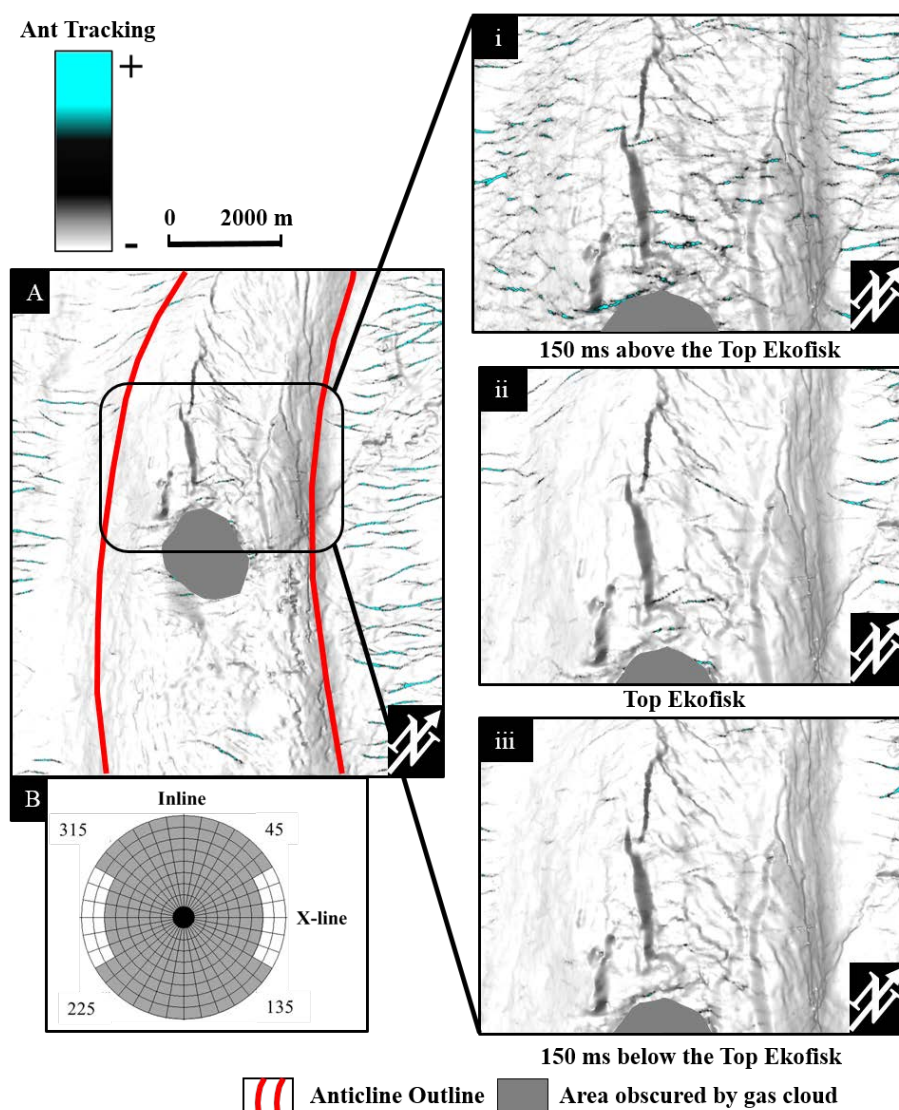


Figure 60 A. Top Ekofisk surface illustrating the ENE-WSW lineament trend obtained from the Ant-tracking algorithm using the stereo-net functionality. The black and blue colour signifies the presence of lineaments. B. Stereo-net used for generating the fault cube for ENE-WSW lineament trend. i. Lineaments extracted 150 ms above the top Ekofisk surface. ii. Lineaments extracted on the top Ekofisk surface. iii. Lineaments extracted 150 ms below the top Ekofisk surface. Note the decrease in ENE-WSW lineaments from i to iii.

Figure 61 illustrates the variance attribute for the time slice (-2730 ms) at the reservoir level. The high value of variance, indicated by red and black is due to discontinuities (i.e., faults). As observed from Figure 61, the variance attribute delineates the different lineament trends of the Ant-tracking results (Figure 58). The variance attribute also delineates the reservoir boundary, and the gas cloud represented by the chaotic pattern (Figure 61). The reservoir boundary is highlighted by a chaotic pattern partly represented by faults and partly by horizons. Some of these chaotic features go radially away from the reservoir.

Table 11 documents the different lineament trends observed from the variance attribute. The labels in column 1 of Table 11 corresponds to the labels in Figure 61. The results obtained from the Ant-tracking algorithm and the variance attribute show that both algorithm capture the different lineament trends and could serve as an intensity driver to guide the fracture intensity modelling.

Table 11 Different lineament trends interpreted from the variance attribute. The labels in Column 1 corresponds to the labels in Figure 61.

Label	Lineament Trend	Remarks	
		Inside the reservoir boundary	Outside the reservoir
A	NNW-SSE	Observed in the north and the south of the gas cloud	Absent
B	WNW-ESE	Higher intensity in the north than in the south of the gas cloud	Absent
C	NNE-SSW	Few lineaments are observed in the south of the gas cloud	Absent
D	ENE-WSW	Absent	Radial Faults
D'			Polygonal Faults

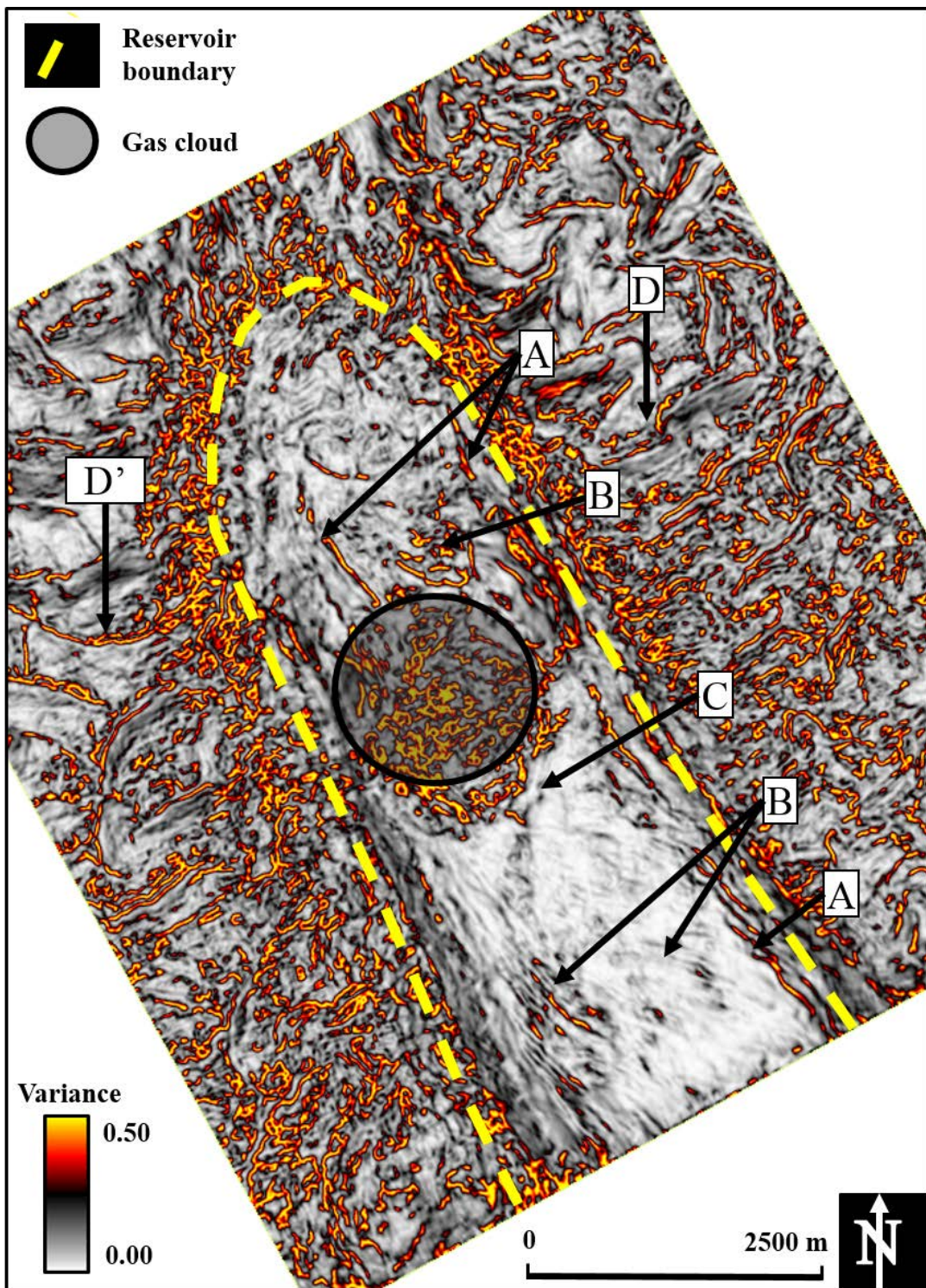


Figure 61 Variance attribute displayed for the time-slice (-2730 ms) within the reservoir. High variance values indicate discontinuities (i.e., faults). The grey circle highlights the area affected by the gas cloud. The yellow dashed line illustrates the reservoir boundary. A: Variance highlighting NNW-SSE lineaments. B: WNW-ESE lineaments. C: NNE-SSW lineaments. D: polygonal faults. D': radial faults.

Figure 62 illustrates the t^* attenuation attribute on the time-slice at -2818 ms cutting the reservoir. As discussed in Section 5.3.4, this attribute has been developed specifically to detect fracture zones. Brown colours signify higher fracture intensity areas while white values indicate lower fracture intensity areas. The figure shows that the region A, i.e., the collapsed region, generally has high t^* attenuation values while region B in the south of the gas cloud, generally has low t^* attenuation values. It is important to note that the t^* attenuation values in region A are oriented in the major lineament direction, i.e., NNW-SSE, and WNW-ESE. Figure 63 highlights these trends on the t^* attenuation attribute time-slice cutting the reservoir.

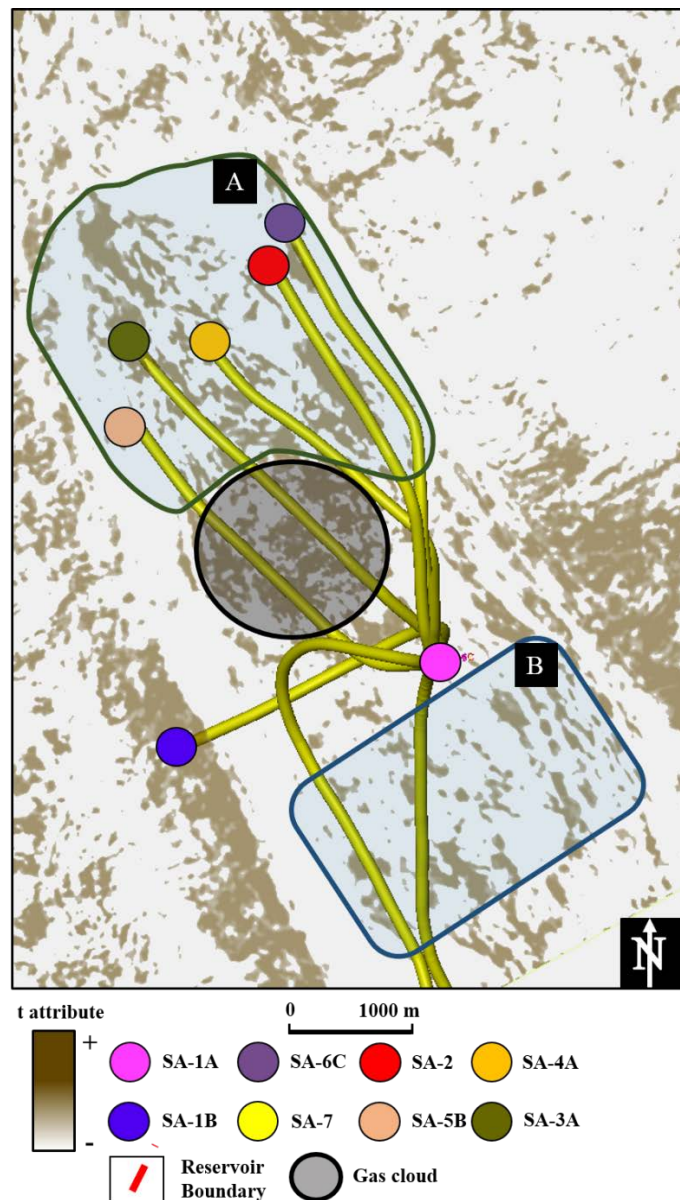


Figure 62 t^* attenuation attribute on the time-slice (-2818 ms) inside the reservoir along with the trajectories of the drilled wells. Region A marks the area of high t^* attenuation values while region B marks the area of low t^* attenuation values.

The orientation of high t^* attenuation values in the direction of the significant lineaments direction suggests that the majority of fracture zones have developed in the vicinity of faults. Another important observation from Figure 63, similar to Figure 62, is that more areas with high t^* attenuation values occur in the Crestal Graben, north of the gas cloud, while high t^* attenuation values are less present in the south of the gas cloud. This observation suggests that more fracture zones can be expected in the north of the gas cloud than in the south. Table 12 documents the lineament trends observed from the t^* attenuation attribute.

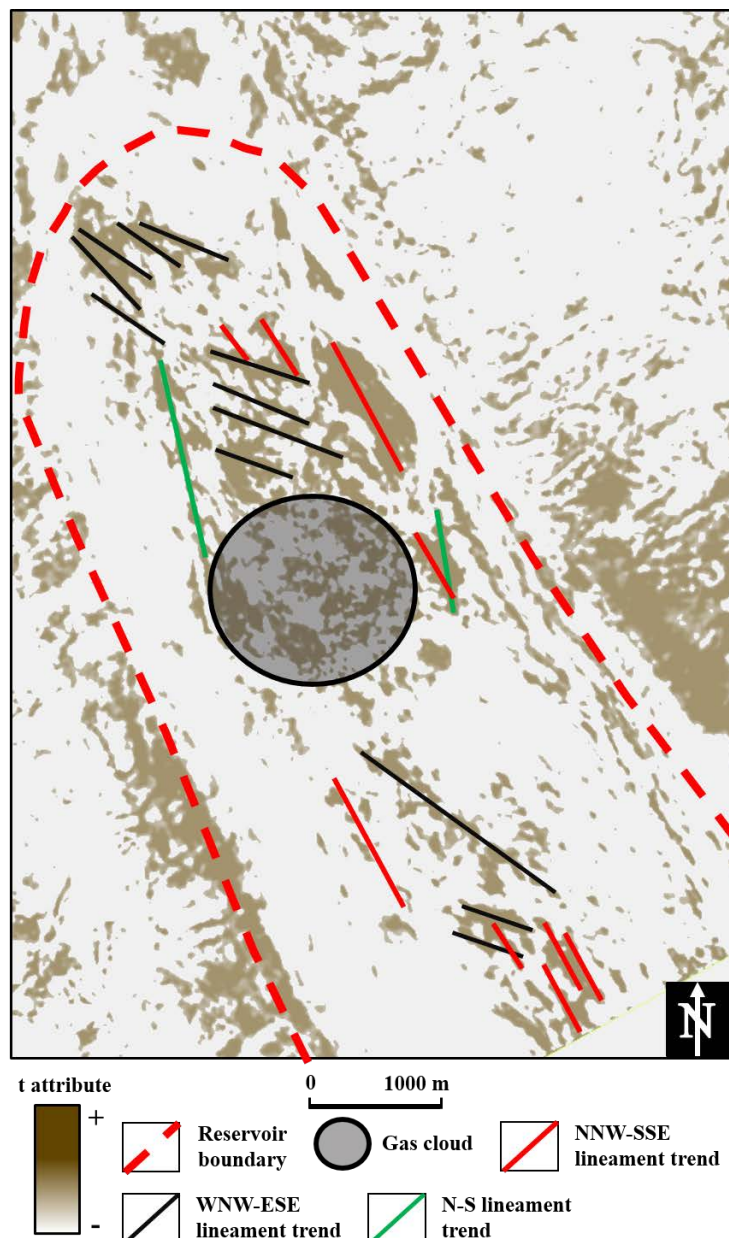


Figure 63 t^* attenuation attribute on the time-slice (-2766) inside the reservoir. Red dashed line indicates the reservoir boundary. The red, black, and green lines represent the NNW-SSE, WNW-ESE, and the N-S lineament trends respectively.

Table 12 Different lineament trends interpreted from the t^* attenuation attribute. The colours in Column 1 corresponds to the colours in Figure 63.

Colour	Lineament Trend	Remarks
Red	NNW-SSE	Observed in the north and south of the gas cloud
Black	WNW-ESE	Observed in the north and south of the gas cloud
Green	N-S	Few lineaments are observed in the north of the gas cloud

6.2.2. Well Fracture Data Study

Influence of well azimuth on fracture data

As indicated in section 5.2.2, the borehole direction may have an impact on the measurement of the fracture intensity. The intention of Figure 64 is to illustrate whether the borehole direction influences the measured fracture data. Figure 64 shows the azimuth histogram of the measured fractures for wells SA-2, SA-6B, and SA-6C. The red dashed line indicates the borehole direction for the three wells. A high count or frequency of fracture points is observed in the direction of the boreholes, thus the effect of borehole direction on fracture data is limited. A similar relation is observed for the other wells.

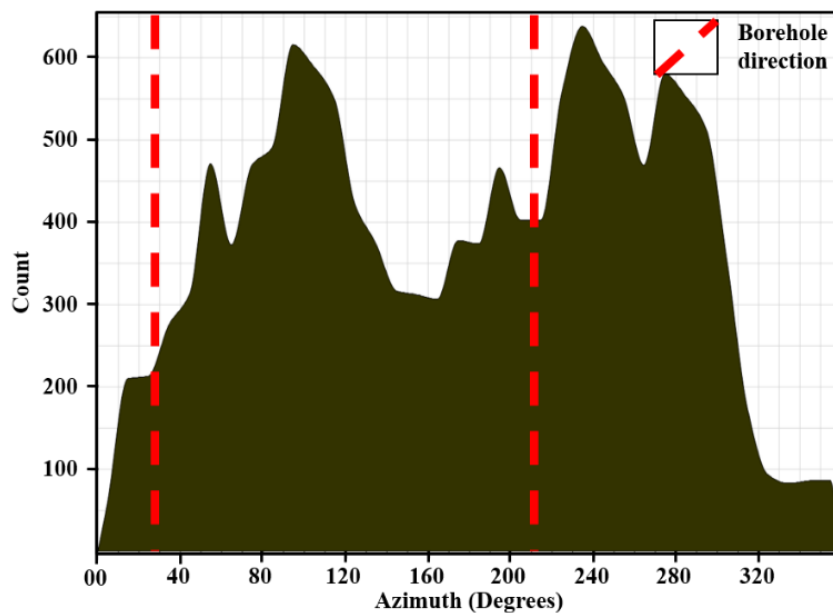


Figure 64 Dip azimuth histogram of fractures for wells SA-2, SA-6B, and SA-6C. Y-axis represents the number of times a particular frequency value is encountered in the dataset. Red dashed lines indicate the borehole direction of the three wells. For the location of the wells, refer to Figure 58.

Fracture Trends Study

As discussed in Section 5.2.1, the study of fracture data by analysing the dip azimuth histogram of each well leads to the interpretation of the different fracture trends. The dip azimuth histogram makes it easier to identify the different trends which are hard to derive from the stereo-net alone. This can also be seen in the stereo-net of well SA-2 (Figure 65). In this figure, the fracture trends are derived from the histogram methodology. To see the dip azimuth histogram for all study wells, please refer to the Appendix, Section 10.1.

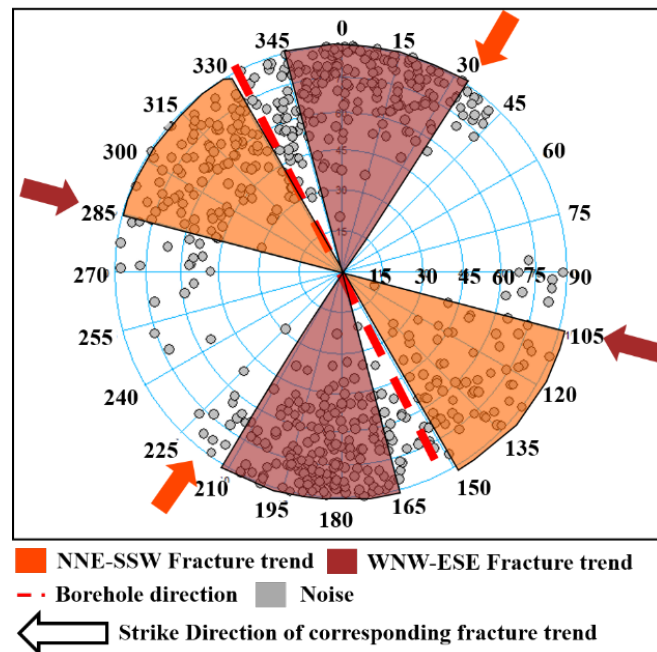


Figure 65 Stereo-net showing the dip azimuth of fracture data for the well SA-2. The coloured area represents the interpreted fracture trends derived from the histogram methodology. Coloured arrows represent the strike directions of the interpreted fracture trends. Grey points outside the coloured area in the stereo-net are noise. For the location of the well SA-2, refer to Figure 58.

Table 13 summarizes the encountered fracture trends at the wells. Figure 66 illustrate the identified fracture trend at each well in the context of the seismic faults derived by Ant-tracking. This figure shows the top Ekofisk surface with the faults interpreted from the Ant-tracking algorithm along with the trajectories of the wells marked with different colours at their bottom depth. The arrows in each part (i.e, Figure 66-A, -B, -C and -D) indicate the different fracture trends of the corresponding well interpreted from the dip azimuth data.

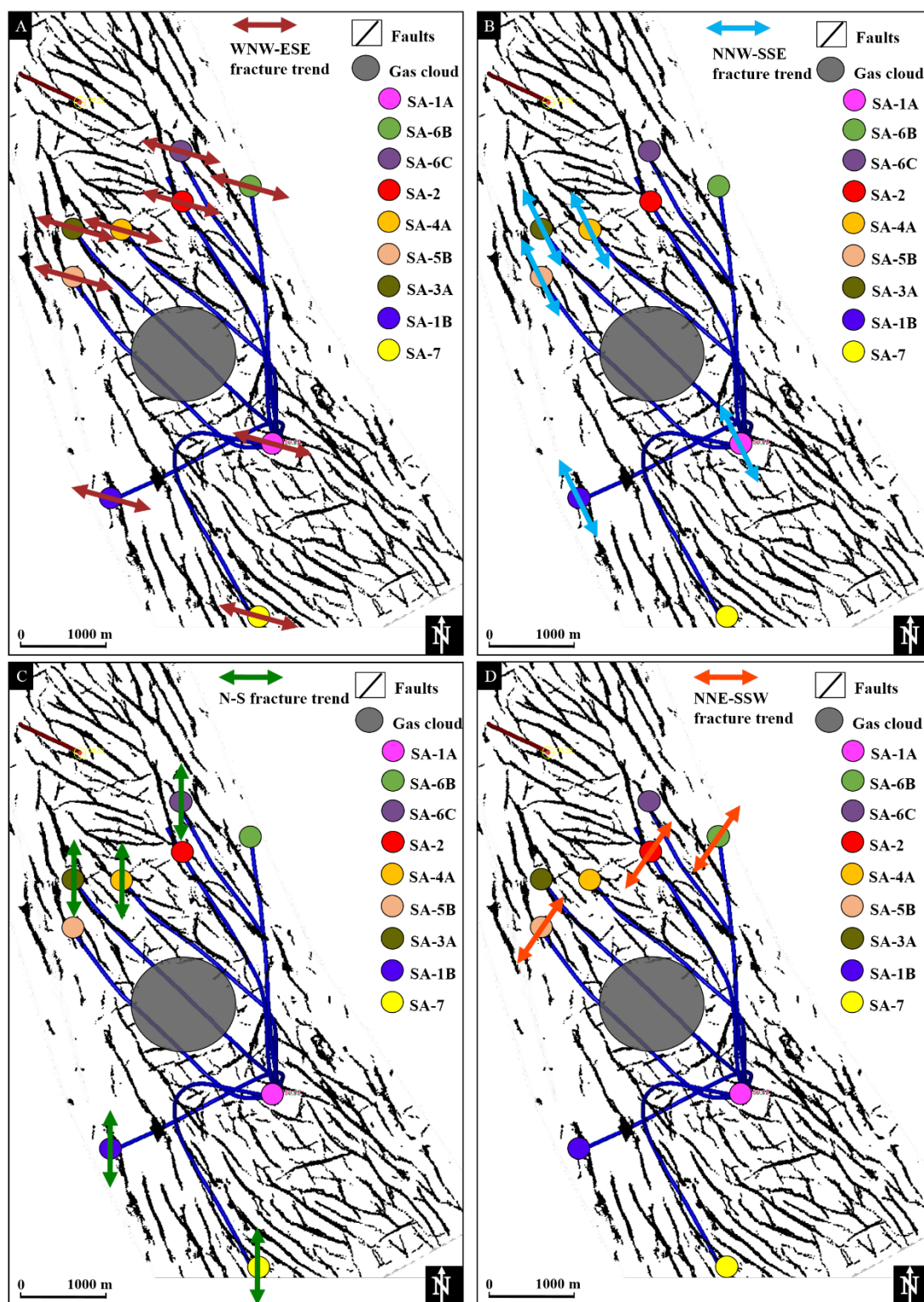


Figure 66 Top Ekofisk surface showing the faults obtained from the ant-tracking algorithm and trajectories of the wells. The wells are marked in different colours at their bottom depth. The arrows on the wells represent the different fracture trends of the corresponding well interpreted from the dip azimuth data. A. Brown arrows represent WNW-ESE fracture trend. B. Blue arrows represent NNW-SSE fracture trend. C. Green arrows represent N-S fracture trend. D. Orange arrows represent NNE-SSE fracture trend.

Table 13 Different fracture trends interpreted from the well azimuth histogram data. The fracture trends are illustrated in Figure 66.

Fracture Trend	Remarks
WNW-ESE	Most dominant fracture trend shown by all wells
NNW-SSE	Present in the well drilled on the eastern shoulder of the structure and absent from the wells drilled on the western shoulder of the structure
N-S	Mostly present in the wells drilled on the eastern shoulder of the structure
NNE-SSW	Present in only in wells drilled to the north of the gas cloud

6.3. Seismic Inversion and Seismic Attributes Study

This section shows the quality of the seismic inversion obtained from the AVO inversion. Thereafter, the Young's Modulus obtained from the seismic AVO inversion is compared with the fault distribution visualized by seismic attributes (Section 6.2.1) and with the well log fracture data.

6.3.1. Seismic Inversion QC

Figure 67 illustrates the upscaled P-impedance and the Young Modulus values based on the AVO inversion and the well log data for the well SA-1A. The inversion data and the log data are in good agreement for both properties in the Ekofisk and Tor formations. The largest mismatch in the Young Modulus between the inversion and the well log data is in the Ekofisk Tight Zone.

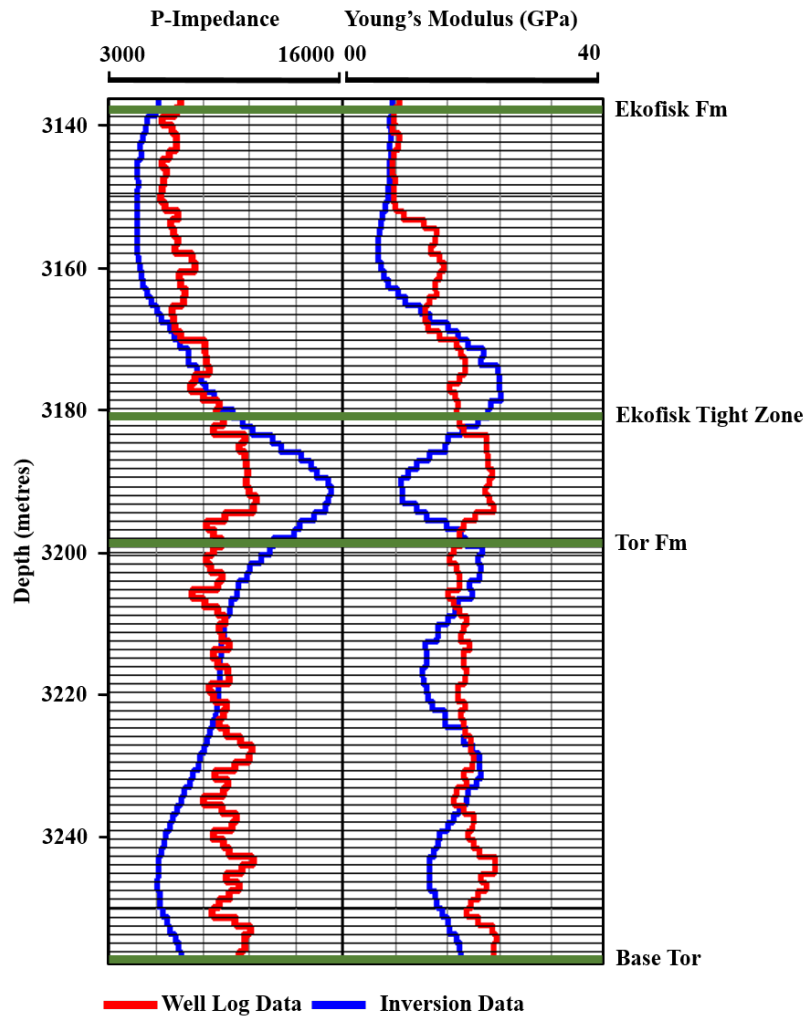


Figure 67 Upscaled P-impedance and Young Modulus, both based on AVO inversion displayed together with the corresponding well log data for well SA-1A. Green lines represent the contacts between the different formations. Note the mismatch in the Young Modulus between the seismic data and the well log data for the Ekofisk Tight Zone. For the location of the well SA-1A, refer to Figure 58.

6.3.2. Comparing Young Modulus and Seismic Attributes

Figure 68-A shows the Ant-tracking and the Young Modulus results on a time-slice within the reservoir area. Figure 68-B shows an enlarged part of the time slice north of the gas cloud. The red arrows show the regions where high Young Modulus correlates with the fault pattern. In both figures, low Young Modulus values (i.e., 0-20 GPa) are displayed in white to highlight the large Young Modulus values predominantly in the vicinity of the faults.

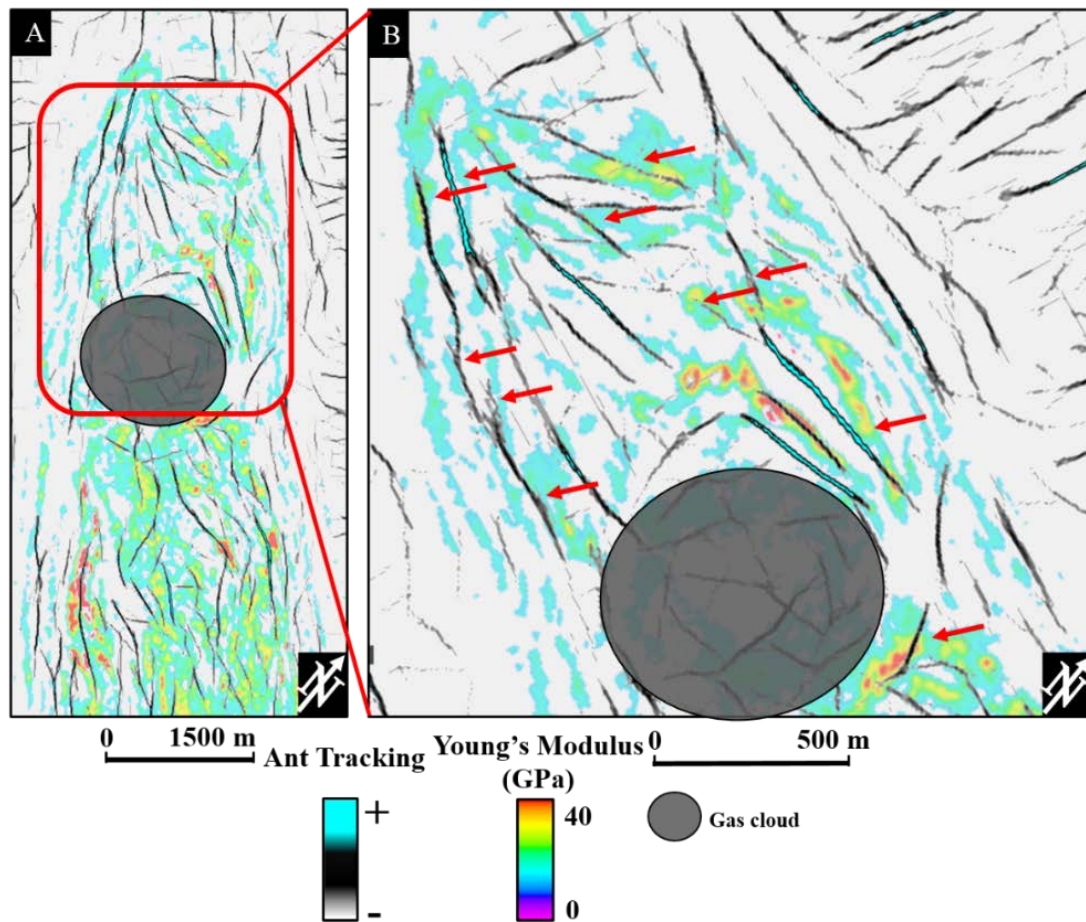


Figure 68 A. Ant-tracking and Young Modulus results illustrated on a time-slice (-2788 ms) inside the reservoir. The red box shows the region displayed in B. B. Magnified image of the Ant-tracking and Young Modulus results illustrating the trend of both datasets in the north of the gas cloud. Red arrows indicate some of the regions where the Young Modulus follows the fault/lineament pattern. The grey area displays the gas cloud. Note that the low Young Modulus values are masked in both figures. Young Modulus values are higher where faults are present.

Figure 61 shows that the variance attribute highlights the major lineament trends in the data. Hence, the variance attribute was also compared with the Young Modulus results. Figure 69 displays both properties on a time-slice within the reservoir area. The figure shows that the high Young Modulus corresponds to the high variance representing the faults. Thus, this result is reiterating the fact that the Young Modulus correlates with the fault pattern from seismic variance.

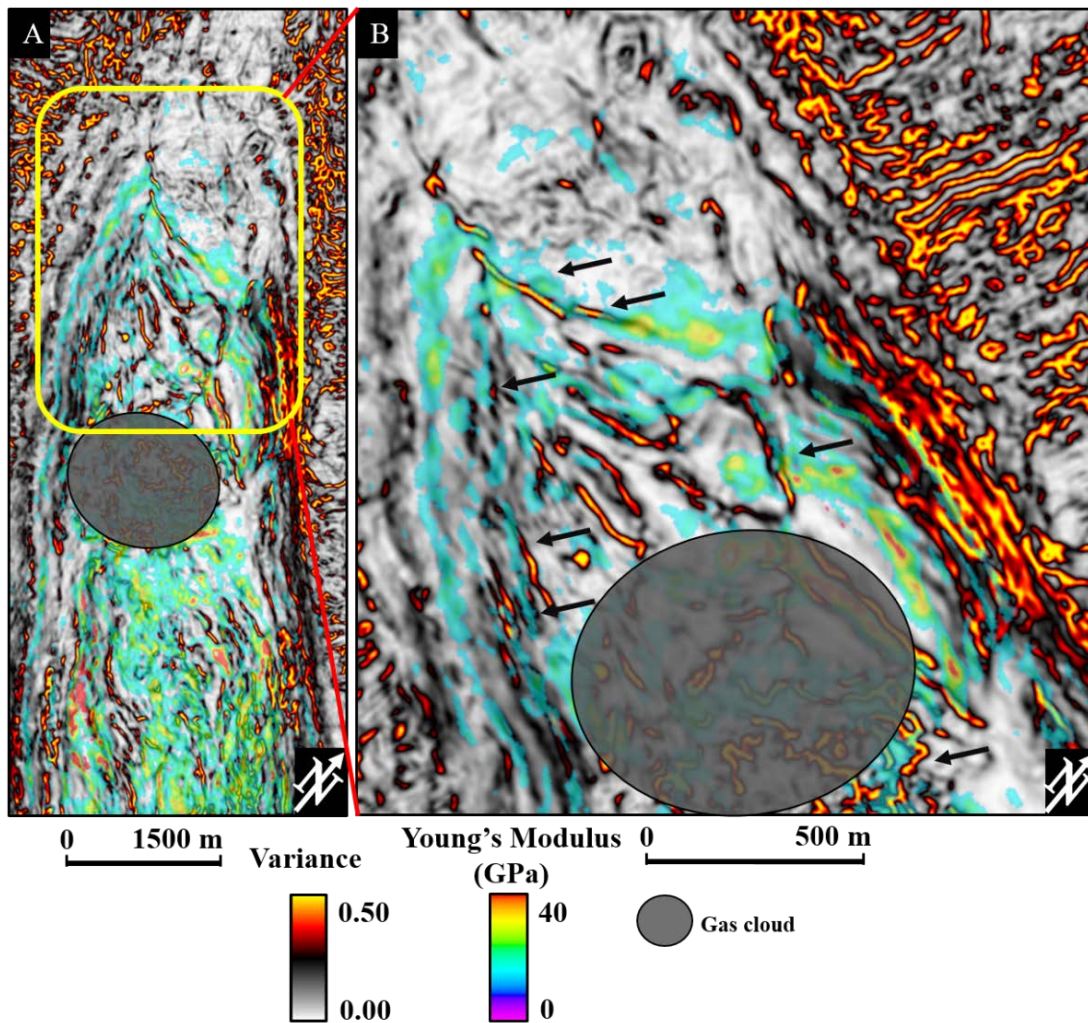


Figure 69 A. Variance and Young Modulus results illustrated on a time-slice (-2788 ms) inside the reservoir. The yellow box shows the region displayed in B. B. Magnified image of the variance and Young Modulus results illustrating the trend of both results to the north of the gas cloud. Black arrows indicate few of the regions where the Young Modulus follows the variance. Note that the low Young Modulus values are masked in both figures.

Figure 70 shows the common display of the t^* attenuation attribute and the Young Modulus on a time-slice within the reservoir. Figure 70-B shows that the trend of both properties is similar to that observed in Figures 68-B and 69-B. However, some mismatches are observed.

In summary Figures 68 to 70 shows that the Young Modulus correlates with the seismic attributes and there exists a relation between the Young Modulus and the seismically detected faults. The presence of fractures in the vicinity of faults (Section 4.1.1) and the observation of high Young Modulus associated with high fracture intensity (Figure 56) suggests in addition that there is a relationship between the Young Modulus, faults and fractures.

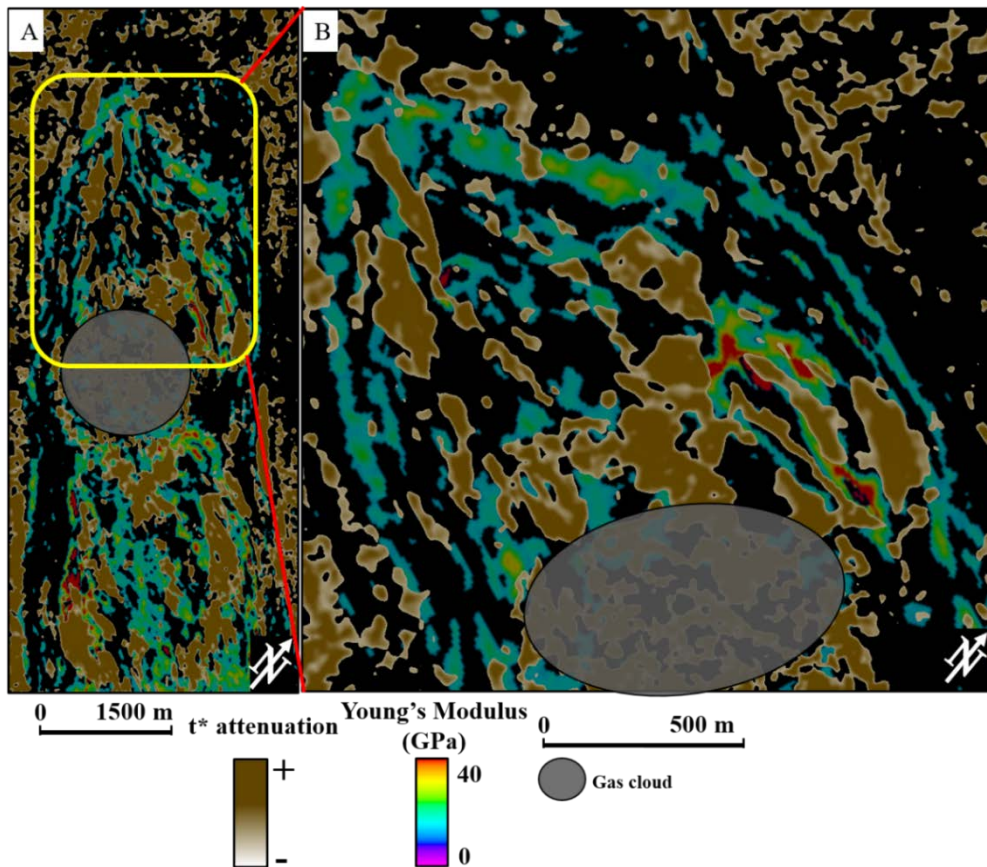


Figure 70 A. t^* attenuation and Young Modulus results illustrated on a time slice (-2788 ms) inside the reservoir. The yellow box shows the region displayed in B. B. Magnified image of the t^* attenuation and Young Modulus results illustrating the trend of both the results on the north of the gas cloud. Note that the low Young Modulus values are masked in both the figures.

Figure 71-A and -B shows the cross-plot of seismic Young Modulus against the variance and t^* attenuation respectively, extracted along the well Rigs-2. The Young Modulus shows a positive correlation with variance (Figure 71-A) and a chaotic correlation with t^* attenuation for negative t^* attenuation values (Figure 71-B). This chaotic correlation could be due to the influence of noise. However, for t^* attenuation values greater than 0, a positive correlation between Young Modulus and t^* attenuation is evident. Similar results were obtained for other wells. The cross-plot of Young modulus against Ant-tracking is not included because Ant-tracking mostly gives information about the position of the faults and does not seem to provide any information about the fault zone covering the fracture area associated to the faults. For the information about the fault fracture zone, the variance attribute is better suited because it shows an amplitude variation across the faults. Following the observations from Figures 68 to 71, the Young Modulus and variance attribute were used for guiding the fracture intensity modelling since both attributes seem to be sensitive to fracture zones.

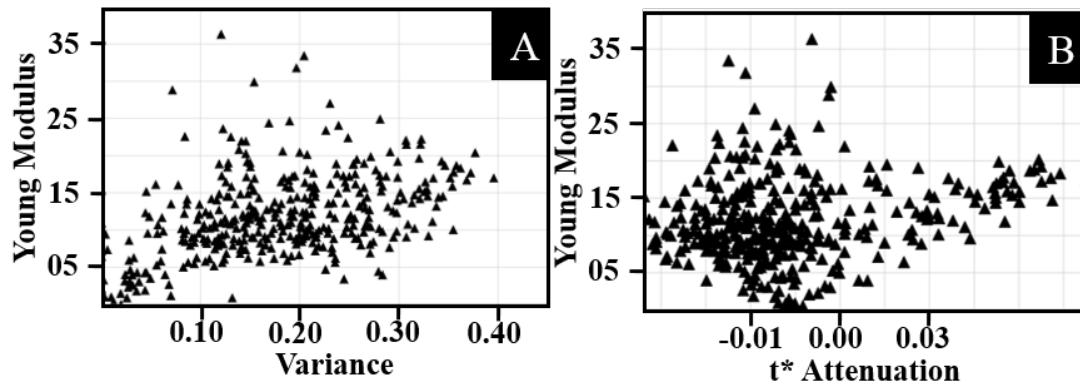


Figure 71 A. Variance versus Young Modulus cross-plot of Rigs-2 well. B. t^* Attenuation versus Young Modulus cross-plot of Rigs-2 well. For the location of the well Rigs-2, refer to Figure 52.

6.4. Fracture Modelling Study

This section consists of two sub-sections. The first one shows a sensitivity analysis of the fracture parameters (Section 5.5.1). This sensitivity study is important to understand the most dominant parameters affecting the fracture permeability. Consequently, the results of this section are used in the fracture modelling of the South Arne Field. The second section discusses modelling parameters used for fracture modelling of the South Arne field and the permeability model obtained from fracture modelling.

6.4.1. Sensitivity Analysis of Fracture Parameters

As discussed in Section 5.5.1, a sensitivity analysis is performed to observe the impact of the critical fracture parameters on the upscaled permeability. The selection of the different parameter values is discussed in Section 5.5.1. Tables 14 and 15 illustrate the change in mean permeability of the upscaled fracture permeability due to the change in fracture concentration and fracture aperture respectively. Similarly, Figures 72 and 73 illustrate the mean upscaled permeability in i direction for different fracture concentrations and fracture apertures respectively. The change in concentration value from 0.5 to 8 (i.e., 16 times) changes the mean upscaled permeability in i direction value from ca 17 mD to ca 275.5 mD. Similarly, while changing the fracture aperture from 0.00075 mm to 0.0012 mm (i.e., 16 times), the mean upscaled permeability in i direction changes from ca 17 mD to ca 69626 mD. The change in mean upscaled permeability for the fracture aperture is significantly higher than the change in mean upscaled permeability for the fracture concentration. To see the effect of concentration and aperture on the permeability in j and k direction, please refer to the Appendix, Section 10.2. No obvious change in the permeability is observed when changing the fracture length from 100 to 500 metres. Unfortunately, higher cases of fracture length are not considered during this study due to the unavailability of superior CPU processing capabilities.

Table 14 Change in mean permeability with change in fracture concentration.

Fracture Concentration	.5	1	2	4	8
Fracture Permeability – i and k direction (mD)	17.02	34.38	68.69	137.07	275.50
Fracture Permeability (j) (mD)	.90	1.83	3.64	7.26	14.64

Table 15 Change in mean permeability with change in fracture aperture.

Fracture Aperture (mm)	.000075	.00015	.0003	.0006	.0012
Fracture Permeability – i and k direction (mD)	17.02	136.09	1088.03	8703.57	69626
Fracture Permeability (j) (mD)	.90	7.21	57.73	461.89	3695.15

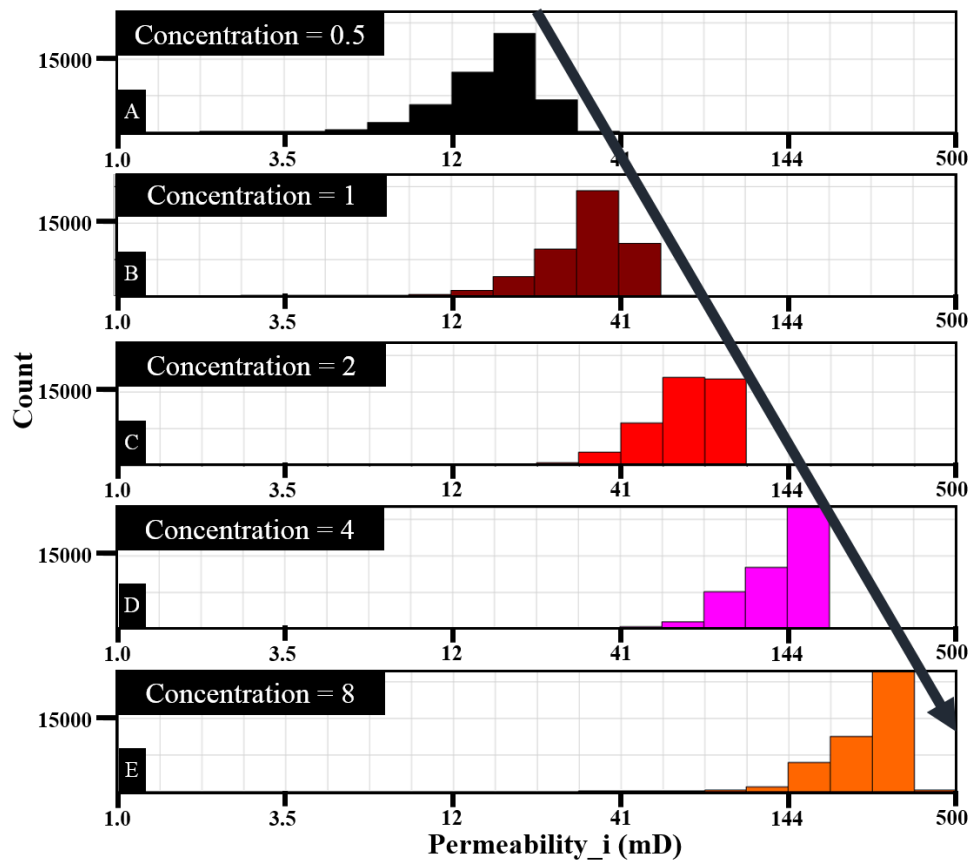


Figure 72 Permeability distribution in i direction for different concentrations, keeping other fracture parameters constant. A, B, C, D and E give the permeabilities for fracture concentration values of 0.5, 1, 2, 4, and 8, respectively. The black arrow highlights the trend of the data.

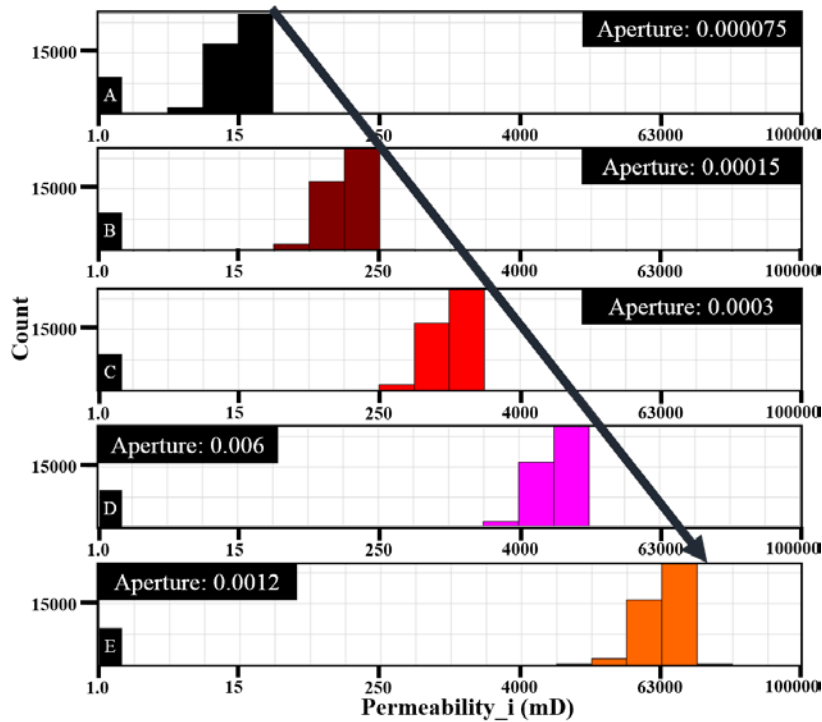


Figure 73 Permeability distribution in *i* direction for different fracture aperture, keeping other fracture parameters constant. A, B, C, D and E give the permeabilities for the aperture value of 0.000075 mm, 0.00015 mm, 0.0003 mm, 0.0006 mm, and 0.0012 mm, respectively. The black arrow highlights the trend of the data

6.4.2. Fracture Modelling of the South Arne Field

6.4.2.1. Modelling Parameters

Derivation of fracture intensity from seismic cubes

As discussed in Section 4.5.1, one of the critical controlling factor in modelling fracture intensity is the variogram model. Typically, the lack of sufficient well data does not allow to derive a reliable variogram range for the two horizontal directions and, in case of strongly deviated wells, the vertical direction. If the fracture intensity is guided by a seismic attribute, this additional variable can be used for deriving the variogram model. Figure 74 shows the modelled variograms from the variance attribute. The variogram does not show a significant anisotropy and consequently the same variogram range was chosen for the two perpendicular horizontal ranges. Also, note that the vertical variogram model (Figure 74-B) is derived from the seismic data as well because of the insufficient fracture data coming from (near-) vertical wells.

Estimating reservoir properties

The fracture dip distribution of the two formations observed in the wells is used as an input for the fracture orientation parameters. Figure 75 shows that most dip angles of the fractures in the Ekofisk and Tor formations lie between 45 to 80 degrees. The dip

angles of the fractures present in the Ekofisk Tight Zone are generally smaller than those of the fractures present in the other two formations.

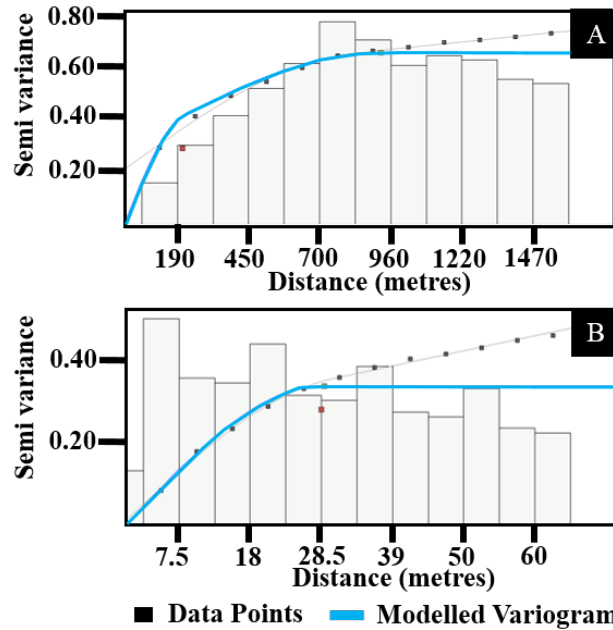


Figure 74 A. Modelled variogram for horizontal direction of the variance attribute (used as the secondary variable). B. Modelled variogram for the vertical direction of the variance attribute.

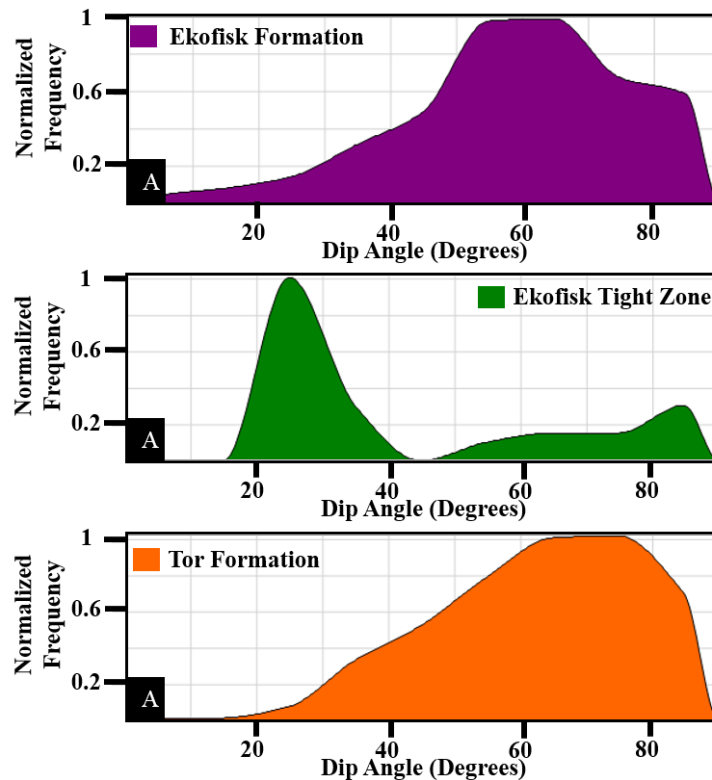


Figure 75 Dip angle distribution of the fractures present in the three formations. Note the low dip angle of fractures present in Ekofisk Tight Zone.

6.4.2.2. Fracture Modelling of the South Arne Field

Figure 76-A, -B and -C illustrate the permeability models resulting from the upscaling of the fracture permeability in i direction of a horizon slice within the Tor Formation. In Figure 76-A, the fracture intensity was calculated by simple kriging of the upscaled intensity of the wells. Figure 76-B and -C shows the permeability resulting from collocated co-kriging of the fracture intensity guided by variance and the Young Modulus respectively. The three models deliver permeability values within the range mentioned in published articles (Luthje et al., 2013). However, the key difference lies in their dynamic behaviour that is guided by the permeability distribution. The permeability model obtained from simple kriging (Figure 76-A) shows a background permeability of ca 10mD and several lineaments in NNW-SSE and WNW-ESE directions with high permeability. Note that these directions reflect the wells fracture azimuth directions used in fracture modelling. On the other hand, the permeability models obtained from the variance seismic attribute (Figure 76-B), and the seismically-derived Young Modulus (Figure 76-C) show areas of high and low permeability that are generally in good agreement with each other.

Figure 76-B shows an area of strongly varying permeability to the south of the gas cloud and in the extreme north of the model. North of the gas cloud there is a large high permeability zone intermingled with few patches of low permeability. These areas of high permeability are in agreement with the trajectories of the horizontal wells, i.e., most of the wells to the north of the gas cloud are drilled horizontally, due to the presence of high permeability zones.

Figure 76-C supports the high permeability zone north of the gas cloud. Similar observations can be made for the permeabilities in j and k directions of all three permeability models. To see the permeability models in j, and k directions, please refer to the Appendix, section 10.3.

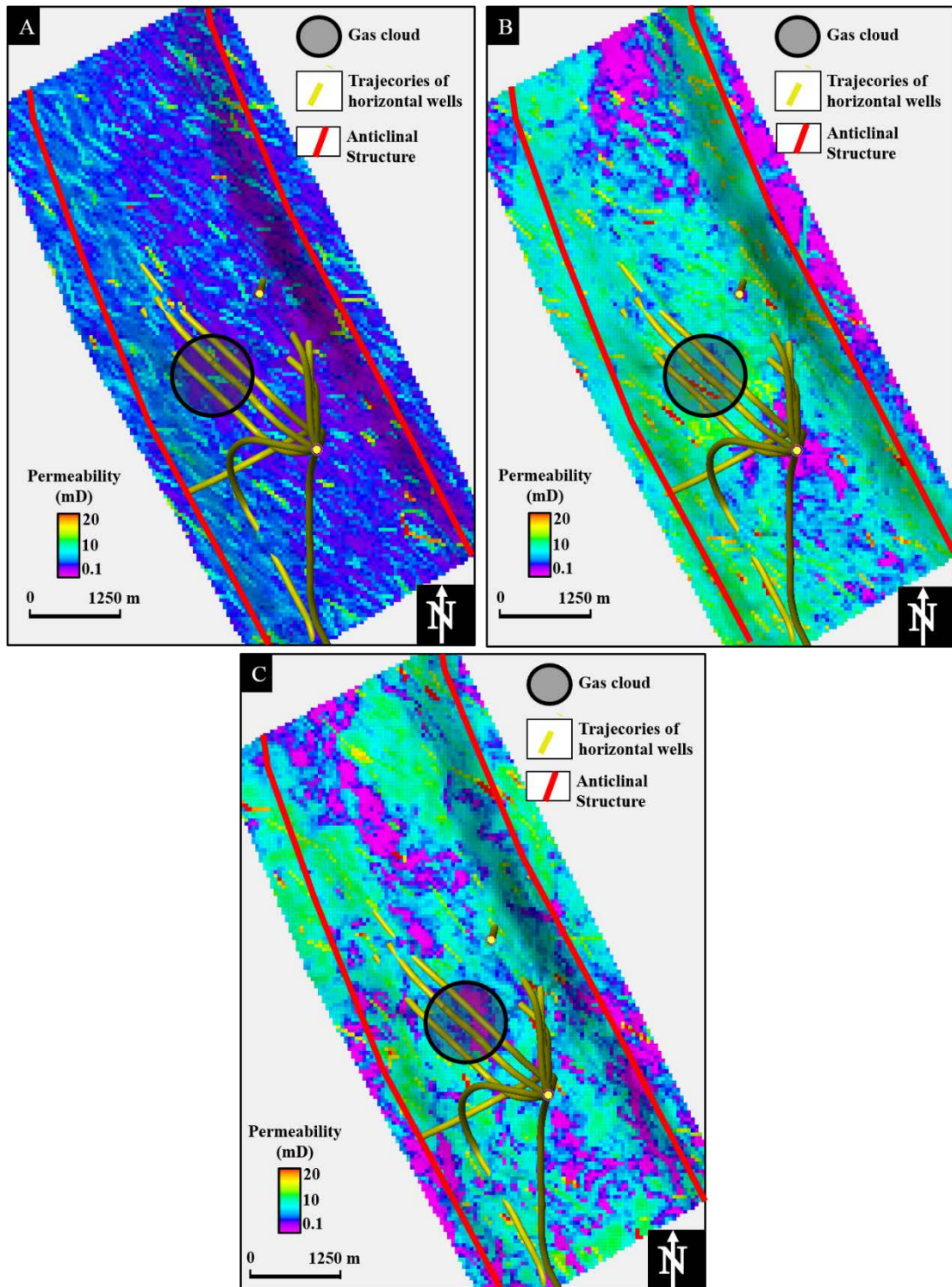


Figure 76 Permeability in *i* direction in the horizontal slice in Tor Formation obtained using the fracture intensity guided by (A) standard statistical procedure, (B) variance attribute, and (C) Young Modulus.

7. DISCUSSION

Rock Physics Study

The cross-plots of different rock physics properties shows that the quality of the reservoir is excellent north of the gas cloud, i.e., in the collapsed region (Figure 53). However, the reservoir quality becomes poorer to the north. The rock physics study (Figures 53 to 56; Tables 8 and 9) also captures the relation of fracture intensity with the reservoir properties. These relations are summarized in Table 16. The two formations (i.e. Ekofisk and Tor Formations) show a similar general trend with respect to the reservoir properties (Figures 54 and 55). However, the clay content of the chalk varies in both formations. Consequently, the Tor Formation has clearly defined zones of clay-rich and clay-poor chalk.

Table 16 Relation of fracture intensity with the reservoir properties.

Fracture Intensity	Type of chalk	Porosity	P-wave Velocity	Young Modulus	Gamma-Ray
High	Clay-poor Chalk	Low	High	High	Low (Brittle)
Low	Clay-rich Chalk	High	Low	Low	High (Ductile)

The occurrence of high fracture intensity in tighter less porous brittle rocks within the reservoir shows that the fractures are present in abundance in clay-poor chalk as compared to clay-rich chalk. This is because pure chalk (i.e., clay-poor chalk) does not show heterogeneity, which could stop fracture development. Hence, pure chalk acts as a single mechanical unit with more fractures confined to these units. Hardman (1982) (Section 2.4.3) and Nelson (2001) (Section 4.3) also discuss this observation of high fracture intensity in clay-poor chalk characterised by low porosity tight reservoir rocks. Mavko (2000) observed the preferential occurrence of fractures in high P- and S-wave velocities characterised by low porosity brittle rocks in fractured carbonates. The association of high fracture intensity with high Young Modulus (Figure 56; Table 16) leads to the idea of using Young Modulus for guiding fracture intensity in fracture modelling.

Fracture Data study

Figure 64 illustrates that the influence of the borehole direction on fracture is negligible. Hence, the well fracture data allows a reliable interpretation of the fracture intensity for each well. To my knowledge, no published study in the past has discussed the well fracture data of the South Arne field in detail. This thesis discusses a unique methodology (Section 5.2.1) for interpreting the fracture trends of each well by plotting the dip azimuth histogram. This methodology was adopted due to the wide distribution

of fracture azimuth data observed in the wells, which is difficult to interpret by the conventional stereo-net plot. However, there is uncertainty in the histogram interpretation due to the bin width. Therefore, the selection of bin width is a critical factor in the histogram. The interpreted fracture trends confirm the different structural trends recognised in previous articles (Astratti et al., 2015; Mackertich and Goulding, 1999).

The lineaments directions documented by seismic attributes (Figures 60 and 61) are in agreement with publishes analyses (Astratti et al., 2015; Mackertich and Goulding, 1999). This confirmation underlines the reliability of the interpreted fracture azimuths from the well data which are compared with the lineaments highlighted by the seismic attributes (Figures 58 and 66). Table 17 illustrates the different lineament trends observed on the well and the seismic data.

Table 17 Observed lineament trends interpreted from the well fracture data and the seismic data.

Lineament Trend	Remarks	
	Well Fracture Data	Seismic Data
NNW-SSE	Present in the wells drilled on the eastern shoulder of the structure and absent from the wells drilled on the western shoulder of the structure	Observed to the north and south of the gas cloud
WNW-ESE	Most dominant structural trend	Most dominant structural trend
NNE-SSW	Present in the wells drilled to the north of the gas cloud	Observed to the south of the gas cloud
ENE-WSW	Not present in the wells	Few lineaments are observed to the south of the gas cloud
N-S	Present in the wells drilled on the eastern and western shoulder of the anticlinal structure, north of the gas cloud and on the western shoulder of the anticlinal structure, south of the gas cloud	Observed only in the eastern shoulder of the anticlinal structure on the ant-tracking cube

Figures 58, 66, and Table 17 illustrate that the WNW-ESE trend is the most dominant trend interpreted within the chalk on both the seismic and the well data. Astratti et al. (2015) also highlight the WNW-ESE trend as the most dominant trend in the seismic data. The absence of the NNW-SSE fracture trend on the western shoulder of the structure is not completely understood. The ENE-WSW lineament trend, interpreted in

seismic data, is not found in the wells. This is because this trend which is present above the reservoir gradually dies out within a few meters in the reservoir (Figure 60). The NNE-SSW and ENE-WSW fracture trends have the same direction as the borehole breakouts. Hence, these fracture trends act as a barrier to the fluid flow as they are formed perpendicular to the maximum horizontal stress direction (Astratti et al., 2015). The N-S trend is observed in most of the wells. However, this trend is not shown on the seismic data except along the eastern shoulder of the reservoir. This could be either due to the small scale of the faults below the seismic resolution or this trend could have been mis-interpreted as the NNW-SSE fracture trend on the seismic data.

Fracture Modelling Study

Seismic attributes and Young Modulus are used to derive the fault pattern based on the assumption that a strong relationship exists between fractures and faults. The seismic attributes (Figures 60 and 61) used in this study deliver consistent results regarding the faults. The fracture modelling workflow used in this study assumes that the fracture density increases near the faults and thus, both are related to each other. A Comparison of the Young Modulus and seismic attributes (i.e., ant-tracking, variance and t^* attenuation) on seismic and well log level (Figures 68 to 71) shows that the Young Modulus correlates best with the variance attribute. The mismatches observed between the Young Modulus and t^* attenuation attribute (Figures 70 and 71) could be explained by the influence of seismic noise on the frequency spectrum which affects the t^* attenuation (Najmuddin, 2004). Frequency modifications related to the layering and multiples may also affect the t^* attenuation attribute. Consequently, the Young Modulus and the variance attribute are used to guide the fracture intensity.

A low Young Modulus is expected at the faults because the fracture zone has an impact on the Young Modulus (Gudmundsson, 2004). However, the Young Modulus seems to correlate with the ant-tracking faults (Figure 68). This is because the seismic resolution does not allow to deliver a detailed Young Modulus distribution via AVO inversion that could show the influence and the fault zone. Additionally, away from the faults, the Young Modulus is no longer influenced by the faults and therefore may show higher values (Figure 68). Thus the Young Modulus expresses the brittleness (and competence of the rock)

Estimating accurate fracture properties is difficult with limited well data. Therefore, analogue studies and the sensitivity analysis study (Section 6.2.2) are used to estimate the fracture properties. Field studies show that fracture length generally follows a power law distribution. Therefore, in this study, all the fracture models incorporate the power law with a shape factor of 2.1 and a length of 25 m. The dominant fracture orientations are derived from the fracture data study (Section 6.2.2). The NNW-SSE and WNW-ESE fracture trends are the fracture orientations at the reservoir level. The sensitivity

analysis shows that the fracture aperture is the critical element influencing the permeability (Section 6.4.1) followed by fracture concentration, and fracture length. This is because of the cubic law (Equation 4) that relates the aperture to the fracture permeability.

The fracture models were compared by analysing their upscaled permeability. The permeability models (Figure 76) deliver a permeability range that is supported by published articles(Luthje et al., 2013). However, the fracture models based on the variance attribute and Young Modulus from the AVO inversion illustrate different connected permeability zones for the same area as compared to the permeability model based on simple kriging. The kriging-based permeability models mimic the fracture trends of the wells, while the seismically based permeability models display a more realistic complexity. It is worthwhile mentioning that the trajectories of the horizontal wells drilled in the South Arne field follow the high-permeability zones identified by the fracture models guided by the variance and by the Young Modulus (Figure 76-B and C). It is understood that the permeability model needs to be calibrated by flow simulation and history matching because. This is beyond the scope of this thesis.

8. CONCLUSION

The fracture data and the fracture modelling study of the South Arne Field reveal several conclusions:

- The fractures in the South Arne field are mainly associated with clay-poor chalk, which has high velocities, low porosities, low shale content, and high Young Modulus. The low shale content and high Young Modulus in the fractured regions confirms that the fractures are associated with more brittle intervals.
- The histogram methodology adopted for identifying the fracture trends from the fracture azimuth data of the wells delivers the different fracture trends on each well. The WNW-ESE fracture trend is the most dominant trend interpreted from the well data. Additionally, the comparison of the fracture trends interpreted from the well data with the lineament trends interpreted from the seismic data gives a more detailed image of the fractures in the South Arne Field.
- Fracture aperture has the most significant influence on the absolute value of the fracture permeability, and fracture intensity controls the spatial distribution of the permeability in the fracture model.
- The models guided by variance attribute and Young Modulus delivers a permeability distribution within the same range of absolute value as delivered by the standard statistical procedure. However, the variance attribute and Young Modulus guided models better represents the connectivity of high permeability zones located near the faults. Yet, the seismic guided fracture modelling requires more control in terms of the spatial permeability distribution. Particularly since the performance of the inversion with few angle-stacks is always questionable, which directly affects the Young Modulus obtained from the inversion.

Further studies are recommended based on reducing the uncertainties around the DFN Model. The main uncertainties in DFN model are the selection of the fracture parameters. Consequently, calibration of the permeability with dynamic data (i.e., production data) would reduce these uncertainties. This process of calibration is generally empirical where the values of the fracture parameters are varied to observe the effect on the permeability and simulated production.

9. REFERENCES

- Abul Khair, H., Cooke, D., Backé, G., King, R., Hand, M., Tingay, M., and Holford, S., 2012, Subsurface mapping of natural fracture networks; a major challenge to be solved. Case study from the shale intervals in the Cooper Basin, South Australia.
- Ahmed Elfeel, M., 2014, Improved upscaling and reservoir simulation of enhanced oil recovery processes in naturally fractured reservoirs: Heriot-Watt University.
- Aki, K., and Richards, P., 1980, Quantitative Seismology, Theory and Methods, Vol. 1 WH Freeman & Co: New York.
- Al-anazi, B. D., Algarni, M. T., Tale, M., and Almushiqeh, I., 2011, Prediction of Poisson's Ratio and Young's Modulus for Hydrocarbon Reservoirs Using Alternating Conditional Expectation Algorithm, Society of Petroleum Engineers.
- Al-Baldawi, B., 2015, Building A 3D Geological model Using Petrel Software for Asmari Reservoir, South Eastern Iraq, 1750-1762 p.:
- Altimar, R. P., 2013, Brittleness estimation from seismic measurements in unconventional reservoirs: Application to the Barnett Shale, The University of Oklahoma.
- Andsbjerg, J., and Dybkjær, K., 2003, Sequence stratigraphy of the Jurassic of the Danish Central Graben: The Jurassic of Denmark and Greenland. Geological Survey of Denmark and Greenland Bulletin, v. 1, p. 265-300.
- Angerer, E., Lanfranchi, P., Pharez, S., and Rogers, S., 2004, Integrated approach for seismic fracture characterisation for improved reservoir performance, Abu Dhabi International Conference and Exhibition: Abu Dhabi, United Arab Emirates, Society of Petroleum Engineers.
- Araujo, H., Lacentre, P., Zapata, T., Del Monte, A., Dzelalija, F., Gilman, J., Meng, H.-Z., Kazemi, H., and Ozkan, E., 2004, Dynamic Behavior of Discrete Fracture Network (DFN) Models, SPE International Petroleum Conference in Mexico: Puebla Pue., Mexico, Society of Petroleum Engineers.
- Astratti, D., Aarre, V., Vejbæk, O. V., and White, G., 2015, Mapping and time-lapse analysis of South Arne Chalk fault network using new developments in seismic dip computation: Geological Society, London, Special Publications, v. 406, no. 1, p. 331-358.
- Azevedo, L., and Soares, A., 2017, Geostatistical Methods for Reservoir Geophysics, Cham, Cham : Springer, Advances in Oil and Gas Exploration and Production Ser.
- Baba, K., Bahi, L., and Ouadif, L., 2014, Geostatistical Analysis for delineating sterile inclusions in Sidi Chennane'phosphatic series, Morocco: Earth Sciences Research Journal, v. 18, no. 2, p. 143-148.
- Birgé, L., and Rozenholc, Y., 2006, How many bins should be put in a regular histogram: ESAIM: Probability and Statistics, v. 10, p. 24-45.
- Bishop, D. J., 1996, Regional distribution and geometry of salt diapirs and supra-Zechstein Group faults in the western and central North Sea: Marine and Petroleum Geology, v. 13, no. 4, p. 355-364.
- Bohling, G., 2005, Introduction to geostatistics and variogram analysis: Kansas geological survey, v. 1, p. 1-20.

- Booth, A. D., Emir, E., and Diez, A., 2015, Approximations to seismic AVA responses: Validity and potential in glaciological applications: *Geophysics*, v. 81, no. 1, p. WA1-WA11.
- Bratton, T., Canh, D. V., Van Que, N., Duc, N. V., Gillespie, P., Hunt, D., Li, B., Marcinew, R., Ray, S., and Montaron, B., 2006, The nature of naturally fractured reservoirs: *Oilfield Review*, v. 18, no. 2, p. 4-23.
- Buller, A., Berg, E., Hjelmeland, O., Kleppe, J., Torsaeter, O., and Aasen, J., 1990, *North Sea oil and gas reservoirs II: Graham and Trotman*, London, v. 234237.
- Butt, A., 2012, Compaction and evolution of rock properties and rock physics diagnostics of Albatross discovery, SW Barents Sea.
- Chopra, S., and Marfurt, K. J., 2007, *Seismic attributes for prospect identification and reservoir characterization*, Society of Exploration Geophysicists Tulsa, Oklahoma.
- Christensen, S. A., Ebbe-Dalgaard, T. J., Rosendal, A., Christensen, J. W., Robinson, G. C., Zellou, A. M., and royer, t., 2006, *Seismically Driven Reservoir Characterization Using an Innovative Integrated Approach: Syd Arne Field*, Society of Petroleum Engineers.
- Contreras, A., Torres-Verdín, C., and Fasnacht, T., 2006, Sensitivity analysis of data-related factors controlling AVA simultaneous inversion of partially stacked seismic amplitude data: Application to deepwater hydrocarbon reservoirs in the central Gulf of Mexico: *Geophysics*, v. 72, no. 1, p. C19-C29.
- Correia, M., Maschio, C., Schiozer, D. J., and Santos, M., *Upscaling Technique Applied to Naturally Fractured Carbonate Reservoirs*, in *Proceedings Brasil Offshore2011*, Society of Petroleum Engineers.
- Cui, X., Lines, L., Krebes, E. S., and Peng, S., 2015, *Seismic Forward Modeling of Fractures and Fractured Medium Inversion*, Springer.
- de Vries, N. G., 2014, *Petroleum System Analysis of the Chalk Fields in the Danish and Dutch Sector of the Central Graben, North Sea*: NTNU.
- Decroux, B., and Gosselin, O., 2013, *Computation of Effective Dynamic Properties of Naturally Fractured Reservoirs: Comparison and Validation of Methods*, EAGE Annual Conference & Exhibition incorporating SPE Europec: London, UK, Society of Petroleum Engineers.
- Dershowitz, W., La Pointe, P., and Doe, T., *Advances in discrete fracture network modeling*, in *Proceedings Proceedings of the US EPA/NGWA fractured rock conference, Portland2004*, p. 882-894.
- Dershowitz, W. S., and Herda, H. H., *Interpretation of fracture spacing and intensity*, in *Proceedings The 33th US Symposium on Rock Mechanics (USRMS)1992*, American Rock Mechanics Association.
- Dunn, D. E., LaFountain, L. J., and Jackson, R. E., 1973, Porosity dependence and mechanism of brittle fracture in sandstones: *Journal of Geophysical Research*, v. 78, no. 14, p. 2403-2417.
- Emsley, S., Chi, S., Hallin, J., and Rivas, J., 2014, *Generation of a Realistic Discrete Fracture Network Model using Deterministic Input Data Derived from 3D Multicomponent Seismic Amplitude Data*, Society of Exploration Geophysicists.

- Fatti, J. L., Smith, G. C., Vail, P. J., Strauss, P. J., and Levitt, P. R., 1994, Detection of gas in sandstone reservoirs using AVO analysis: A 3-D seismic case history using the Geostack technique: *Geophysics*, v. 59, no. 9, p. 1362-1376.
- Francis, A., 2014, A simple guide to seismic inversion: *GEOExPro*, v. 10, no. 2, p. 46-50.
- Ganssle, G., 2012, Calculation of a Synthetic Gather using the Aki-Richards Approximation to the Zoeppritz Equations.
- Garcia, A., and MacBeth, C., 2013, An estimation method for effective stress changes in a reservoir from 4D seismic data: *Geophysical Prospecting*, v. 61, no. 4, p. 803-816.
- Gautier, D. L., 2005, Kimmeridgian shales total petroleum system of the North Sea graben province: Geological Survey (US).
- Geir U. Haugen, M. A. S., 2000, The echo of a fault or fracture: *Geophysics*, v. 65, no. 1, p. 176-189.
- Gennaro, M., 2011, The chalk depositional system in the Central Graben—concepts of regional geology, sedimentology and stratigraphy: 3D seismic stratigraphy and reservoir characterization of the Chalk Group in the Norwegian Central Graben, North Sea.
- Golyan, M. F., 2012, Compaction, rock property evolution and rock physics diagnostics of Askeladd discovery, Norwegian Barents Sea.
- Gommesen, L., Fabricius, I. L., Mukerji, T., Mavko, G., and Pedersen, J. M., 2007, Elastic behaviour of North Sea chalk: A well-log study: *Geophysical Prospecting*, v. 55, no. 3, p. 307-322.
- Gudmundsson, A., 2004, Effects of Young's modulus on fault displacement: *Comptes Rendus Geoscience*, v. 336, no. 1, p. 85-92.
- Halland, E. K., Gjeldvik, I., Johansen, W., Magnus, C., Meling, I., Pedersen, S., Riis, F., Solbakk, T., and Tappel, I., 2011, CO2 Storage Atlas Norwegian North Sea: Norwegian Petroleum Directorate, PO Box, v. 600.
- Hardman, R., 1982, Chalk reservoirs of the North Sea: *Bulletin of the Geological Society of Denmark*, v. 30, no. 3-4, p. 119-137.
- Hassanpour, R., and Deutsch, C. V., 2010, An introduction to grid-free object-based facies modeling: Centre for computational geostatistics report, v. 12.
- Herwanger, J., Mohamed, F., Newman, R., and Vejbæk, O., 2013, Time-lapse seismic data-calibrated geomechanical model reveals hydraulic fracture re-orientation, SEG Technical Program Expanded Abstracts 2013, Society of Exploration Geophysicists, p. 4949-4953.
- Herwanger, J., Schjøtt, C., Frederiksen, R., Vejbæk, O., Wold, R., Hansen, H., Palmer, E., and Koutsabeloulis, N., Applying time-lapse seismic methods to reservoir management and field development planning at South Arne, Danish North Sea, *in Proceedings Geological Society, London, Petroleum Geology Conference series 2010, Volume 7, Geological Society of London*, p. 523-535.
- Isaksen, D., and Tonstad, K., 1989, A revised Cretaceous and Tertiary lithostratigraphic nomenclature for the Norwegian North Sea, Norwegian Petroleum Directorate.
- Japsen, P., Britze, P., and Andersen, C., 2003, Upper Jurassic–Lower Cretaceous of the Danish Central Graben: structural framework and nomenclature: The Jurassic of Denmark and Greenland. Geological Survey of Denmark and Greenland Bulletin, v. 1, p. 233-246.

- Javed, M. A., 2012, Late Carboniferous-Early Permian structural development of the Ringkøbing-Fyn High and adjacent Norwegian-Danish Basin: University of Oslo.
- Kennedy, W., 1987, Late Cretaceous and early Palaeocene Chalk Group sedimentation in the Greater Ekofisk area, North Sea central graben: *Bulletin des Centres de Recherches Exploration-Production Elf-Aquitaine*, v. 11, no. 1, p. 91-126.
- King, M. J., MacDonald, D. G., Todd, S. P., and Leung, H., 1998, Application of Novel Upscaling Approaches to the Magnus and Andrew Reservoirs, European Petroleum Conference: The Hague, Netherlands, Society of Petroleum Engineers.
- Lei, Q., Latham, J.-P., and Tsang, C.-F., 2017, The use of discrete fracture networks for modelling coupled geomechanical and hydrological behaviour of fractured rocks: *Computers and Geotechnics*, v. 85, p. 151-176.
- Lindgreen, H., Fallick, A. E., Jakobsen, F., and Springer, N., 2012, The Tight Danian Ekofisk Chalk Reservoir formation in the South Arne Field, North Sea: Mineralogy and Porosity: *Journal of Petroleum Geology*, v. 35, no. 3, p. 291-309.
- Luthje, M., Stokkendal, J., Lindelow-Marsden, C. C., Johansen, K., and Jensen, L. J. K., 2013, Using 4D Seismic to Validate the Geomodel for the South Arne Chalk Field, Society of Petroleum Engineers.
- Ma, X.-Q., 2002, Simultaneous inversion of prestack seismic data for rock properties using simulated annealing: *Geophysics*, v. 67, no. 6, p. 1877-1885.
- Mackertich, D. S., and Goulding, D. R. G., 1999, Exploration and appraisal of the South Arne Field, Danish North Sea: Geological Society, London, Petroleum Geology Conference series, v. 5, no. 1, p. 959-974.
- Mavko, G., 2000, Multi-Attribute Seismic/Rock Physics Approach to Characterizing Fractured Reservoirs: Stanford University (US).
- McCann, T., The geology of central Europe 2008, Geological Society of London.
- Møller, J. J., and Rasmussen, E. S., 2003, Middle Jurassic–Early Cretaceous rifting of the Danish Central Graben: The Jurassic of Denmark and Greenland. Geological Survey of Denmark and Greenland Bulletin, v. 1, p. 247-264.
- Najmuddin, I., 2001, Detecting fracture zones in the Austin chalk using seismic P-wave data.
- Najmuddin, I. J., 2004, Austin Chalk fracture mapping using frequency data derived from seismic data: Texas A&M University.
- Nelson, R., 2001, Geologic analysis of naturally fractured reservoirs, Gulf Professional Publishing.
- Paillet, F. L., and Kapucu, K., 1989, Fracture characterization and fracture-permeability estimates from geophysical logs in the Mirror Lake watershed, New Hampshire, Department of the Interior, US Geological Survey, v. 4058.
- Pedersen, S. I., Skov, T., Randen, T., and Sønneland, L., 2005, Automatic fault extraction using artificial ants, *Mathematical Methods and Modelling in Hydrocarbon Exploration and Production*, Springer, p. 107-116.
- Pendrel, J., and Van Riel, P., 2000, Effect of well control on constrained sparse spike seismic inversion: *CSEG Recorder*, v. 25, p. 18-26.
- Pereira, L. A. G. R., 2009, Seismic attributes in hydrocarbon reservoirs characterization: Universidade de Aveiro.

- Price, N. J., and Cosgrove, J. W., 1990, *Analysis of geological structures*, Cambridge University Press.
- Randen, T., Pedersen, S. I., and Sønneland, L., Automatic extraction of fault surfaces from three-dimensional seismic data, *in* Proceedings 2001 SEG Annual Meeting 2001, Society of Exploration Geophysicists.
- Ringrose, P., and Bentley, M., 2015, *Reservoir model types*, Reservoir Model Design, Springer, p. 173-231.
- Rocha, M. M., Yamamoto, J. K., Watanabe, J., and Fonseca, P. P., 2012, Studying the influence of a secondary variable in Collocated Cokriging estimates: *Anais da Academia Brasileira de Ciências*, v. 84, no. 2, p. 335-346.
- Sams, M., and Saussus, D., Practical implications of low frequency model selection on quantitative interpretation results, *in* Proceedings 2013 SEG Annual Meeting 2013, Society of Exploration Geophysicists.
- Schlumberger, L., 2010, *Petrel 2010 : Petrel introduction G & G course*, Schlumberger.
- Simm, R., and Bacon, M., 2014, *Seismic Amplitude: An interpreter's handbook*, Cambridge University Press.
- Singhal, B., and Gupta, R., 2010, *Fractures and discontinuities*, Applied Hydrogeology of Fractured Rocks, Springer, p. 13-33.
- Stearns, D. W., and Friedman, M., 1972, *Reservoirs in fractured rock: Geologic exploration methods*.
- Taner, M. T., 2001, *Seismic attributes: CSEG recorder*, v. 26, no. 7, p. 49-56.
- Tavakkoli, M., Mohammadsadeghi, M., Shahrabadi, A., Khajooee, S., Malakooti, R., and Beidokhti, M. S., 2009, Deterministic versus Stochastic Discrete Fracture Network (DFN) Modeling, Application in a Heterogeneous Naturally Fractured Reservoir, Kuwait International Petroleum Conference and Exhibition: Kuwait City, Kuwait, Society of Petroleum Engineers.
- Terzaghi, R. D., 1965, Sources of error in joint surveys: *Geotechnique*, v. 15, no. 3, p. 287-304.
- Trice, R., 2014, *Basement exploration, West of Shetlands: progress in opening a new play on the UKCS*: Geological Society, London, Special Publications, v. 397, no. 1, p. 81-105.
- Twiss, R. J., and Moores, E. M., 1992, *Structural geology*, Macmillan.
- Van Golf-Racht, T. D., 1982, *Fundamentals of fractured reservoir engineering*, Elsevier.
- Vejbæk, O., and Andersen, C., 2002, Post mid-Cretaceous inversion tectonics in the Danish Central Graben—regionally synchronous tectonic events: *Bulletin of the Geological Society of Denmark*, v. 49, no. 2, p. 93-204.
- Vejbæk, O. V., Mohamed, F. R., and Herwanger, J., 2014, 4D seismic, 4D geomechanics and hydraulic stimulation in the low permeability South Arne chalk field, 139-148 p.:
- Xu, H., Zhou, W., Xie, R., Da, L., Xiao, C., Shan, Y., and Zhang, H., 2016, Characterization of rock mechanical properties using lab tests and numerical interpretation model of well logs: *Mathematical Problems in Engineering*, v. 2016.

10. APPENDIX

10.1. Fracture Data

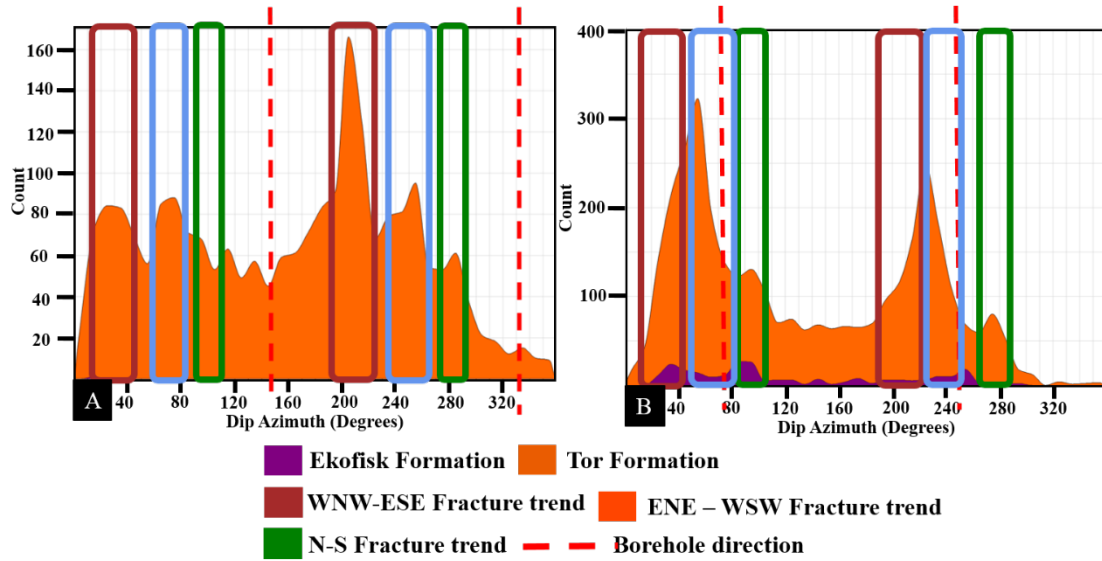


Figure 77 A. Dip azimuth histogram of fracture data for the well SA-3A illustrating interpreted fracture trends. B. Dip azimuth histogram of fracture data for the well SA-1B illustrating interpreted fracture trends. For the location of the wells, refer to Figure 58.

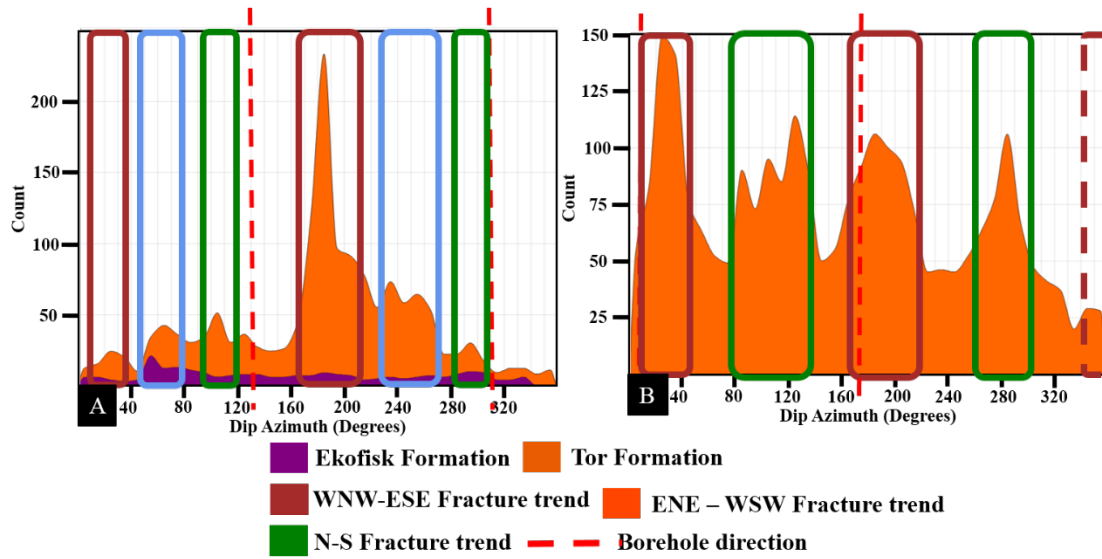


Figure 78 A. Dip azimuth histogram of fracture data for the well SA-4A illustrating interpreted fracture trends. B. Dip azimuth histogram of fracture data for the well SA-6C illustrating interpreted fracture trends. For the location of the wells, refer to Figure 58.

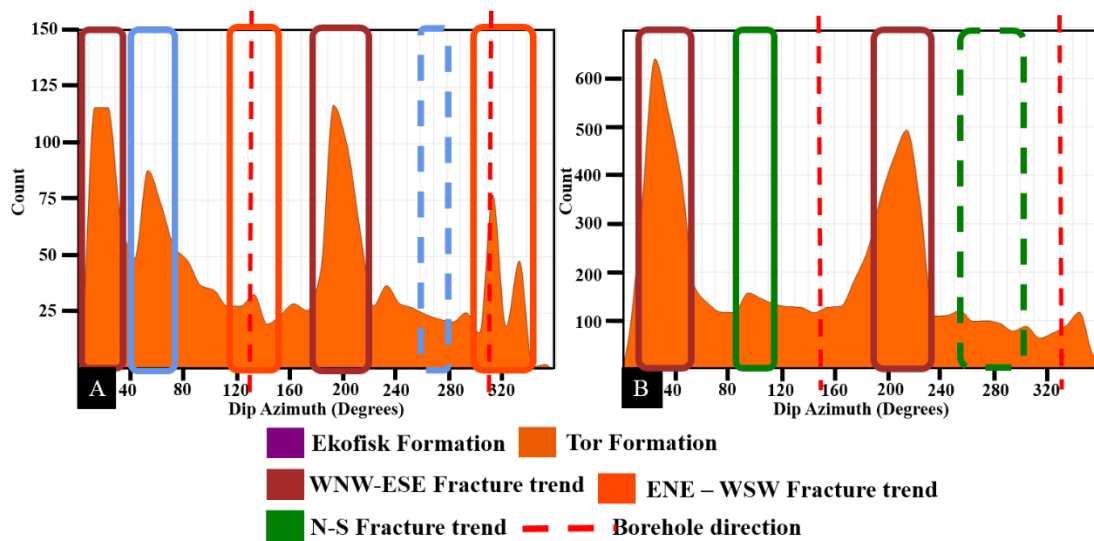


Figure 79 A. Dip azimuth histogram of fracture data for the well SA-5B illustrating interpreted fracture trends. B. Dip azimuth histogram of fracture data for the well SA-7 illustrating interpreted fracture trends. For the location of the wells, refer to Figure 58.

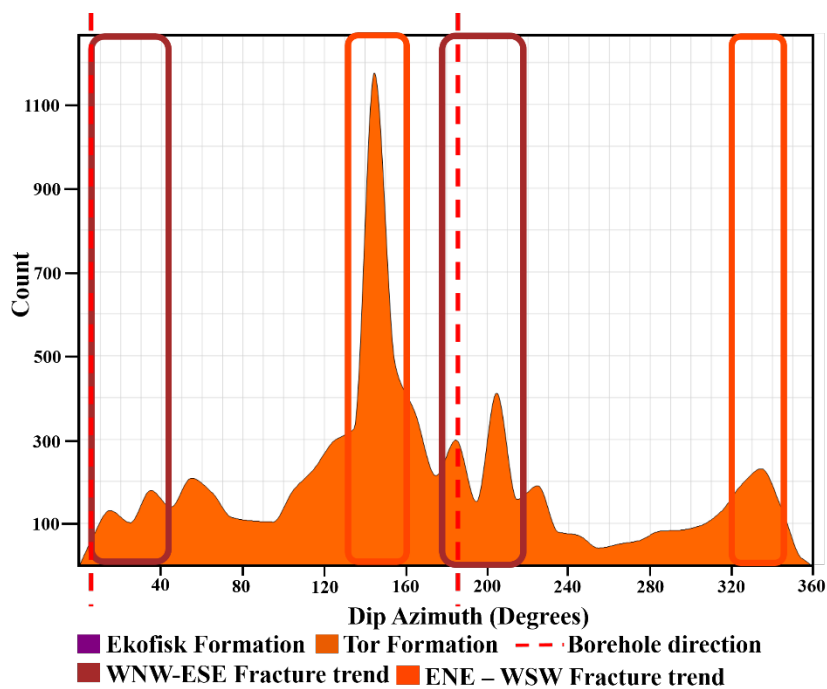


Figure 80 Dip azimuth histogram of fracture data for the well SA-6B illustrating interpreted fracture trends. Brown rectangle indicates the WNW-ESE fracture trend, while orange colour indicates the NNE-SSW fracture trend. Red dash line indicates the borehole azimuth. For the location of the well SA-6B, refer to Figure 58.

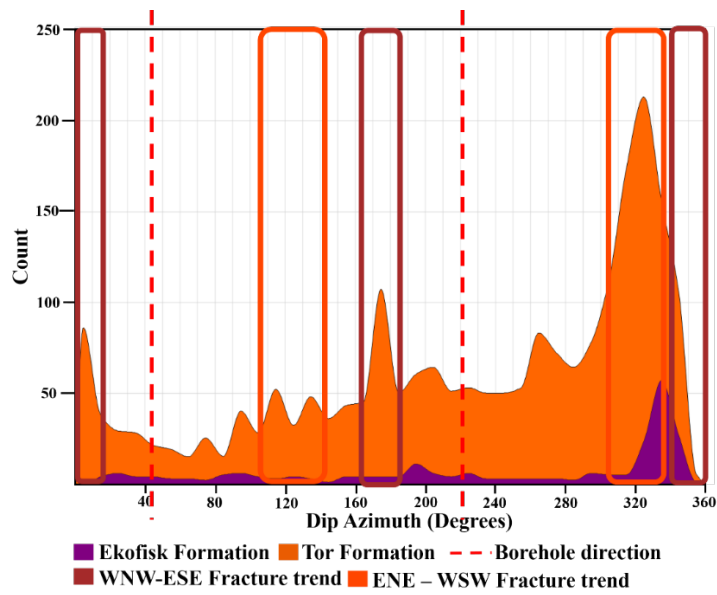


Figure 81 Dip azimuth histogram of fracture data for the well SA-2 illustrating interpreted fracture trends. Brown rectangle indicates the WNW-ESE fracture trend, while orange colour indicates the NNE-SSW fracture trend. Red dash line indicates the borehole azimuth. For the location of the well SA-2, refer to Figure 58.

10.2. Impact of fracture concentration and fracture aperture on fracture permeability

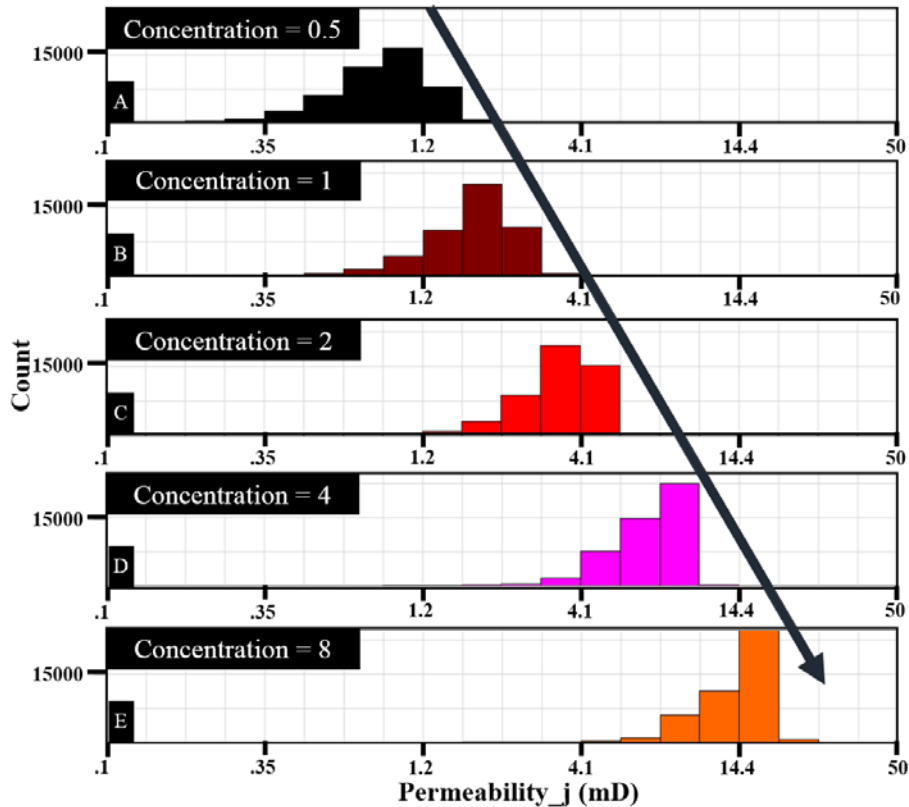


Figure 82 Change in permeability in *j* direction with the change in concentration, keeping other parameters constant. A, B, C, D and E define the concentration value at 0.5, 1, 2, 4, and 8, respectively.

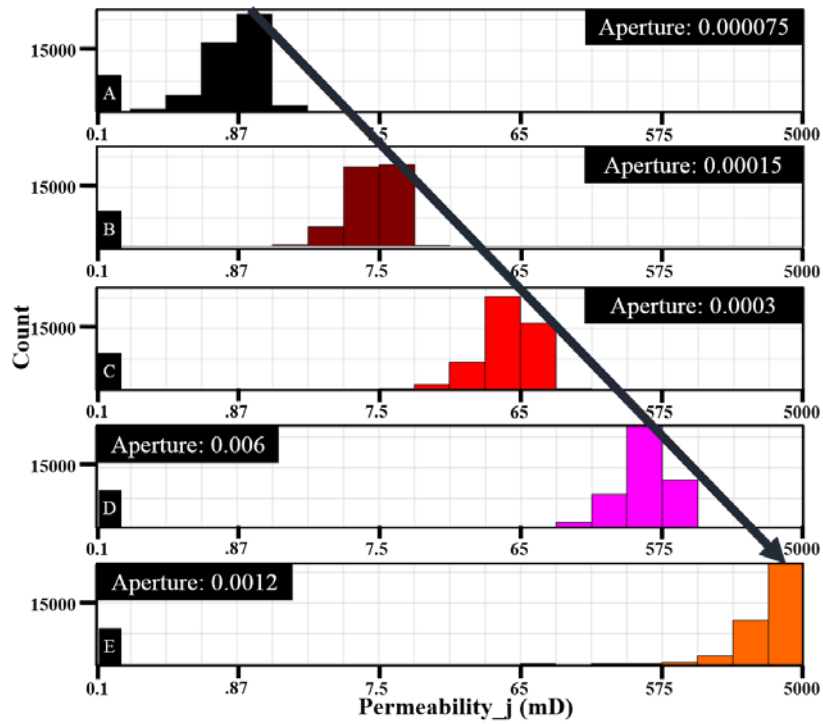


Figure 83 Change in permeability in j direction with the change in aperture, keeping other parameters constant. A, B, C, D and E define the aperture value at 0.000075 mm, 0.00015 mm, 0.0003 mm, 0.0006 mm, and 0.0012 mm, respectively.

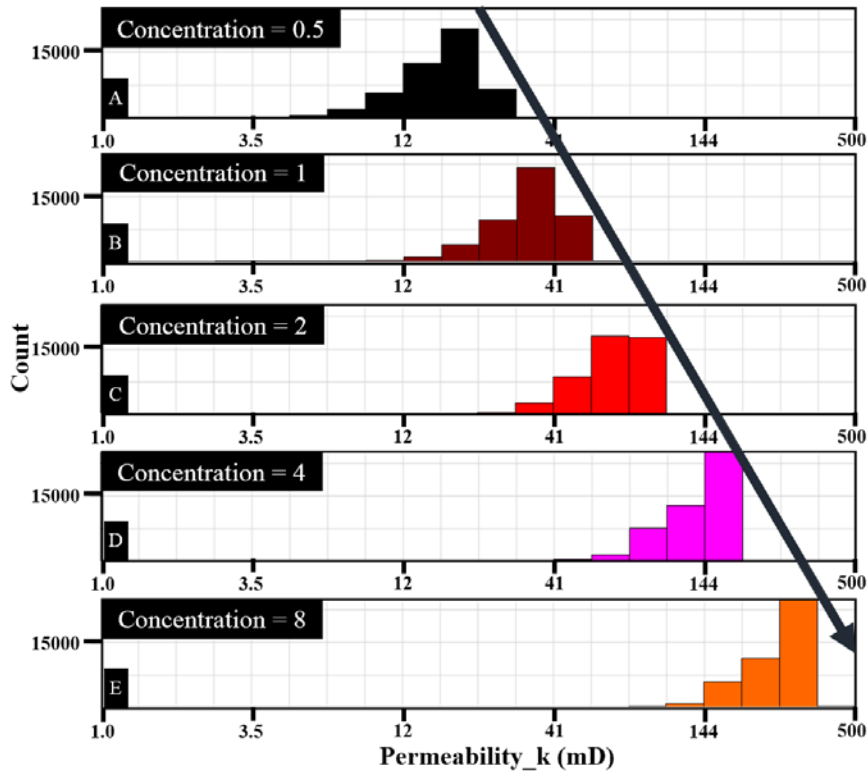


Figure 84 Change in permeability in k direction with the change in concentration, keeping other parameters constant. A, B, C, D and E define the concentration value at 0.5, 1, 2, 4, and 8, respectively.

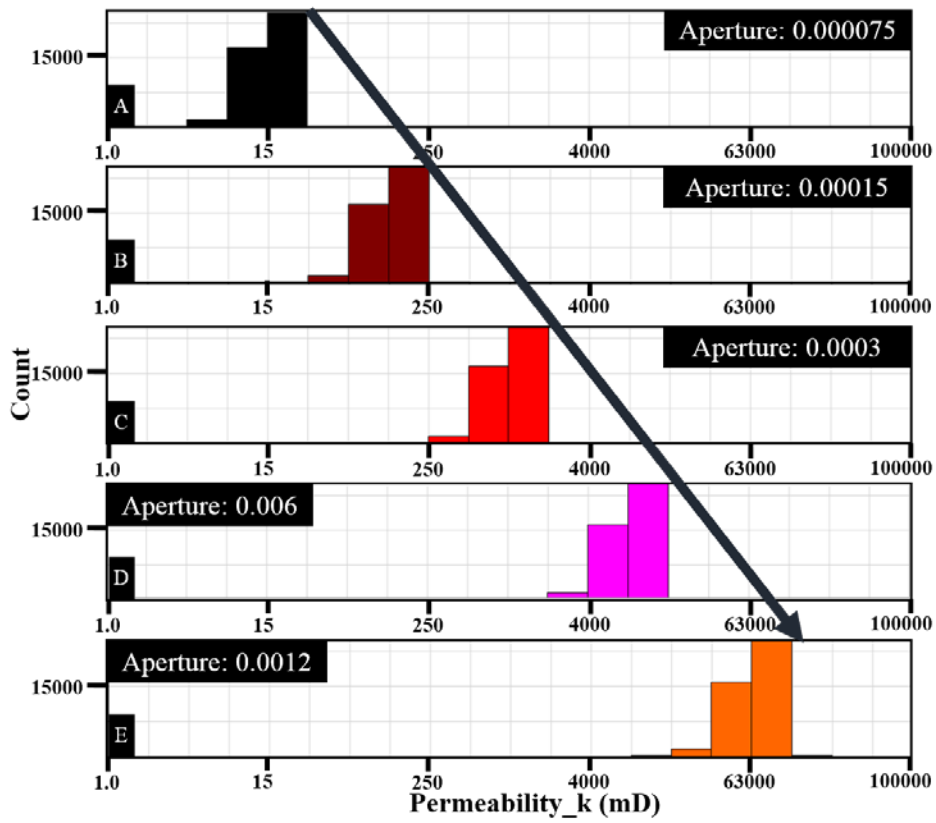


Figure 85 Change in permeability in k direction with the change in aperture, keeping other parameters constant. A, B, C, D and E define the aperture value at 0.000075 mm, 0.00015 mm, 0.0003 mm, 0.0006 mm, and 0.0012 mm, respectively.

10.3. Fracture Modelling

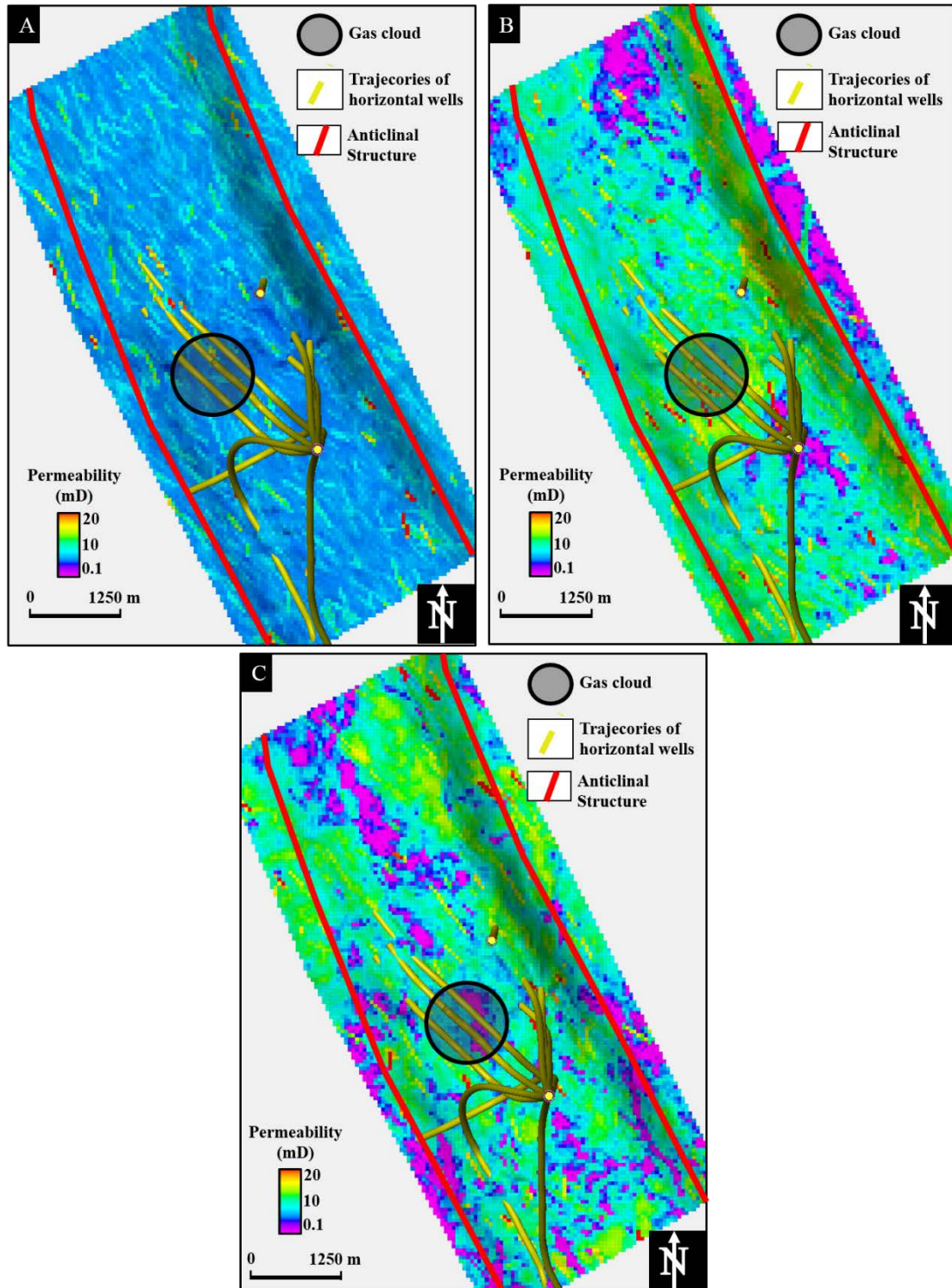


Figure 86 Permeability in *j* direction in the horizontal slice in Tor Formation obtained using the fracture intensity guided by (A) standard statistical procedure, (B) variance attribute, and (C) Young Modulus.

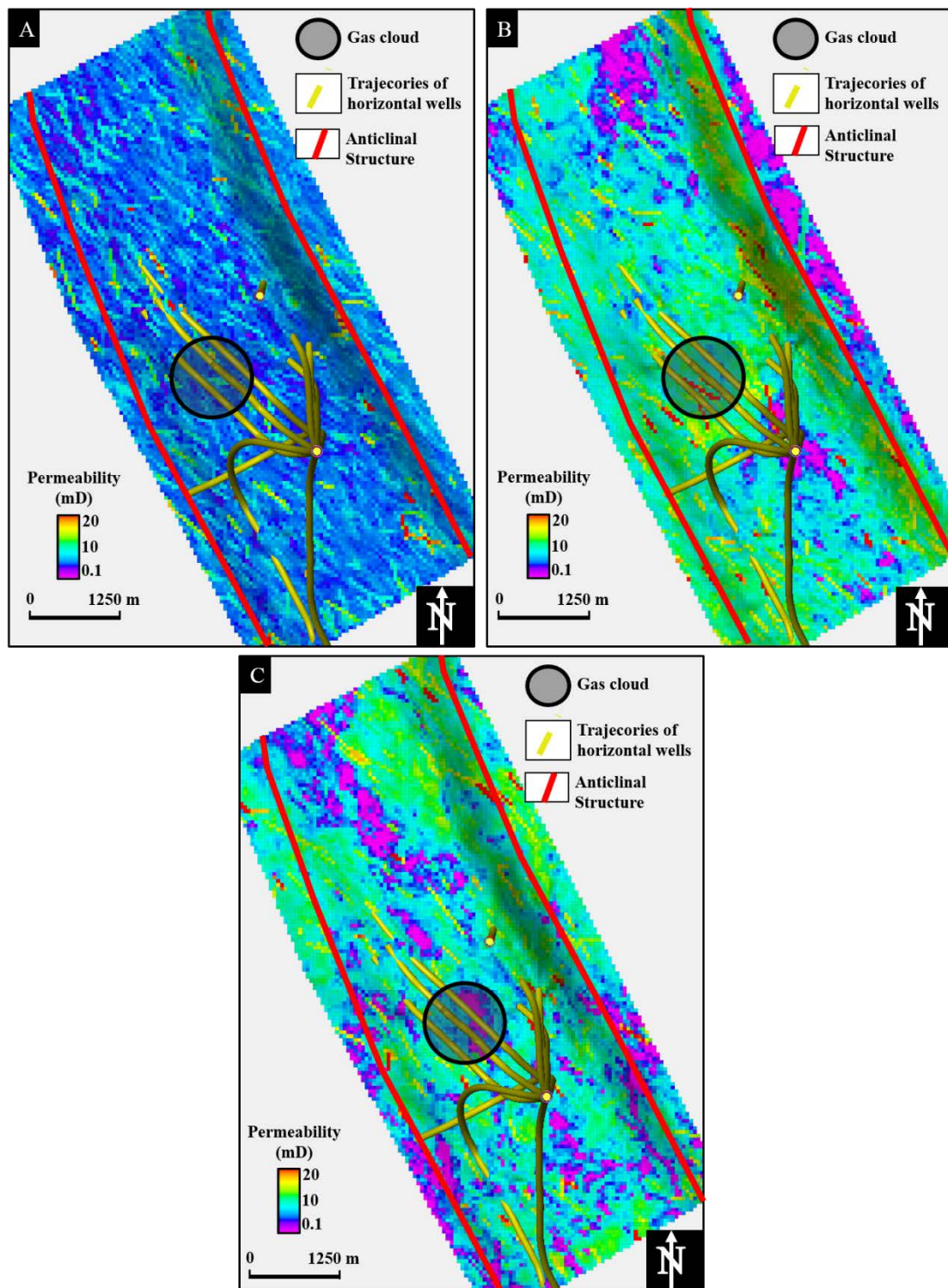


Figure 87 Permeability in k direction in the horizontal slice in Tor Formation obtained using the fracture intensity guided by (A) standard statistical procedure, (B) variance attribute, and (C) Young Modulus.